

2021

Study of mm-wave Fixed Beam and Frequency Beam-Scanning Antenna Arrays

Zeeshan Ahmed
Technological University Dublin

Follow this and additional works at: <https://arrow.tudublin.ie/engscheledis>

 Part of the [Electrical and Computer Engineering Commons](#)

Recommended Citation

Ahmed, Z. (2021). *Study of mm-wave Fixed Beam and Frequency Beam-Scanning Antenna Arrays*. Technological University Dublin. doi: 10.21427/JMSY-GE93

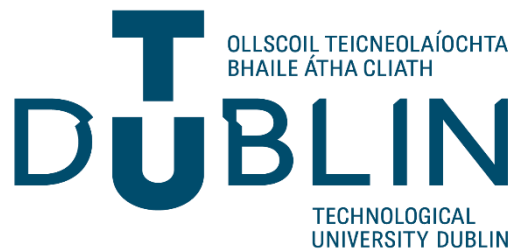
This Theses, Ph.D is brought to you for free and open access by the School of Electrical and Electronic Engineering at ARROW@TU Dublin. It has been accepted for inclusion in Dissertations by an authorized administrator of ARROW@TU Dublin. For more information, please contact arrow.admin@tudublin.ie, aisling.coyne@tudublin.ie, gerard.connolly@tudublin.ie.



This work is licensed under a [Creative Commons Attribution-Noncommercial-Share Alike 4.0 License](#)
Funder: Science Foundation Ireland

Study of mm-wave Fixed Beam and Frequency Beam-Scanning Antenna Arrays

Zeeshan Ahmed



A thesis submitted in fulfilment of the requirements for the degree of

Doctor of Philosophy

2021

Under the Supervision of

Prof. Max J. Ammann

Dr. Pádraig McEvoy

This thesis is dedicated to the memory of my grandfather.

MUHAMMAD ASLAM (1932 - 2020)

“It's the questions we can't answer that teach us the most. They teach us how to think. If you give a man an answer, all he gains is a little fact. But give him a question and he'll look for his own answers.”

— Patrick Rothfuss (The Wise Man's Fear)

Declaration

I certify that this thesis which I now submit for examination for the award of PhD, is entirely my own work and has not been taken from the work of others, save and to the extent that such work has been cited and acknowledged within the text of my work.

This thesis was prepared according to the regulations for graduate study by research of the Technological University Dublin and has not been submitted in whole or in part for another award in any other third level institution.

The work reported on in this thesis conforms to the principles and requirements of the TU Dublin's guidelines for ethics in research.

TU Dublin has permission to keep, lend or copy this thesis in whole or in part, on condition that any such use of the material of the thesis be duly acknowledged.

Zeeshan Ahmed

Date

Abstract

Millimeter-wave frequencies are anticipated to be widely adapted for future wireless communication systems to resolve the demand of high data-rate and capacity issues. The millimeter-wave frequency range offers wide spectrum and a shift for most newly developing technologies as the microwave and lower frequency bands are becoming overcrowded and congested. These high frequency bands offer short wavelengths which has enabled the researchers to design and implement compact and adaptable antenna solutions. This research focuses on the implementation, transformation and modification of antenna structures used in lower frequency bands to millimeter-wave applications with high gain and multi-band and wideband performances.

The first part of the thesis presents a microstrip patch array antenna with high gain in the upper 26 GHz range for 5G applications. The tolerance of the antenna, on widely used Rogers RT/duroid 5880 substrate, is observed with the edge-fed structure when curved in both concave and convex directions.

In the second part of the thesis, 20 rectangular loops are arranged in a quasi-rhombic shaped planar microstrip grid array antenna configuration with dual-band millimeter-wave performance. A comparison with equal sized microstrip patch array is also presented to analyse the performance. The antenna operates in the upper 26 GHz band and has two frequency bands in close proximity.

The third part of the thesis discusses the transition from wire Bruce array antenna to planar technology. Having been around for nearly a century and despite the simplicity of structure, the research community has not extended the concept of Bruce array antenna for further research. The proposed planar Bruce array antenna operates in three frequency

bands with optimization focus on 28.0 GHz band that has a directive fan-beam radiation pattern at broadside whereas the other two frequency ranges, above 30 GHz, have dual-beam radiation patterns which provide radiation diversity in narrow passages.

The final part of the thesis deals with the transformation and modification of wire Bruce array antenna geometry to edge-fed printed leaky-wave antennas for millimeter-wave frequency scanning applications. In the first approach, the lengths of the unit-cell are optimised, without any additional circuitry, to enable two scanning ranges and mitigate the *Open-Stopband*, at broadside, for seamless scanning in the first range. A Klopfenstein tapered divider is then deployed to make a linear array of the proposed antenna to achieve high gain. In the second approach, the horizontal and vertical lengths of the meandered unit-cell are replaced with semi-circular and novel bowtie elements, respectively, to obtain wide scanning range.

The numerical results and optimizations have been performed using CST Microwave Studio where the effects of metallization and dielectric losses are properly considered. The prototypes of the proposed antennas have been fabricated and experimentally validated.

Acknowledgments

I would like to express my sincere gratitude to my supervisor, Professor Max J. Ammann, for taking me under his wing, offering guidance, leadership, patience and continuous support throughout my PhD study. *Go raibh mile maith agat* and *Tausend Dank!*

I would also like to extend my sincere thanks to my co-supervisor, Dr. Pádraig McEvoy, for his valuable suggestions. I am really glad to have met and known my past and present colleagues in Antenna & High-frequency Research Centre. I am thankful to Dr. Kansheng Yang and Dr. Matthias John for the discussions and help towards fabrication of the antennas, Dr. Adam Narbudowicz, Dr. Xiulong Bao and Dr. Giuseppe Ruvio for their guidance, Manh Ha Hoang, Khatereh Nadali, Jakub Przepiorowski and Neeraj Kumar for the interesting discussions, cooperation, support and advice.

I would also like to acknowledge my confirmation examiner Professor William Scanlon's insight on antenna designs and millimeter-wave technology.

I am grateful to my parents, siblings and fiancé for their love, unequivocal support and inspiration throughout my education journey for which my mere expression of thanks does not suffice. A very special thanks to my friends Mehdi Ali, Arsalan Kazmi and Denis Manley for their camaraderie, discussions and encouragement.

Finally, I would like to acknowledge CONNECT - Science Foundation Ireland (SFI) research centre for future networks and communications for their financial support. This publication has emanated from research conducted with the financial support of Science Foundation Ireland (SFI) and is co-funded under the European Regional Development Fund under Grant Number 13/RC/2077.

Nomenclature

c_0	speed of light in vacuum, $299792458 \text{ ms}^{-1}$
C	capacity (F)
D	directivity (dBi)
ϵ_r	relative dielectric constant of a dielectric material
δ_{tan}	loss tangent of a dielectric material
η_{rad}	radiation efficiency
η_{total}	total efficiency
F	frequency (Hz)
G	gain (dBi)
G_r	realized gain (dBi)
H	substrate height (mm)
λ_0	wavelength (m)
P_{rad}	total power radiated (Wm^{-2})
ψ	phase of transfer function ($^\circ$)
R_{in}	input resistance of antenna (Ω)
S_{nn}	input reflection coefficient at port n
S_{mn}	transmission coefficient between ports n and m
σ	conductivity of a material (Sm^{-1})
θ, ϕ	angular coordinates in spherical coordinate system ($^\circ$)
U	radiation intensity (W/unit solid angle)
x, y, z	coordinates in a cartesian coordinate system (m)
Z_{in}	input impedance of antenna (Ω)

Abbreviations

<i>5G</i>	Fifth Generation
<i>BAA</i>	Bruce array antenna
<i>CPW</i>	Coplanar Waveguide
<i>CST</i>	Computer Simulation Technology GmbH ®
<i>D-BAA</i>	Dual Bruce array antenna
<i>DIT</i>	Dublin Institute of Technology
<i>FBW</i>	Fractional Bandwidth
<i>GAA</i>	Grid array antenna
<i>HPBW</i>	Half Power Beamwidth
<i>IEEE</i>	Institute of Electrical and Electronics Engineers
<i>ITT</i>	Institute of Technology Tallaght
<i>LCP</i>	Liquid Crystal Polymer
<i>LTCC</i>	Low Temperature Co-fired Ceramic
<i>LWA</i>	Leaky-Wave Antenna
<i>MIMO</i>	Multiple Input Multiple Output
<i>MPA</i>	Microstrip patch array
<i>mm-wave</i>	Millimeter Wave
<i>PIFA</i>	Printed Inverted F Antenna
<i>PCB</i>	Printed Circuit Board
<i>PEC</i>	Perfect Electric Conductor
<i>PET</i>	Polyethylene Terephthalate
<i>SIW</i>	Substrate Integrated Waveguide
<i>SLL</i>	Side Lobe Level
<i>SMA</i>	Sub-Miniature Type A Connector
<i>SMK</i>	K-Type connector
<i>TU Dublin</i>	Technological University Dublin
<i>UHF</i>	Ultra-High Frequency
<i>UWB</i>	Ultra Wide Band
<i>VHF</i>	Very High Frequency
<i>VNA</i>	Vector Network Analyzer

Table of Contents

Declaration	iii
Abstract	iv
Acknowledgments	vi
Nomenclature	vii
Abbreviations	viii
Table of Contents.....	ix
List of Figures	xii
List of Tables.....	xix
Chapter 1 Introduction	1
1.1 The Need for Speed in Wireless Communications	1
1.2 Objectives of Research.....	4
1.3 Key Contributions	6
1.4 Organisation of Thesis	7
Chapter 2 Background	9
2.1 Millimeter-Wave and <i>5G and Beyond</i> Spectrums	9
2.2 Millimeter-Wave Challenges	12
2.3 Millimeter-Wave Advantages and Applications	15
2.4 Microstrip Patch Antenna Array Configurations	19
2.5 Leaky-wave Antennas.....	23
2.6 Simulation and Modelling Tools.....	28
2.7 Measurement Setup.....	30

Chapter 3	Millimeter-Wave Patch Array Antenna on Curved Substrate.....	33
3.1	Introduction.....	33
3.2	Microstrip Patch Antenna	36
3.3	4×2 Center-Fed Microstrip Patch Antenna Array	39
3.4	Edge-Fed Microstrip Patch Antenna Array on Curved Substrate	46
3.5	Summary	54
Chapter 4	Dual-Band Millimeter-Wave Grid Array Antenna.....	56
4.1	Introduction.....	56
4.2	Quasi-Rhombic Grid Array Antenna Geometry	59
4.3	Parametric Analysis	61
4.4	Results and Discussion.....	65
4.5	Comparison with equidimensional Microstrip Patch Array Antenna	68
4.6	Summary	70
Chapter 5	Tri-Band Millimeter-Wave Bruce Array Antenna.....	72
5.1	Conventional Bruce Array Antenna.....	72
5.2	Planar Bruce Array Antenna Geometry	76
5.3	Parametric Analysis	77
5.4	Results and Discussion.....	82
5.5	Summary	86
Chapter 6	Millimeter-Wave Frequency Scanning Bruce Array Antennas	88
6.1	Introduction.....	88
6.2	Edge-Fed Planar Bruce Array Antenna.....	91
6.3	Dual Bruce Array Antenna	105
6.4	Modified Bruce Array Antenna with Semi-Circular and Bowtie Elements.....	112
6.5	Comparison with Existing Literature	123

6.6 Summary	126
Chapter 7 Conclusions and Future Work	127
7.1 Conclusions	127
7.2 Future Work	130
Bibliography	132
List of Publications	155
List of Modules Completed for Structure PhD	157

List of Figures

Figure 1.1. The evolution of mobile communication from 1G to 5G. (adapted from [2])	2
Figure 1.2. Cisco's projection of compound annual growth rate (CAGR) of data consumption per month from 2017 to 2022. [8]	3
Figure 2.1. Electromagnetic spectrum showing 5G sub-6 GHz range, mm-wave spectrum and 5G NR mm-wave spectrum.	10
Figure 2.2. Worldwide allocated and targeted 5G spectrum [10]	11
Figure 2.3. Attenuation of mm-waves by oxygen and water vapours. [32]	14
Figure 2.4. Attenuation due to rainfall in mm-wave region. [33]	14
Figure 2.5. Array configurations (a) Parallel feed (b) Series feed (c) Hybrid feed.	22
Figure 2.6. Representation of leaky-wave antenna and radiation principle.	23
Figure 2.7. An example of an infinitely long periodic LWA showing unit-cell's period, p , and scanning directions in backward and forward endfire regions.	25
Figure 2.8. Equivalent two-port representation of periodic LWA's unit-cell by ABCD matrix.	26
Figure 2.9. Flowchart of Research methodology.	29
Figure 2.10. Measurement setup at Antenna and High Frequency Research Centre (AHFR) (a) Block diagram (b) Anechoic chamber.	31
Figure 3.1. Geometry of rear-fed microstrip patch antenna.	36
Figure 3.2. $ S_{11} $ of patch antenna with inset varying (a) l_p (b) w_p (c) l_i (d) w_i .	37
Figure 3.3. 3D radiation pattern of microstrip patch antenna with inset at 27.40 GHz.	39
Figure 3.4. 4×2 element rear-fed array (a) Geometry (b) Prototype.	40
Figure 3.5. Parametric analysis with element spacing.	42

Figure 3.6. Simulated and measured $ S_{11} $ at 27.40 GHz.	42
Figure 3.7. Simulated total and radiation efficiency.	43
Figure 3.8. Simulated and measured gain for the 4×2 array.	44
Figure 3.9. Simulated and Measured polar plots at 27.40 GHz (a) xz-plane (b) yz-plane.	45
Figure 3.10. 3D Radiation pattern of rear-fed microstrip patch antenna array at 27.40 GHz.	45
Figure 3.11. Surface current distribution at 27.40 GHz at phase = 0°	46
Figure 3.12. Edge-fed microstrip patch array antenna with curved substrate (a) Geometry (b) Prototype.	47
Figure 3.13. Simulated $ S_{11} $ with concave bending.....	49
Figure 3.14. Simulated realized gain with concave bending.....	49
Figure 3.15. Simulated polar plots with concave bending (a) xz-plane (b) yz-plane. ...	50
Figure 3.16. Simulated $ S_{11} $ variation with different degrees of convexity.	51
Figure 3.17. Simulated realized gain variation with different degrees of convexity.	52
Figure 3.18. Simulated polar plots with convex bending (a) xz-plane (b) yz-plane.	53
Figure 4.1. A 5-loop grid array antenna arrangement showing current distribution in long sides and short sides.	57
Figure 4.2. Rear-fed grid array antenna (a) Geometry (b) Prototype.....	60
Figure 4.3. Feed position locations along the upper symmetric half of the yz-axis.....	61
Figure 4.4. Feed positions analysis (a) $ S_{11} $ (b) Realized gain.....	62
Figure 4.5. Parametric analysis varying (a) L_b (b) W_b (c) W_t (d) L_t	63
Figure 4.6. Simulated and measured $ S_{11} $ of the quasi-rhombic grid array antenna.	65
Figure 4.7. Simulated radiation efficiency of the grid array antenna.....	66
Figure 4.8. Surface current distribution at phase = 0° (a) 27.0 GHz (b) 29.10 GHz.....	66

Figure 4.9. Simulated and measured polar plots of grid array antenna (a) xz-plane (b) yz-plane.	67
Figure 4.10. Geometry of 4×4 rear-fed microstrip patch array antenna.	68
Figure 4.11. 4×4 element microstrip patch array antenna showing simulated (a) $ S_{11} $ (b) Radiation Efficiency (c) polar plot in xz-plane (d) polar plot in yz-plane.	70
Figure 5.1. Variations of Twin-Line fed wire Bruce array antenna with number of vertical radiating elements (a) 2 (b) 3 (c) 4 (d) 5. (adapted from [139]).....	73
Figure 5.2. 80-meter wire Bruce array antenna (a) free-space E-plane patterns for 2, 3, 4 and 5 vertical elements (b) SWR of a 4 vertical element structure [139].	74
Figure 5.3. (a) Geometry and (b) Prototype of rear-fed planar Bruce array antenna with 16 vertical elements.....	76
Figure 5.4. Effect of parametric variation on $ S_{11} $ (a) varying v and keeping h fixed at $1.46 \times \lambda/4$ (b) varying h and keeping v fixed at $1.46 \times \lambda/4$ (c) varying h and v simultaneously.	78
Figure 5.5. $ S_{11} $ with and without $1.46 \times \lambda/8$ inward bent element with 16-element structure.....	79
Figure 5.6. Geometry of Planar Bruce Array antenna with 15 vertical elements.	80
Figure 5.7. Simulated $ S_{11} $ of Planar Bruce Array antenna with odd 15-elements.	80
Figure 5.8. Current distribution of 15-element BAA at phase = 0 (a) 26.60 GHz (b) 29.90 GHz (c) 33.10 GHz.....	81
Figure 5.9. 3D radiation pattern of odd 15-element Bruce Array antenna structure (a) 26.60 GHz (b) 29.90 GHz (c) 33.10 GHz.....	81
Figure 5.10. Simulated and measured $ S_{11} $ of planar Bruce array antenna.	82
Figure 5.11. Simulated total and radiation efficiency of planar Bruce array antenna....	83
Figure 5.12. Current distribution of 16-element BAA at phase = 0° (a) 28.0 GHz	

(b) 31.54 GHz (c) 34.34 GHz.....	84
Figure 5.13. 3D radiation pattern plots at (a) 28.0 GHz (b) 31.54 GHz (c) 34.34 GHz.	84
Figure 5.14. Simulated and measured xz-plane and yz-plane radiation pattern plots at (a) 28.0 GHz (b) 31.54 GHz (c) 34.34 GHz.....	85
Figure 6.1. A twin-line fed geometry of conventional meandered 11 vertical element wire BAA showing magnitudes and direction of current distribution with in-phase vertical elements.....	90
Figure 6.2. Geometry of meandered unit-cell printed on a 0.254 mm thick grounded Arlon DiClad 880.....	92
Figure 6.3. (a) Attenuation constant and (b) phase constants normalized to the free-space wavenumber (k_0) for the unit-cell consistent with conventional wire BAA theory varying lengths v and h simultaneously.	92
Figure 6.4. Geometry of a 1-D periodic edge-fed BAA-LWA based on conventional equi-dimensional unit-cell printed on a 0.254 mm thick grounded Arlon DiClad 880. .	93
Figure 6.5. Simulated Effect of adding number of vertical elements in BAA (a) $ S_{11} $ (b) HPBW.	94
Figure 6.6. Simulated and measured $ S_{11} $ plot of 11 unit-cell elements with conventional equi-dimensional v and h	95
Figure 6.7. Simulated and measured realized gain plot of 11 unit-cell elements with conventional equi-dimensional v and h	95
Figure 6.8. Scanning in forward quadrant of planar 11 element BAA with equal 3.40 mm conventional dimensions with broadside gain degradation.	96
Figure 6.9. (a) Attenuation constant and (b) phase constants normalized to the free-space wavenumber (k_0) with conventional and proposed modified dimensions of h and v showing mitigation of open-stopband effect.....	97

Figure 6.10. Dispersion diagram of modified BAA unit cell.....	98
Figure 6.11. (a) Geometry with detail of the h_s element and (b) prototype of a 1-D quasi-periodic BAA-LWA printed on a 0.254 mm thick grounded Arlon DiClad 880.	99
Figure 6.12. Simulated and measured $ S_{11} $ plot of 11 unit-cell elements with improved unit-cell and the addition of h_s element to the periodic structure.	100
Figure 6.13. Simulated and measured realized gain plot of 11 unit-cell elements with improved unit-cell and the addition of h_s element to the periodic structure.	101
Figure 6.14. (a) Main beam direction and (b) Sidelobe Level plots of BAA with modified dimensions of h and v	102
Figure 6.15. Proposed 1-D quasi-periodic BAA-LWA with improved unit-cell dimensions (a) 1 st scanning range in backward quadrant (b) 1 st scanning range in forward quadrant and (c) 2 nd scanning range after role reversal of main and back lobe.....	103
Figure 6.16. Simulated HPBW and Radiation Efficiency of the proposed BAA.	104
Figure 6.17. Geometry of Klopfenstein taper showing stepped discrete blocks from 25 Ω to 50 Ω , outlined smooth taper and two-way divider.....	106
Figure 6.18. $ S_{11} $ performance of 13-section discrete and smooth wideband Klopfenstein tapered feedline.	107
Figure 6.19. D-BAA-LWA with tapered Klopfenstein feed two-way divider based on improved unit-cell (a) Geometry (b) Prototype.	108
Figure 6.20. Simulated and measured $ S_{11} $ plot of D-BAA with improved unit-cell...	109
Figure 6.21. Simulated HPBW and Radiation Efficiency of BAA and D-BAA.	109
Figure 6.22. Proposed quasi-periodic D-BAA with improved unit-cell dimensions showing simulated and measured (a) 1 st scanning range in backward quadrant (b) 1 st scanning range in forward quadrant and (c) 2 nd scanning range after role reversal of main and back lobe.....	111

Figure 6.23. Geometry of the modified BAA unit-cell with vertical bowtie and horizontal semi-circular segments printed on a 0.254 mm thick grounded Arlon DiClad 880.	112
Figure 6.24. Top view of the proposed periodic 13 unit-cell antenna fabricated on 0.254 mm thick grounded Arlon DiClad 880 substrate (a) Geometry (b) Prototype....	113
Figure 6.25. Effect of varying length, l_v , and diameter, l_c , simultaneously of 13 unit-cell element periodic structure with $w_v = 0.76$ mm unit-cell segments on $ S_{11} $	115
Figure 6.26. Effect of varying vertical bowtie segment parameters, w_v and l_t , of 13 unit-cell element periodic structure independently on $ S_{11} $ while the other parameters remain constant.	115
Figure 6.27. Effect of independently varying lengths of 13 unit-cell element periodic structure with fixed $w_v = 0.65$ mm bowtie segments on $ S_{11} $ (a) Varying l_v with fixed $l_c = 3.50$ mm (b) Varying l_c with fixed $l_v = 3.50$ mm.....	116
Figure 6.28. Simulated realized gain of 1-D periodic BAA-LWA with $l_v = l_c = 3.50$ mm and $w_v = 0.76$ mm unit-cell showing gain degradation around 28.0 GHz.	117
Figure 6.29. Simulated and measured $ S_{11} $ of 13 unit-cell element periodic structure with bowtie vertical unit-cell segments.....	118
Figure 6.30. Simulated and measured realized gain comparison of 13 unit-cell element periodic structure with $w_v = 0.76$ mm and modified bowtie vertical unit-cell segments.	119
Figure 6.31. 3D radiation pattern visualising scanning in top and side view at (a) 24.0 GHz (b) 28.0 GHz (c) 35.0 GHz.....	120
Figure 6.32. Scanning range of the proposed 1-D periodic modified BAA-LWA with bowtie and semi-circular unit-cell (a) backward quadrant and (b) forward quadrant...	121
Figure 6.33. (a) Sidelobe Level and (b) Main beam direction in the yz-plane of the proposed LWA.	122

Figure 6.34. Simulated plots of LWA (a) Radiation Efficiency and (b) HPBW in y-z plane.	123
---	-----

List of Tables

Table 3.1. Optimised design parameters of the proposed antenna array.....	41
Table 3.2. Frequency reconfiguration, realized gain, HPBW and sidelobe level with mechanical bending of Rogers RT/duroid 5880 substrate.	55
Table 4.1. Design parameters of Grid array antenna.....	60
Table 4.2. Design parameters of 4×4 microstrip patch array antenna.....	69
Table 4.3. Performance comparison between proposed GAA and MPA.....	71
Table 5.1. Optimised parameters of planar BAA.	77
Table 5.2. Radiation characteristics of the proposed 16-element BAA.	86
Table 6.1. Design parameters of Bruce array antenna with modified unit-cell.....	99
Table 6.2. Geometric details of two-way Klopfenstein taper feed divider.	106
Table 6.3. Parametric details of antenna with semi-circular and bowtie elements unit-cell.	114
Table 6.4. Performance comparison between proposed LWAs and LWAs in literature.	125

Intentionally Left Blank

Chapter 1

Introduction

1.1 The Need for Speed in Wireless Communications

Over the past decade, there has been a multiple fold increase in the demand of wireless communications. The rise in internet data traffic and dependability of consumers on high-speed communications has led to increased capacity demands. The First Generation (1G) commercial network was first deployed by Nippon Technologies in Japan in 1979 which mainly featured voice services with data rate of 2 Kbps. 1G technology used analog signals for data transfer, had very small system capacity to accommodate large number of users, had low quality voice links, poor handoff and no security for eavesdropping [1], [2]. From the infant 1st generation, the wireless communications systems transitioned to the Second Generation (2G) which was based on Global System for Mobile communications (GSM). Deployed commercially in 1990s as Time Division Multiple Access (TDMA) technology, it addressed the poor voice quality issues by replacing the analog technology with digital communication. It offered digitally encrypted Short Messaging Service (SMS), Multimedia Messaging Service (MMS) and voice services. The introduction of commercial digital services such as email influenced the expansion of 2G. The adaptation of Code Division Multiple Access (CDMA) enhanced GSM's abilities with General Packet Radio Services (GPRS) technology and had data rate of 14.40 Kbps to

64.0 Kbps towards the end of the Second Generation (2.5G and 2.75G also known as Enhanced Data Rates for GSM Evolution (EDGE)). By the end of the year 2002, the number of cellphone and internet subscribers had reached to 1.5 billion and 631 million, respectively [3]. The demand of wireless capacity became explosive with the introduction of smartphones and internet accessible application development. The data speed of 2G and its enhanced systems was snail-slow and not enough to cater the needs of the third industrial revolution also known as the age of digital transformation. The early Third Generation (3G) systems were based on Universal Mobile Telecommunications Service (UMTS) technology and were able to achieve transfer speed of up to 2 Mbps. The 3G network later evolved to High-Speed Package Access (HSPA) and featured peak download and upload speeds of 14.70 Mbps and 5.40 Mbps, respectively. According to the International Telecommunication Union (ITU), the global population covered by at least a 3G network, in 2019, has surpassed 7 billion mark [4]. 4G and its subsequent iterations, Long Term Evolution (LTE) were the successors of 3G. The systems designed until 3G

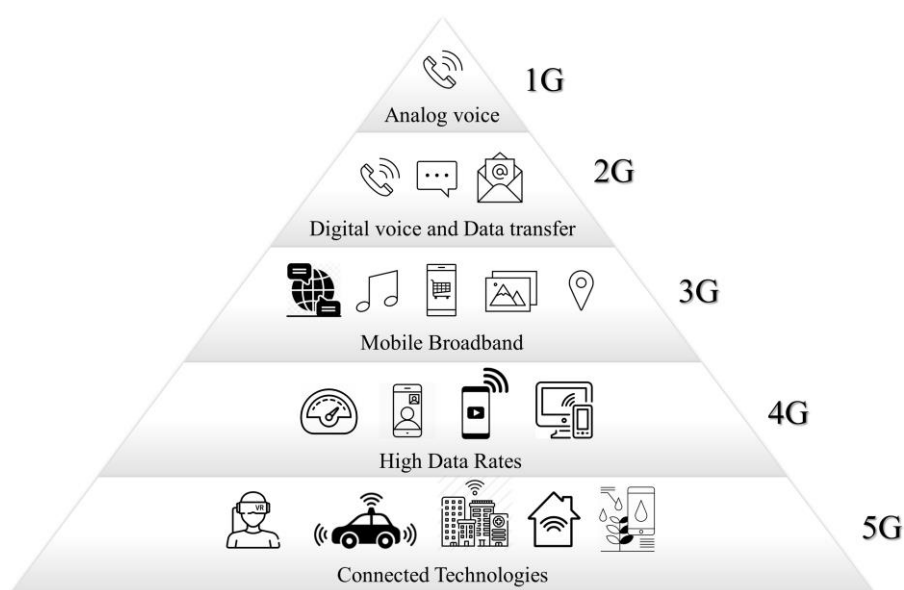


Figure 1.1. The evolution of mobile communication from 1G to 5G. (adapted from [2])

were primarily based on voice services whereas 4G was designed for better data transmission thereby encouraging more internet users for applications such as video streaming, mobile TV and video calling etc, globally. Several service providers around the globe offered standalone 4G internet devices to replace broadband devices. The global 4G population coverage was over 80 percent by June 2020 and has been forecasted to reach around 95 percent in 2026 [4]. While 4G was a great step towards evolution of wireless communications, the next generation 5G is designed for much more than just smartphone connectivity. The vast expansion of smartphones industry and other band applications has led to saturation in the sub-6 GHz bands which is why the cellphone providers are expanding 5G to mm-wave bands. 5G provides extremely low latency, the communication is a lot smoother and allows many devices to connect to the network with low power consumption having theoretical speed up to 300 Gbps which is why it is drawing interest from researchers and industries around the globe to expand 5G's capabilities to applications beyond the smartphones industry [5], [6]. Ericsson's mobility report in 2019 predicted that in 2020, the 5G device volume will reach 160 million units [7] but because of the uncertainty due to Coronavirus disease 2019 (Covid-19) pandemic, with lockdowns

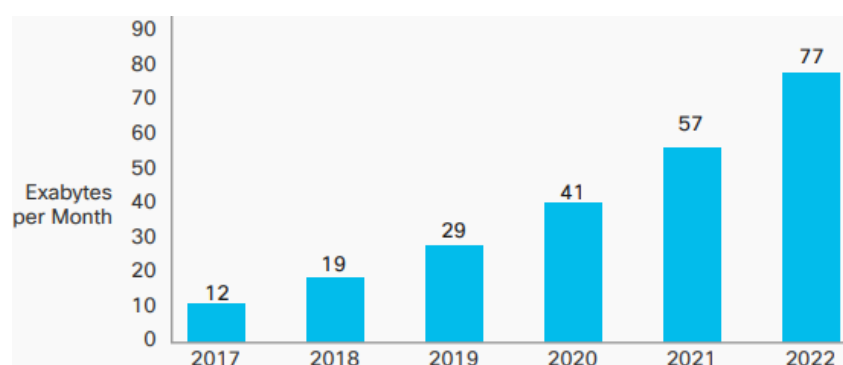


Figure 1.2. Cisco's projection of compound annual growth rate (CAGR) of data consumption per month from 2017 to 2022. [8]

and restrictions around the globe, the net 5G subscriptions in the third quartile of 2020 were as low as 11 million. Nevertheless, many service providers have commercially launched their 5G services and these projections have been adjusted by Ericsson who now forecast that there will be 8.8 billion mobile subscriptions, in 2026, including 3.5 billion 5G subscribers [9]. Cisco's projections show that the global monthly mobile data consumption will reach 77 exabytes/month and 5G will be 11.8% of the traffic by 2022 [8].

1.2 Objectives of Research

With the introduction of *5G and Beyond* and expanding technological possibilities in the mm-wave region, the future wireless applications are expected to be guided in this less crowded frequency region to meet high speed connectivity and data-rate demands. Several antenna design techniques have been explored in the literature to meet these new demands. The objectives of this research are driven by the challenges faced for mm-wave antenna designs and are summarized below:

- Most system deployments, in the literature and the industry, are exhibited for sub-6 GHz communications. The extensive list of applications and the frequency bands for mm-wave are not yet defined with the researchers continuously exploring the technological opportunities and several countries still considering the possibility of allocating more bandwidth for mm-wave communications [10]. Conventionally, the resonant antenna array technologies, in the microwave and low frequency region, are designed around a single frequency but with wide bandwidth being opened up for 5G connectivity in the mm-wave region and for applications beyond mm-wave cellular communication, the development of

multi-resonant and wide bandwidth antenna arrays will provide high gain to overcome the atmospheric attenuations and path loss in the mm-wave region.

- The complex nature of antenna designs for mm-wave applications in the literature, such as multilayer structures, custom-made material antennas, parasitic structures and Sub-Integrated Waveguide (SIW) structures, have good performance but are massive and consequently add up to the cost of manufacturing. Performance oriented planar, single-layered, compact and efficient antennas with minimalistic passive circuitry are one the focus areas in this research.
- The choice of substrate is one of the rudimental steps in the design hierarchy of an antenna design. A low-profile substrate with features such as low electrical losses and suitability for atmospheric conditions with high moisture is sought for antenna applications in high frequency regions. The off-the-shelf commercially used substrate, Rogers RT/ Duroid 5880, is a popular choice substrate for mm-wave applications which fits the above-described criterion however, exploration and knowledge about the fabrication tolerances that may affect the performance of an antenna, in the mm-wave region, gives a better perspective on how to avoid or, in certain cases, exploit the characteristics of material properties for a pertinent application.
- A large number of mm-wave antennas can be obtained by scaling and configuring the wavelengths of the existing antenna technologies researched in the lower frequency bands such as wire antennas. Among those antennas, the ones with potential of having high efficiency, gain and directivity should be considered for transformation to mm-wave applications. In theory, scaling the wavelength to mm-wave is an uncomplicated procedure. However, in practice, as the frequency

increases, the footprint of the antenna reduces in which coupling effects, fabrication tolerances and imperfections, as well as expensive design materials, have to be taken into account. Therefore, these antenna designs require modification for transformation to planar geometries to be suitable to operate in the mm-wave region. Unlike the lower frequency bands, where complex antenna structures can be relatively easily designed and fabricated for a particular application, the most important task is to design simplistic planar structures that are fabrication-friendly and cost-effective.

1.3 Key Contributions

The major contributions in this research are listed below:

- Often considered as a rigid substrate, Rogers RT/Duroid 5880 is prone to deformations during fabrication and testing. The research presented in this thesis has shown the effects of bending a microstrip antenna array in both convex and concave directions at 28 GHz. While majority of the antennas in this thesis are planar structures however, for conformal 5G and mm-wave applications, the proposed antenna array offers a simplistic solution for high gain mechanically tuneable frequency performance.
- A novel simplistic shape of printed wire loop-based grid array antenna for 28 GHz 5G applications, with wide beamwidth, wideband and dual band performance, is proposed. A performance comparison with microstrip patch array antenna, having similar footprint, is presented.
- For the first time, a meandered Bruce array antenna is transformed to a planar

microstrip based geometry for mm-wave applications. The proposed antenna is compact and modified to operate for 28 GHz 5G applications, having high bandwidth with its multiband resonances, and has high gain fan-beam radiation pattern.

- Two novel modifications of the planar Bruce array antenna are further studied in this thesis for mm-wave frequency beam-scanning applications with the ability to suppress the open-stopband (OSB) problem, common in leaky-wave periodic structures, without using any additional circuitry. The first edge-fed structure provides wide enough bandwidth to accommodate two frequency scanning regions in K-Band and Ka-band. The gain is improved considerably, without any substantial increase in the antenna size, by forming a linear array deployed using a two-way Klopfenstein tapered feed divider for wide bandwidth. In the second modification of planar Bruce array antenna, the elements of meandered unit-cell are replaced with semi-circular and bowtie elements to suppress the open stopband, at 28 GHz broadside, for wide beam-scanning mm-wave applications.

1.4 Organisation of Thesis

An overview of breakdown of contents of the thesis is presented in this section.

Chapter 1 presents an overview of the evolution, and the need for data transfer speed, of wireless technologies from 1G to 5G. It further highlights the objectives of the research presented in this thesis.

Chapter 2 discusses the mm-wave frequency band, with focus on 5G spectrum, its applications, advantages and challenges along with fundamentals of the relevant antenna

technologies utilized in this thesis.

Chapter 3 provides discussion of microstrip patch antenna array with rear-fed and edge-fed mechanisms. A detailed discussion regarding tolerance of commonly used flexible Rogers RT/duroid 5880 substrate on edge-fed 4×2 patch array is presented in this chapter.

Chapter 4 focuses on a planar grid array antenna for upper 26 GHz applications. The feed position on the array is optimized to obtain dual band with both single and dual beam behaviours. Additionally, the antenna's performance is compared with a 4×4 patch array antenna.

Chapter 5 demonstrates the transformation of wire Bruce array antenna to its printed counterpart for mm-wave applications. The lengths of the elements are modified and results, with both even and odd number of radiating elements, are discussed to obtain three frequency bands with single and dual fan-beam radiation characteristics.

Chapter 6 proposes further modifications in printed Bruce array antenna structure to obtain frequency scanning behaviour in K-Band and Ka-Band. Optimization of horizontal and vertical lengths are discussed to mitigate open-stopband problem for seamless scanning through broadside and dual Bruce array antenna is proposed using Klopfenstein tapered divider. Another modification is proposed in which the vertical and horizontal elements are replaced with bowtie and semi-circular elements which enable wide continuous scanning range.

Chapter 7 concludes the thesis with summary of key results and discusses potential future advancements pertinent to the presented research.

Chapter 2

Background

2.1 Millimeter-Wave and *5G and Beyond* Spectrums

In the electromagnetic spectrum, the mm-wave band ranges from 30 GHz to 300 GHz with wavelengths from 10 mm to 1 mm, respectively. Compared to the sub-6 GHz frequency range, which is very saturated, the relatively unused mm-wave band is less crowded and provides wide bandwidth opportunity for development of applications to cater future demands of capacity and data rate. The primary reason why this band has largely remained untapped in the previous years is because of the unsuitable propagation conditions for wireless communications, that is discussed at length in section 2.2. However, with the technological advancements over time, these limitations are now deemed conquerable [11], [12].

The unlicensed 60 GHz mm-wave band has attracted the research community to explore applications for Wireless Local Area Network (WLAN), cellular systems and Wireless Personal Area Network (WPAN). The first major regulation of 60 GHz band, for unlicensed commercial consumers, was initiated in the US by Federal Communications Commission (FCC) in 1995 where the suitability of this band was suggested for short range and high data rate wireless broadband applications between 57 GHz and 59 GHz. In 2002, the FCC allocated additional 5 GHz to this range increasing the 60 GHz

mm-wave unlicensed bandwidth between 57 GHz to 64 GHz [13]. Due to the limited interference observed for short range, narrow beamwidth and point-to-point applications, the licensing of this band was not deemed necessary therefore it enabled 7 GHz of license-free spectrum for high data rate 60 GHz Wi-Fi, alternatively known as Wireless Gigabit (WiGig), compared to less than 3.5 GHz (2.4 GHz – 5.9 GHz) in the sub-6 GHz band for Wi-Fi, covering IEEE 802.11ad and the upcoming IEEE 802.11ay standards [14]–[17].

The recent introduction of the 5G New Radio (NR) in the mm-wave spectrum has attracted both commercial and research communities to explore the potential of new applications as well as transforming the existing applications to these bands. As stated earlier, the mm-wave band in the electromagnetic spectrum starts from 30 GHz but in 5G NR, shown in **Figure 2.1**, the mm-wave spectrum is considered from 24 GHz due to its low latency and high capacity features [18]. The availability of large bandwidth in mm-wave region enables more than 1 GHz channel bandwidth for cellular communication, especially, at 28 GHz, 38 GHz and between 70 GHz and 80 GHz [19]. In 2016, FCC announced the regulations and measures to be taken to minimize the delays in 5G development in the US. While additional bands of mm-wave are currently being reviewed, such as 70 GHz, 80 GHz and 90 GHz, the FCC has released almost 5 GHz bandwidth

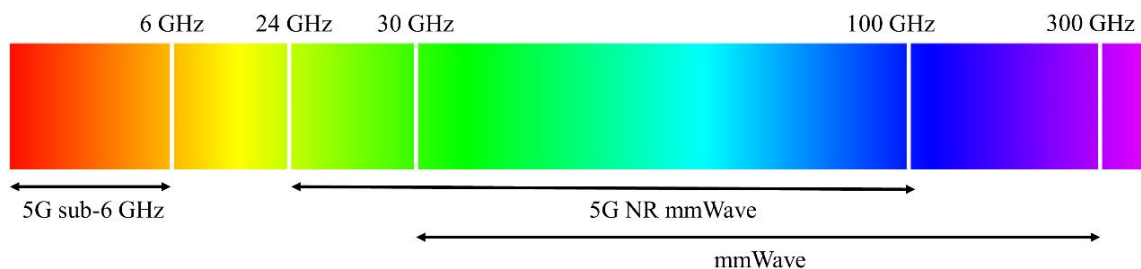


Figure 2.1. Electromagnetic spectrum showing 5G sub-6 GHz range, mm-wave spectrum and 5G NR mm-wave spectrum.

between 24 GHz and 39 GHz, around 600 MHz in the sub-6 GHz spectrum and 2 x 35 MHz channels at 600 MHz with an additional release of 64 GHz – 71 GHz unlicensed spectrum [20], [21]. The European Commission followed suit and, in September 2016, issued *5G Action Plan* to streamline the development and deployment of 5G infrastructure across European Union (EU) by 2020. The plan called on the Member States to have a coordinated approach and have a consensus on the cross-border 5G spectrum in the Digital Single Market [22]. In line with this plan, in June 2017, the Commission for Communications Regulation of Ireland (Comreg) auctioned 3.6 GHz spectrum in the range of 3400 MHz – 3800 MHz [23] and, in June 2018, 26 GHz spectrum in the range of 24.745 GHz – 25.277 GHz and 25.753 GHz – 26.285 GHz [24]. Ofcom, in the UK, harmonised in this coordinated approach for spectrum allocation to support EU's 5G architecture and finalized auction of 700 MHz and 3.6 GHz bands in April 2021 [25]. It also targets to award 26 GHz band in the future for mid-band mm-wave 5G communications and has shown an intention to plan regularization of 66 GHz – 71 GHz spectrum.

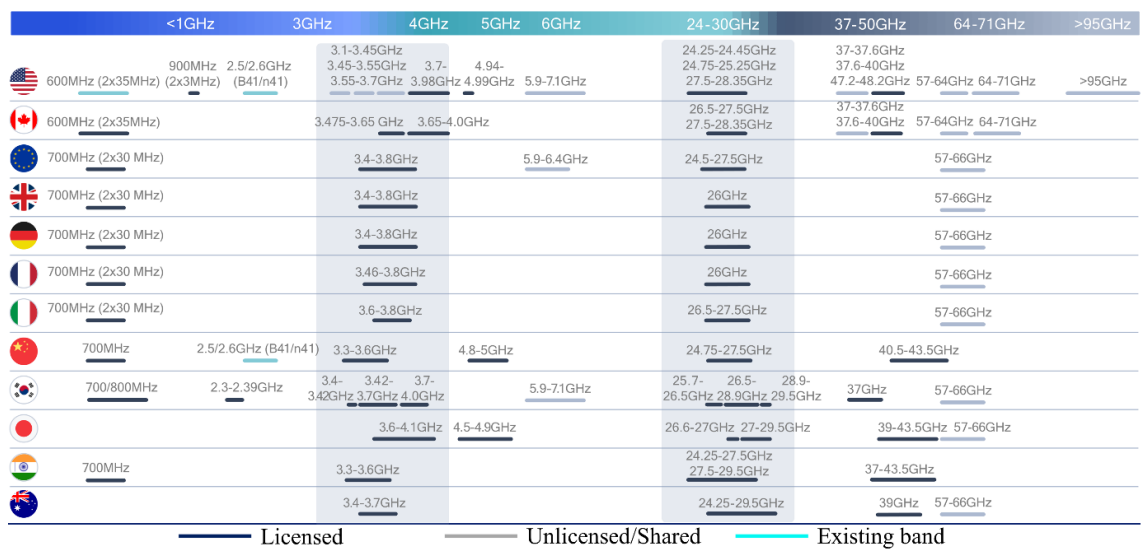


Figure 2.2. Worldwide allocated and targeted 5G spectrum [10]

Other mm-wave communications bands, such as 32 GHz band (31.80 - 33.40 GHz), have been proposed by ITU which are being considered by the FCC for the expansion of 5G network [26]. In this thesis, the antennas related to 5G are primarily designed for frequency bands in 24 GHz – 30 GHz range.

2.2 Millimeter-Wave Challenges

As opposed to the wireless and cellular systems in the 300 MHz – 3 GHz region, the mm-wave communication systems require unhindered line-of-sight path to perform to their expected potential, but the hostile propagation conditions effect this performance requirement adversely. The high diffraction and penetration losses in the mm-wave region cannot be discounted while studying scattered and reflected signals. Typically, the building and human body penetration losses vary to more than 40 dBs [27]. Friis free space path loss equation describes the fundamental relationship for transmitted and received powers, P_t and P_r , respectively, which presents a vital scenario for Line of Sight (LOS) communication in small cells radius.

$$\frac{P_r}{P_t} = G_t G_r \left(\frac{\lambda}{4\pi d} \right)^2 \quad (2.1)$$

where λ is the wavelength, d is the transmitter and receiver distance and G_t and G_r are the transmit and received antenna gains, respectively.

Substituting $\lambda = c/f$, where c is the speed of light and f is the frequency, in equation (2.1) gives us the resultant received power,

$$P_r = P_t G_t G_r \left(\frac{c}{4\pi d f} \right)^2 \quad (2.2)$$

It can be seen from equation (2.2) that as the frequency increases, the energy transfer decreases for antennas with specified gain. Therefore, the path loss, which is the difference between transmitted and received power, increases for higher frequency regions such as mm-waves, compared to sub-6 GHz or lower frequency bands. Another factor is the distance between transmitter and receivers. The reduction in separation in Urban Macrocells (UMa), between the transmitter and receiver, from 100 m to 25 m increases the probability of LOS channel availability from 0.35 to 0.90, respectively [27], [28]. Several propagation models have been proposed over the past years for mm-wave communications. Penetration losses of 25 dB and 37 dB at 38 GHz was found for tinted glass window and glass door, respectively. At 28 GHz, 40.1 dB loss for tinted glass installed outdoors and 28.3 dB for brick pillars was measured. On the other hand, clear glass installed indoors had 3.6 dB and dry wall had 6.8 dB of penetration losses [27], [28].

For the presently considered 26 GHz, 28 GHz and 38 GHz mm-wave bands of 5G, the atmospheric conditions do not affect the performance significantly but for the high frequency mm-wave bands considered for future inclusion in the 5G and beyond networks, such as 60 GHz, shown in **Figure 2.3**, the wavelengths are so small that, besides the high Friis free-space loss and difficulty in penetration through objects, even minute levels of air, water, temperature and humidity variations in the atmosphere, from temperate to tropical regions, will be evident in signal attenuation [19], [29]–[31]. For mm-waves, propagation into shadowed vegetated regions is achievable through scattering and diffraction but the intensity of the signal is expected to drop. From **Figure 2.3**, in order to operate near 60 GHz, frequency adjustment can assist in controlling the transmission distance thereby minimizing the signal attenuation leading to less vulnerability to interference and eavesdropping [30]. Studies have shown that at 28 GHz and 38 GHz, the rain

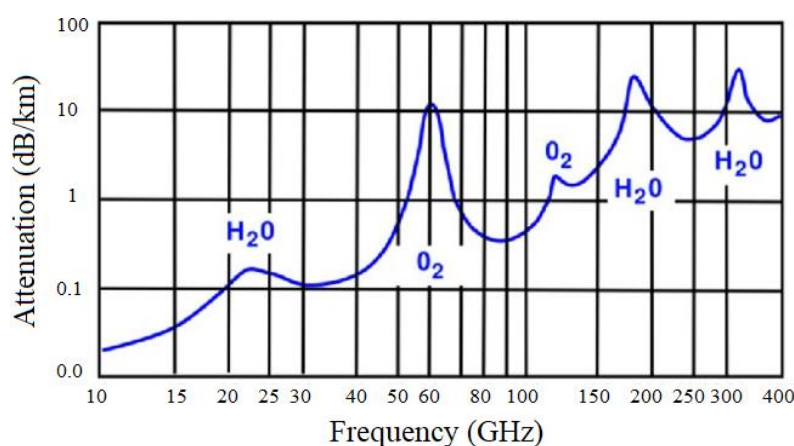


Figure 2.3. Attenuation of mm-waves by oxygen and water vapours. [32]

droplets do not contribute significantly towards signal attenuation in path loss [29], [33].

Figure 2.4 shows that at 28 GHz and 38 GHz, the signal attenuated by 25 mm/h rain rate is about 7 dB/km (1.4 dB/200 m cell radius) and 8 dB/km (1.6 dB/200 m), respectively.

droplets do not contribute significantly towards signal attenuation in path loss [29], [33].

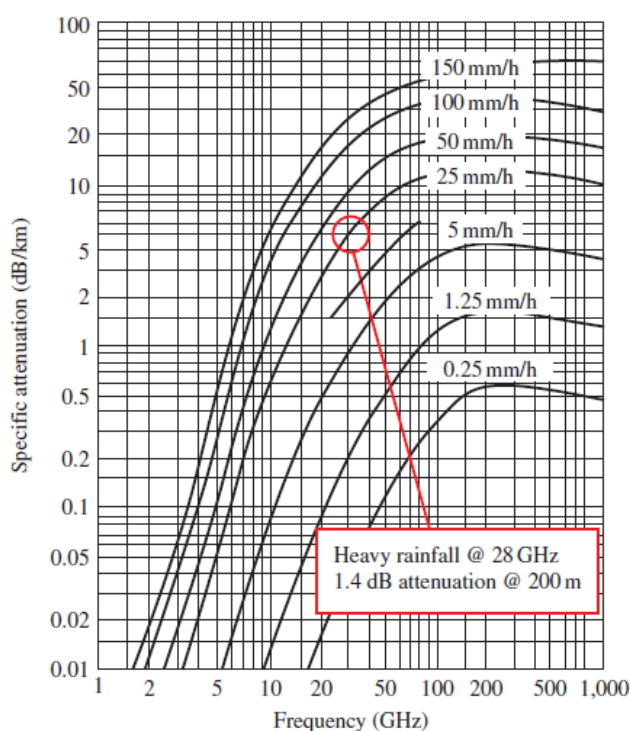


Figure 2.4. Attenuation due to rainfall in mm-wave region. [33]

Figure 2.4 shows that at 28 GHz and 38 GHz, the signal attenuated by 25 mm/h rain rate is about 7 dB/km (1.4 dB/200 m cell radius) and 8 dB/km (1.6 dB/200 m), respectively. On the other hand, between 50 GHz and 200 GHz, the atmospheric attenuation is much larger. This aspect of comparatively little atmospheric attenuation in 28 GHz and 38 GHz bands make them a strong potential contender for long distance, indoor and outdoor wireless communication systems. The low propagation distance problem in the mm-wave region can be resolved by reduction of the cell size of covered area up to a defined threshold of acceptable signal attenuation prioritizing line-of-sight paths in order to mitigate path loss. This cell size reduction technique is also known to minimize atmospheric effects for the frequencies affected by signal attenuation [29].

2.3 Millimeter-Wave Advantages and Applications

As discussed in Chapter 1, the wireless mobile data traffic has grown exponentially in the past two decades and, with it, the demand for higher data rates and more capacity has risen which cannot be catered by the existing low frequency spectrums and wireless systems. The research and commercial sectors have found mm-wave spectrum to the rescue with its much wider bandwidth than any other spectrum to accommodate existing and new applications. The abundance of the spectrum in the mm-wave band not only resolves the spectrum saturation problem but it also ensures the delivery of ultra-low latency transmission with its high capacity, better propagation through dry snow, dust and fog, than optical waves and data rate comparable to fiber optic speeds, thereby enhancing network responsiveness [34]. The mm-wave region has a relatively shorter wavelength which was once considered a drawback for the applications because of expensive fabrication and

propagation distance challenges but now that the technology has evolved, and several new antenna design practices have been researched on that these limitations can be overcome which enables small, compact, high gain and integratable antenna designs using beamforming techniques to augment coverage with efficient utilization of the spectrum. In the scenarios where mm-wave based device is deployed indoors, there is a potential of reusing spectrum in a larger physical area due to its short radio signals [35]. The short propagation distance also provides reliable and secure communication with low probability of eavesdropping because of the narrow beamwidth, no wall penetration characteristics and atmospheric absorptions [34].

A number of application areas of mm-waves have emerged over the past few decades. Before the inception and proposal of 5G networks, applications related to satellite communications, mobile communications and automotive radars were utilizing the mm-wave band. In challenging terrains, tunnels and mines etc the communication systems were unmanageable and hazardous but the radiation diversity that multi-beam mm-wave antennas offer can provide better wireless connectivity to enhance productivity and ensuring human safety. The large bandwidth of the spectrum also enables the use of mm-wave frequency varying body security scanners between 10 GHz and 40 GHz through which high resolution imaging can be obtained that can be used to detect concealed objects which are otherwise not detected by metal scanners due to the advancement of 3D printed, non-metal, weapon and packaging technologies [36], [37]. Narrow beam scanning is preferred for radio astronomy and satellite services in the K-Band (18 GHz to 26.50 GHz) and SATCOM-on-the-move Ka-band (26.50 GHz – 40 GHz) applications in which high gain, frequency beam-scanning antennas are commonly used for long distance communications, positioning, geographical data, images and voice communication and

speed detection [38], [39]. In mm-wave automotive radars, traditionally, mechanical beam scanning is used but it renders the system with complex and costly architecture. Frequency scanning automotive radars in the mm-wave region offer high bandwidth, low cost and simplistic solution for collision detection, leading to minimisation and prevention of accidents, with wide beam-scanning coverage and high gain without any complex circuitry [40], [41].

5G NR is one of the most recent and talked about technology of mm-wave spectrum. The densification of the small-cell network is indeed a labour- and cost-intensive project but the economic and lifestyle benefits of shifting towards mm-wave technology outweigh the drawbacks. The small-cell technology will revolutionize the capacity in traffic congestion regions which will increase the number of radios and provide better signal intensity to solve the increasing video streaming and data rate intensive applications' demands. To put things in perspective, 5G has the ability to connect up to a million devices per square kilometre which is ten times the capacity of 4G.

Millimeter-wave Internet of things (IoT) is anticipated to be the driving force for connectivity across sectors and will be one of the major components of development of *Industry 4.0*. It will accelerate the manufacturing and logistics processes by enabling faster, wire-free and cost-effective communication to provide connectivity to industries such as renewable energy sector to develop smart grids and robots equipped with Artificial Intelligence (AI) technology. The remote operations features to monitor activity, machine-to-machine communications and checking and procuring inventory etc, will increase productivity and efficiency on factory floors and agricultural and livestock sectors, amongst others. The agricultural sector will also benefit from meteorological information

of millimeter-wave cloud radars (MMCR) [42].

The idea of connected environment is not limited to industries and businesses only. At the consumer end there will be a true smart and connected living, a glimpse of which we experienced in 4G communications with connected smartwatches, smart lights, smart homes and online shopping. Since 4G's capacity was exhausted leading to poor signal quality, 5G mm-wave communication qualifies to handle the existing and upcoming smart applications robustly. The healthcare sector, both at equipment and services end, will benefit from the mm-wave spectrum as well. With roundtrip latency around 10 ms, large bandwidth and highly reliable and secure 5G network, connected ambulance and emergency services will be able to transfer large amounts of data remotely through sensors and High Definition (HD) cameras to the hospital staff to give consultation to the crew and make pertinent arrangements before the patient arrives at the facility. It will also enable live virtual video consultations, remote patient monitoring and even remote collaboration of surgeons globally. The same HD video conferencing abilities apply to academic sectors as well where online education will support the students who are unable to travel will benefit from distant learning without experiencing any lag or jitters in the virtual classrooms.

Virtual Reality (VR) and Augmented Reality (AR) experiences are expected to be enhanced with 5G mm-wave communications. Until now, VR headsets did not gain the popularity they deserved because of the noticeable connection lags with rendered images having latency of more than 15 ms acting as catalyst for motion sickness [43]. The introduction of VR and AR in 5G mm-wave bands will unleash its true potential in healthcare, education, business and HD gaming. The technology can also be utilized in education

sector where science and medicine students can have an immersive experience to virtually perform experiments and practice complex procedures [44].

Intelligent transport system will also benefit with mobility in mm-wave spectrum. The Vehicle-to-everything (V2X) and Vehicle-to-Vehicle (V2V) sector will be able to design intelligent cars using mm-wave radars and antenna arrays to easily assist and coordinate with other vehicles on the road and detect objects and obstacles in fog and at night, with quick situation handling cases such as emergency braking, compared to cameras or Light Detection and Radar (LIDAR) technology [45].

It is expected that more applications areas will emerge, and industries will follow suit after regulation of spectrum and auction of mm-wave bands. While the requirements of mm-wave and 5G antennas for different applications are speculative and not standardized at this point, it is expected that multiband or wideband, high gain and directive antennas, with small form factor for integration and simplistic inexpensive structures, with ease-of-fabrication, will be desired by the industries in the future.

2.4 Microstrip Patch Antenna Array Configurations

The microstrip patch antenna was first introduced in the 1950's [46] but the first practical implementation on low loss substrate was performed in 1973 [47], [48] and since then has been studied extensively to utilize its characteristics in numerous wireless applications. When compared to other antennas, such as helix and reflector antennas, the microstrip patch antenna is extremely low profile and lightweight thereby occupying less space on the surface on which it is placed while also having the property to conform to the surface's aperture. It is because of these features that the microstrip patch antenna has

found its applications in the military domain where they are deployed in aircrafts, rockets and missiles etc [49]. These antennas have found their way in commercial industries as well such as Global Positioning System (GPS), satellite communications, cellular communications etc. The patch antenna is also capable of supporting multiple bands of frequencies and although it supports only narrow bandwidth, this limitation can be overcome with bandwidth enhancement techniques such as patch truncation [50], parasitic patches and shorting vias [51], using defected ground plane [52] and fractal geometries [53], [54]. The width of a rectangular patch antenna, W , can be calculated using equation (2.3) [55],

$$W = \frac{c}{2f_0 \sqrt{\frac{(\epsilon_r + 1)}{2}}} \quad (2.3)$$

where f_0 is the resonance frequency, ϵ_r is the relative permittivity of the substrate and c is the speed of light. The effective dielectric constant, ϵ_{eff} , is calculated as,

$$\epsilon_{eff} = \frac{(\epsilon_r + 1)}{2} + \frac{(\epsilon_r + 1)}{2} \left[1 + 12 \frac{h}{W} \right]^{-\frac{1}{2}}, \text{ if } \frac{W}{h} < 1$$

or,

$$\epsilon_{eff} = \frac{(\epsilon_r + 1)}{2} + \frac{(\epsilon_r + 1)}{2} \left\{ \frac{1}{\sqrt{1 + 12 \left(\frac{h}{W} \right)}} + 0.04 \left[1 - \left(\frac{W}{h} \right)^2 \right] \right\}, \text{ if } \frac{W}{h} < 1 \quad (2.4)$$

where h is the thickness of the substrate. Using equation (2.4), the effective length, L_{eff} , can be calculated,

$$L_{eff} = \frac{c}{2f_0 \sqrt{\epsilon_{eff}}} \quad (2.5)$$

The extension in length, ΔL , can be calculated using,

$$\Delta L = 0.412h \frac{(\epsilon_{eff} + 0.3) \left(\frac{W}{h} + 0.264 \right)}{(\epsilon_{eff} + 0.258) \left(\frac{W}{h} + 0.8 \right)} \quad (2.6)$$

The length of patch, L , can be calculated using equations (2.5), and (2.6),

$$L = L_{\text{eff}} - 2\Delta L \quad (2.7)$$

The guided wavelength, λ_g , on the substrate can be calculated using eq (2.8) and CST MWS has a built-in calculator as well,

$$\lambda_g = \frac{300}{f_{\text{GHz}}\sqrt{\epsilon_{\text{eff}}}} \quad (2.8)$$

In order to enhance the performance of the patch antenna, an array can be formed using as little as 2 antennas. The signals from the individual patch elements can be combined to increase the gain, cancel out unwanted signals and provide diversity reception [56]–[58]. The overall radiation pattern is determined using array factor which depends on the number and configuration of elements, their spacing, and phased and amplitude of the signal to each element [55]. Suited to a particular application, one of the three primary configurations can be adopted to design an antenna array: series, parallel or a combination of both series and parallel i.e., hybrid.

Figure 2.5(a) shows an example of parallel-feed configuration, also known as corporate feed configuration, in which all the elements are fed from a single source through a network of transmission lines. A power divider mechanism, such as Wilkinson or Bagley polygon, is usually deployed to split the power, either equally or unequally [59], to each element in the configuration. In this way, a squint-less, broadside radiation can be achieved by dividing each branch of the transmission line into equal lengths. In a series-fed array configuration, shown in **Figure 2.5(b)**, the antenna elements are linearly combined and fed using a common source through transmission line [60]. For an edge-fed series array, the signal travels through each element and an unequal power distribution is

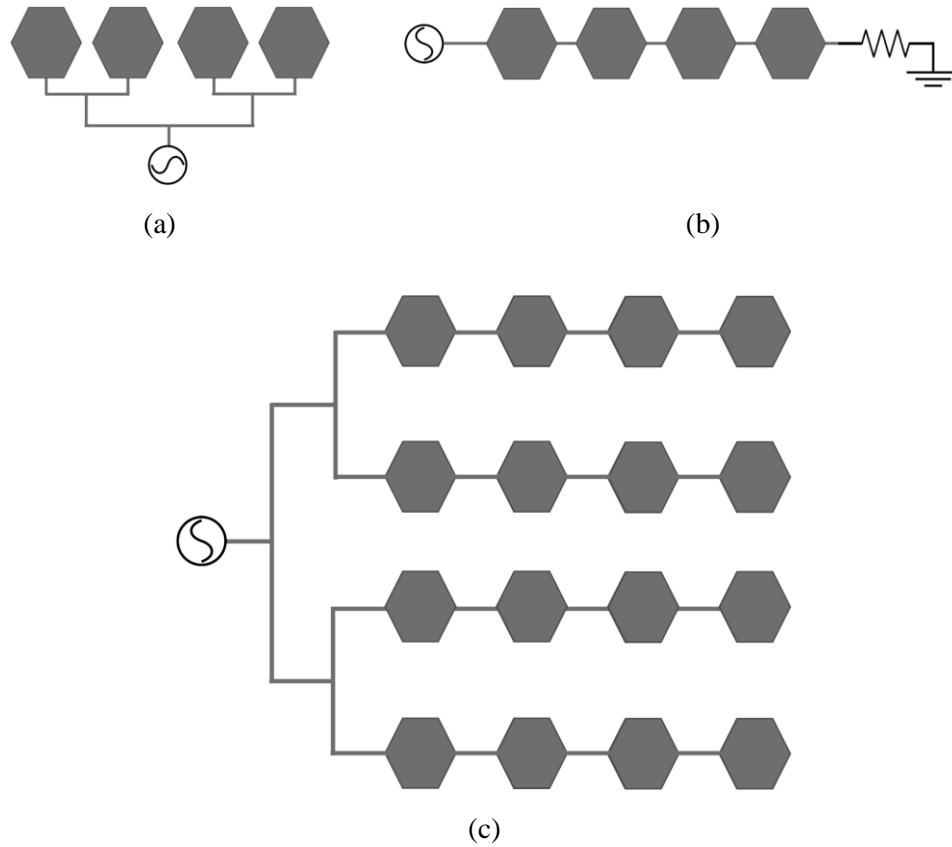


Figure 2.5. Array configurations (a) Parallel feed (b) Series feed (c) Hybrid feed.

observed when it reaches the last element. This results in a beam squint and the structure behaves as a traveling wave antenna in which frequency scanning is observed where the beam shifts with change in frequency. Compared to parallel-feed configuration, the series-fed array usually has a wide impedance bandwidth to support this frequency scanning feature [61]. A matched load is usually placed at the end of the structure to absorb the small amount of leftover energy after it has passed through all the elements in the array. In case of parallel-fed microstrip array, the quarter wavelength power divider transmission lines contribute to limiting the bandwidth of the structure. However, with equal power divider transmission line lengths, unlike the series-fed configuration, the same inter-element phase leads to no beam squint with change in frequency [49]. A combination

of both series- and parallel-feed combinations i.e., hybrid feed configuration, is shown in **Figure 2.5(c)**. Each branch power divider, similar to the parallel-feed structure, is used to feed an array of elements combined in series. Each series-fed sub-array has broader beamwidth but when collimated in hybrid-feed configuration, the bandwidth and gain increases but beamwidth becomes narrower [49]. Although fed from a common source through parallel-feed, the phase of individual row of series-fed array can be controlled.

2.5 Leaky-wave Antennas

Leaky-wave antennas (LWAs) were first introduced in 1940 when W. W. Hansen proposed a rectangular waveguide-based traveling-wave antenna [62] but the detailed theory of this class of antennas was not pioneered until 1984 [63]. The LWAs fall into the category of traveling wave antennas in which the wave, that propagates along the guiding structure, produces radiation [64] and, owing to the structure's size, are able to produce narrow fan-beam radiation patterns. The IEEE standard 145-2013 defines an LWA as “An antenna that couples power in small increments per unit length, either continuously

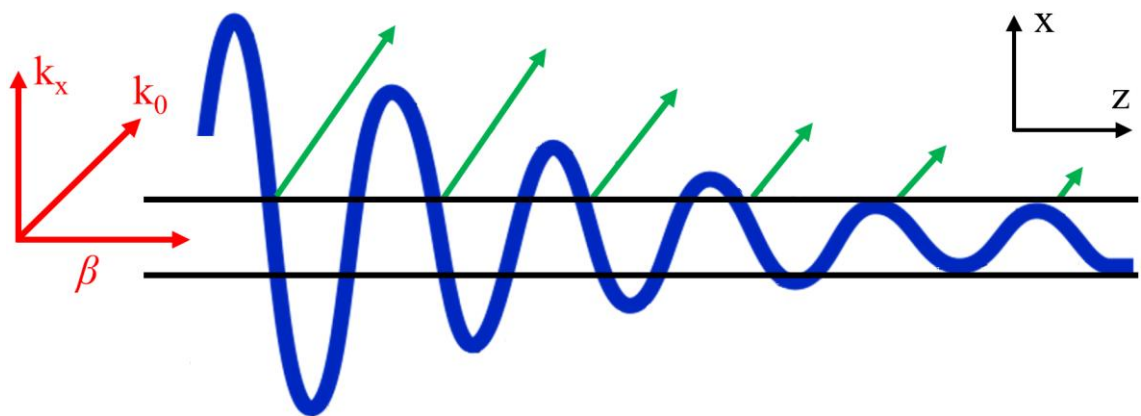


Figure 2.6. Representation of leaky-wave antenna and radiation principle.

or discretely, from a traveling-wave structure to free space” [65]. The simplistic feed mechanism of the LWAs, and the ability to scan the beam with frequency shift, gives them the advantage to be adopted for applications in the mm-wave band.

Unlike the transmission line structures in which the wave propagates in the longitudinal direction, the leaky modes of LWAs’ propagation phenomenon occur inside the open guiding structure while simultaneously radiating power in the space provided the propagation conditions are met [66]. **Figure 2.6** shows a guided wave, with phase constant, β (radians/m), propagating in the longitudinal z direction. The leaky-wave has a complex propagation constant in the wave’s propagation direction, written as

$$\gamma = \alpha + j\beta \quad (2.9)$$

where α is the attenuation or leakage constant (Nepers/m). The relationship between the propagation constant of the leaky-wave produced in the x direction, k_x , and β can be written as

$$k_x^2 = k_0^2 - \beta^2 \quad (2.10)$$

where $k_0 = 2\pi/\lambda_0$, free-space wavenumber, represents the radiating wave’s phase constant. From the above equation, a leaky-wave can be observed to radiate into space if the perpendicular propagation constant, k_x , is a real number, the phase velocity is faster than light velocity ($v_p > c$) and the fast-wave condition is satisfied, i.e.,

$$\left| \frac{\beta}{k_0} \right| < 1 \quad (2.11)$$

In the case where $\beta > k_0$ and k_x is an imaginary number, it is referred to as slow-wave or guided wave [63].

The LWAs can be classified into several categories depending on their operating principles or geometry of the structures. LWAs can be one- or two-dimensional geometries and can be divided into uniform and periodic structures. The uniform LWA's structure remains unaltered in the longitudinal direction of propagation. The waveguiding structure, when open, supports a fast leaky mode and produces radiation. Such structures have the ability to radiate scan angles in only one quadrant i.e., broadside to forward endfire direction [67], [68]. Periodic LWAs, shown in **Figure 2.7**, are a sub-class of LWAs that have fan-beam frequency scanning radiation in backward and forward endfire direction. The dominant mode of the periodic structure is slow-wave, where the phase constant is greater than the free space wavenumber ($\beta > k_0$), which means that the dominant mode itself does not produce any leaky-waves rather it is the periodic modulations of the array that produces radiation along the length of the structure [68]. According to Floquet's theorem, the wave in a periodic structure has an infinite number of space harmonics [69].

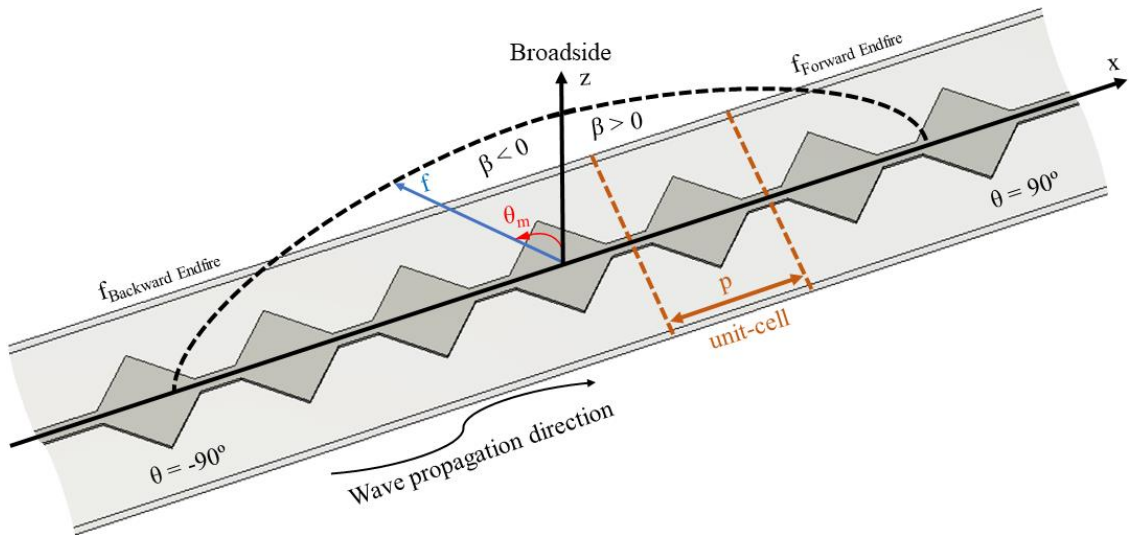


Figure 2.7. An example of an infinitely long periodic LWA showing unit-cell's period, p , and scanning directions in backward and forward endfire regions.

Each space harmonic is characterized by phase constants β_n

$$\beta_n = \beta_0 + \frac{2\pi n}{p}, \quad n = 0, \pm 1, \pm 2, \pm 3 \dots \quad (2.12)$$

where β_0 is the fundamental space harmonic, n is the n th number Floquet mode and p is the period of the unit cell. For directive frequency scanning applications, a single beam is usually required, therefore the antenna structure is designed so that the first Floquet mode, i.e., $n = -1$, is fast such that (2.12) becomes

$$\beta_{-1} = \beta_0 - \frac{2\pi}{p} \quad (2.13)$$

The scanning beam direction of the periodic LWA can be determined using

$$\theta_m \simeq \sin^{-1} \left[\frac{\beta_{-1}}{k_0} \right] \quad (2.14)$$

where θ_m is the angle of the main beam, measured from broadside. As the frequency tunes up, the antenna's main beam scans from backward endfire, through Open StopBand (OSB) at broadside, to forward endfire. The thickness of the substrate plays a key role in scanning as thicker substrate increases unwanted radiation from the edges as a result of surface wave scattering that, ultimately, effects the antenna's gain adversely [70].

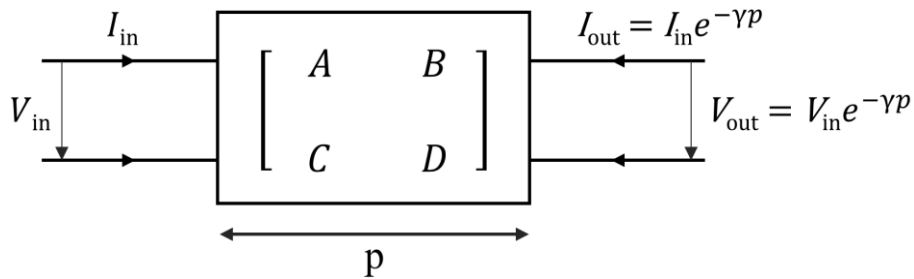


Figure 2.8. Equivalent two-port representation of periodic LWA's unit-cell by ABCD matrix.

For an infinitely long periodic structure, the unit-cell can be modelled as a two-port network. **Figure 2.8** shows the characterization of the unit-cell, shown in **Figure 2.7**, by

its ABCD parameter matrix resulting in equation (2.15),

$$\begin{bmatrix} V_{in} \\ I_{in} \end{bmatrix} = \begin{bmatrix} A & B \\ C & D \end{bmatrix} \begin{bmatrix} V_{out} \\ I_{out} \end{bmatrix} = \begin{bmatrix} A & B \\ C & D \end{bmatrix} \begin{bmatrix} V_{in}e^{-\gamma p} \\ I_{in}e^{-\gamma p} \end{bmatrix} \quad (2.15)$$

Equation (2.15) can be simplified to obtain propagation constant, γ , which, for a periodic structure, describes the characteristics of the propagating wave,

$$AD + e^{2\gamma p} - (A + D)e^{\gamma p} - BC = 0 \quad (2.16)$$

which is further simplified to yield [71],

$$\cos \gamma p = \frac{A + D}{2} \quad (2.17)$$

The above equation can be used for extraction of dispersion characteristics from CST Studio by deploying two ports at either edge of the unit-cell and substituting the resulting scattering parameters with the ABCD parameters [71]. The resultant equation will be,

$$\beta = \frac{1}{p} \left[\cos^{-1} \left(\frac{1 - s_{11}s_{22} + s_{21}s_{12}}{2s_{21}} \right) \right] \quad (2.18)$$

The impedance at the ports can be derived by concatenation of ABCD matrix and Floquet theorem [71]

$$Z_B^{\pm} = \pm \frac{BZ_0}{\sqrt{A^2 - 1}} \quad (2.19)$$

In equation (2.19), it is assumed that the structure is symmetric, and the sign represents the direction of propagation of the traveling wave.

2.6 Simulation and Modelling Tools

The research presented in this thesis is conducted using a 3D electromagnetic simulation software, CST Microwave Studio Suite. CST is an efficient tool that offers design solutions for high frequency 3D structures such as antennas and other multilayer geometries, while offering electromagnetic analysis, material property configurations and taking into account space, metallization, ohmic and other losses. Antennas come in different form factors with some having more discontinuities than others. To cater the geometric refinements for electromagnetic analysis, CST offers two discretizing solutions, namely tetrahedral meshing and hexahedral meshing, to take into account the effects of each element in terms of S-Parameters, radiation patterns, gain, efficiency and current distribution etc.

There are several other commercial modelling and simulation tools available and utilized by antenna engineers globally. FEKO is a Method of Moment (MoM) based 3D solver and it combines other techniques such as multilevel fast multimode method (MLFMM), geometric optics approach (GO) and unified theory of diffraction (UTD) to compute complex matrix elements by deploying tetrahedral mesh for volume discretization and triangular mesh for surface discretization [72], [73]. While FEKO is efficient, it does not support the combination of multilayer substrate and dielectric bodies [74]. Ansys Electronics Desktop (formerly HFSS) was one of first tools released for commercial antenna engineers and still is one of the most widely used tools in the industry for Finite Element Method (FEM) based solver calculations [74], [75]. It has adaptive mesh refinement features for all the design layers and generates results in S-, Y- and Z-parameters along with visualization of 2D and 3D far field results. Empire XPU deploys Finite Difference Time Domain (FDTD) technique providing very fast simulations with accelerated

kernel to model multi-layered and planar geometries [72], [76]. All of these full-wave solvers have market penetration and are used widely in academic and commercial environments however the licensing cost of these solvers is very high. The fact that the research in this thesis is conducted using CST, and its details are extensively discussed, does not undermine the credibility of other commercially available software but the main motivation of choosing CST was the availability of licence to the research lab.

First proposed in 1976, the Finite Integration Technique (FIT) is the numerical computational methodology adapted in CST in which Maxwell's equations' integral form is discretised to analyse electromagnetic fields in time and frequency domains [77]. The role of CST Studio Suite, in the modelling, simulation parametric analysis, and optimisation of the antennas, is shown in **Figure 2.9**. Suited to a particular geometry and application, CST offers different high-frequency solvers, namely, Time (Transient) Domain, Frequency Domain, Integral Equation, Multilayer, Asymptotic and Eigenmode solver. For planar antennas, Transient and Frequency Domain modules are popular solvers amongst

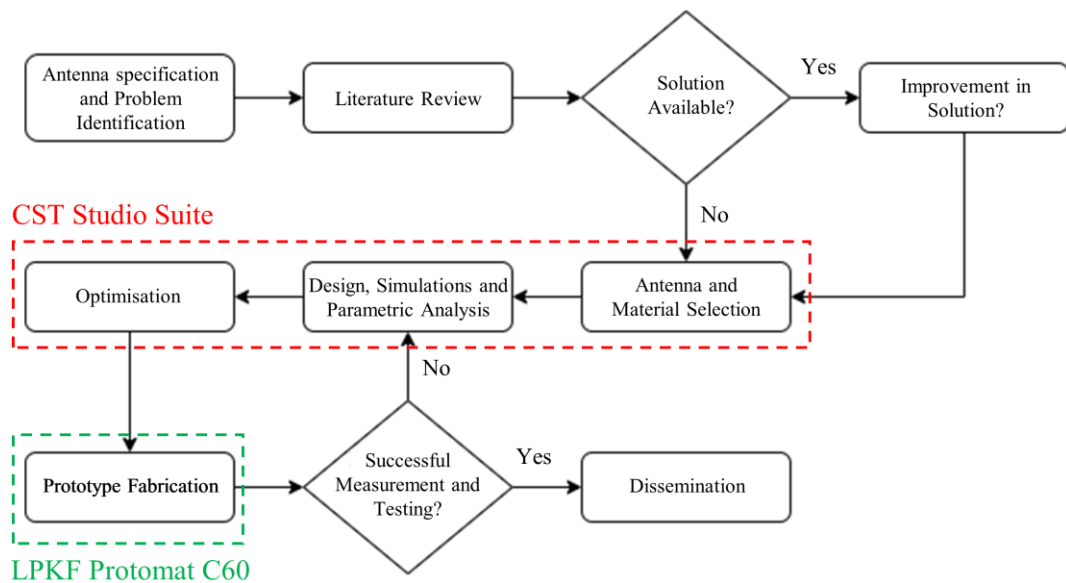
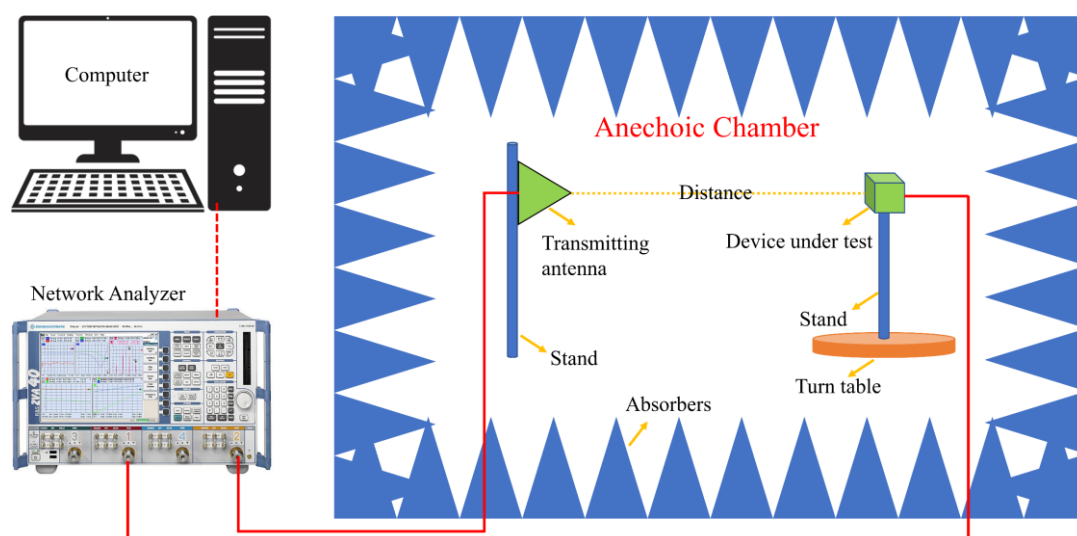


Figure 2.9. Flowchart of Research methodology.

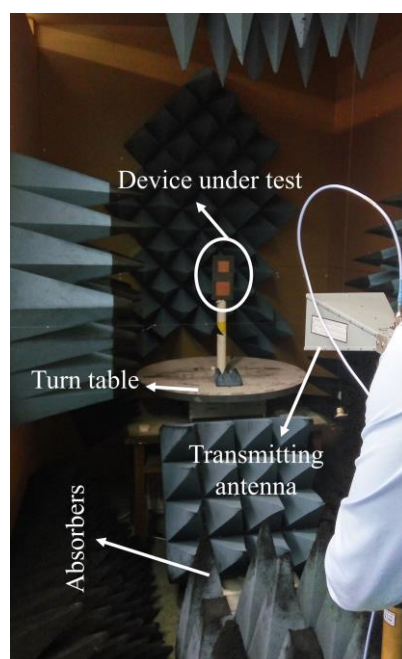
antenna engineers and, of these modules, the Transient domain is the flagship solver of CST MWS which calculates the broadband behaviour across the frequency range with an arbitrarily fine frequency resolution [72]. The other type of frequently used solver in CST is Frequency Domain in which a frequency sweep is performed based on a small number of frequency samples and, therefore, frequency samples are chosen adaptively for which minimum number of equation system is setup. The Time Domain solver is suited to applications such as high frequency antennas, transmission lines and connectors whereas the Frequency Domain solver is efficient for strongly resonant structures which would, otherwise, have long time-domain signals settling time [78]. There are two major excitation signal sources for the calculation of parasitic parameters and field distribution in CST: Discrete port and Waveguide port. The discrete port comprises of a current source with internal resistance and is placed inside the structure. The waveguide port, used in this research, simulates a waveguide, infinite in length, contacting the structure's edge usually. It has high simulation accuracy, with default input signal power of 1W, having mode matching capability and absorption of returning power in the structural model. By default, CST MWS has gaussian pulse signal defined which requires f_{min} and f_{max} inputs for appropriate mesh creation. Gaussian pulse is efficient in frequency and time domain transient solvers and avoids divisions of S-parameter computations with zero [78].

2.7 Measurement Setup

The accuracy of simulation and optimisation of the antenna is measured through in-house fabrication facility and measurement setup at Antenna and High Frequency Research Centre shown in **Figure 2.10**. Antennas are fabricated using LPKF Protomat C60 that has



(a)



(b)

Figure 2.10. Measurement setup at Antenna and High Frequency Research Centre (AHFR)

(a) Block diagram (b) Anechoic chamber.

the track cutting precision of 4 mils (~ 0.10 mm), with separation of 4 mils, and drilling precision of 8 mils [79]. The measurement and testing facility consists of Device Under Test (DUT), Standard Gain Horn Antenna (SGH) and a partially anechoic chamber as

shown in **Figure 2.10(a)**. The DUT is the fabricated antenna placed on top of a stand and supported by purpose-built polystyrene foam to support the weight of the cable and align the position of the antenna with SGH, which is the transmitting antenna (Schwarzbeck-BBHA 9170) [80], in the anechoic chamber shown in **Figure 2.10(b)**. The alignment of the centres of the SGH and DUT is carried out using laser beams. The DUT and stand setup is centred on a turntable which has the ability to rotate 360° in Azimuth. The absorbing materials in the anechoic chamber are strategically placed on the walls and the roof to absorb approximately all the incident electromagnetic radiation and provide a near free space environment.

The cables connected to both DUT and SGH are then connected to a Vector Network Analyser (VNA), *Rohde & Schwarz ZVA40*, in the control room outside of the anechoic chamber [81]. The VNA has the frequency range of 10 MHz to 40 GHz and for each antenna, it needs to be calibrated which, in our case, was performed using the calibration kit provided by Rohde & Schwarz in the steps of 100 MHz for the frequency range of the AUT. Using the phase and amplitude measurements, the VNA calculates complex S-Parameters, VSWR and real and imaginary impedances.

The VNA is connected to a computer in the control room, through which it can be controlled, and it has a proprietary software to gather the measurement data of radiation patterns and control the turntable in the anechoic chamber.

Chapter 3

Millimeter-Wave Patch Array Antenna on Curved Substrate

3.1 Introduction

The expansion of the wireless industry around the globe has enabled people to access the internet and the demand for high-quality wireless communications systems is growing exponentially. This rapid growth demands for high data rates and overcoming challenges including capacity issues to accommodate more users and applications which require quick and quality research in order to develop next generation wireless communications systems. The mm-wave spectrum is most likely to be the potential candidate to implement the 5G communication applications because of its wide bandwidth [5]. The introduction of the mm-wave band for 5G applications has brought considerable attention to the researchers in order to analyse and design antennas which are reported in several papers [61], [82]–[84]. Other works include dielectric superstrate and Electromagnetic BandGap (EBG) ground structure to improve radiation characteristics in 5G [83] and phased arrays [84]. A review for several 5G antennas was presented in [61]. In [85], a multi-band split ring resonator was proposed which covers 6 GHz band which is also expected for

5G communications [86].

Microstrip patch antennas are widely used for antenna design applications for wireless communications because they can be made with different shapes, such as square, rectangle and circle etc, are compact, easy to fabricate and lightweight with low manufacturing costs. The shapes of microstrip antennas can be modified with slots [87] and trimming of edges to obtain desirable results [50], [88]. Suited to a particular installation, microstrip patch antennas also support different feed mechanisms depending on the availability of space, can be used in formation of arrays and designed for different type of radiation patterns. These reasons are compelling to use microstrip antennas as candidates for mm-wave applications. Several microstrip patch antenna techniques have been deployed and used for mm-wave communications recently [82], [89], [90].

As discussed in Chapter 2, series and corporate feed configurations can be deployed to form arrays of microstrip antennas. In [91], a 4×4 series-fed microstrip patch array is presented for 28 GHz communications and in [92] an unequally spaced series-fed antenna is shown to improve sidelobe level. Corporate feeding technique for microstrip patch arrays is widely used to obtain high gain and broadside radiation pattern. 4×1 and 2×2 stacked patch arrays, on LTCC and PCB substrates, with a maximum gain of 13.0 dBi, are presented in [82]. A high gain 2×2 patch antenna array with high gain and high efficiency is demonstrated in [90]. Some researchers have combined the series and corporate networks recently to reduce sidelobe levels and achieve other desired results [93], [94].

In this chapter, two corporate-fed configurations of microstrip patch array antenna are presented. The first antenna is a 4×2 planar microstrip array with rear feeding designed on Rogers RT/duroid 5880 substrate. The spacing between the elements plays a key role

in the resonant frequency and the performance of the antenna. When compared with flexible substrates such as PET film and LCP substrates, the Rogers RT/duroid 5880 is often categorized as a rigid substrate [95] but it is not as rigid as other commonly used laminates for antenna design such as FR4 epoxy/glass [96]. A study on effects of bending two-dipoles on LCP substrate is presented in [97] and a UWB directional antenna placed conformally on a cylindrical pipe section is reported in [98]. Curving 5-element and 9-element microstrip patch array conforming on a cylinder using genetic algorithm, for conformal applications, are presented in [99], [100]. A comparative study on bent and planar microstrip patch antenna, between 1 GHz and 8 GHz on FR-4 substrate with relative permittivity of 4.3, is presented in [101] which shows that for increasing the radius of cylindrical concave bending from 5 mm to 10 mm, the antenna still operates on the resonant frequency of 4.591 GHz but with decrease in angular width in the plane of bending. In [102], for gradual increase in radius of concave cylindrical bending, a downward shift in resonant frequency was observed for 1×2 and 1×4 conformal microstrip patch antenna array designed at 16 GHz and upward tuning was observed for larger bends. The second proposed design, in this chapter, focuses on the novel study to observe effects of mechanically curving the substrate on the microstrip antenna array's performance in terms of frequency tuning, gain variation and changes in radiation characteristics for the operating frequency range. For realistic results, the edge-feeding mechanism is adopted for the curved substrate and the results for concave and convex bending are presented. The aim of mechanical curving is threefold: first, to test the tolerance of the substrate for deformations in either direction, apart from the well-known manufacturing tolerances such as cable and connector losses and milling machine and anechoic chamber limits etc, which will also help in fabrication and handling of future development of antennas, presented in

subsequent chapters; second, to explore the frequency tuning feature; and third, to see the suitability of the design for mm-wave conformal applications for which the antenna is curved up to -30° and results are observed.

3.2 Microstrip Patch Antenna

3.2.1 Initial Single-Element Modelling

In order to design an array of microstrip patch antennas, a single-element patch antenna for 28 GHz communications is shown in **Figure 3.1**. Instead of using a microstrip line, the antenna is fed with a probe at the center of the inset which is placed symmetrically along the width of the antenna. The antenna has full ground plane to minimize radiation from the back of the structure and making the radiation as directive, towards the broad-side, as possible. Rogers RT/duroid 5880 substrate, with double-sided copper cladding having relative permittivity of 2.2 and loss tangent of 0.0009, is used to design the antenna. The overall dimensions of the antenna are $10 \times 10 \times 0.254$ mm³.

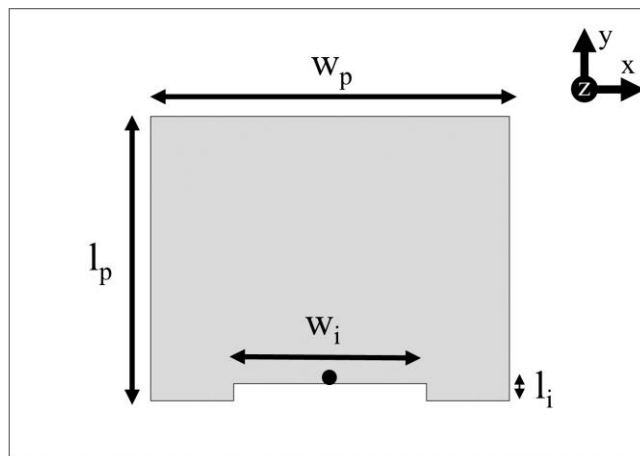


Figure 3.1. Geometry of rear-fed microstrip patch antenna.

3.2.2 Parametric Variations and Discussion

The parametric variations of the antenna geometry, presented in **Figure 3.1**, are discussed in this section. The physical connector's effects and losses are not considered for these simulations because these simulations are performed to observe frequency tuning and impedance matching behaviour of each parameter to be later incorporated into an array which will be discussed in **Section 3.3**. The losses associated with the connector will be taken into account in the analysis and results of the array antenna.

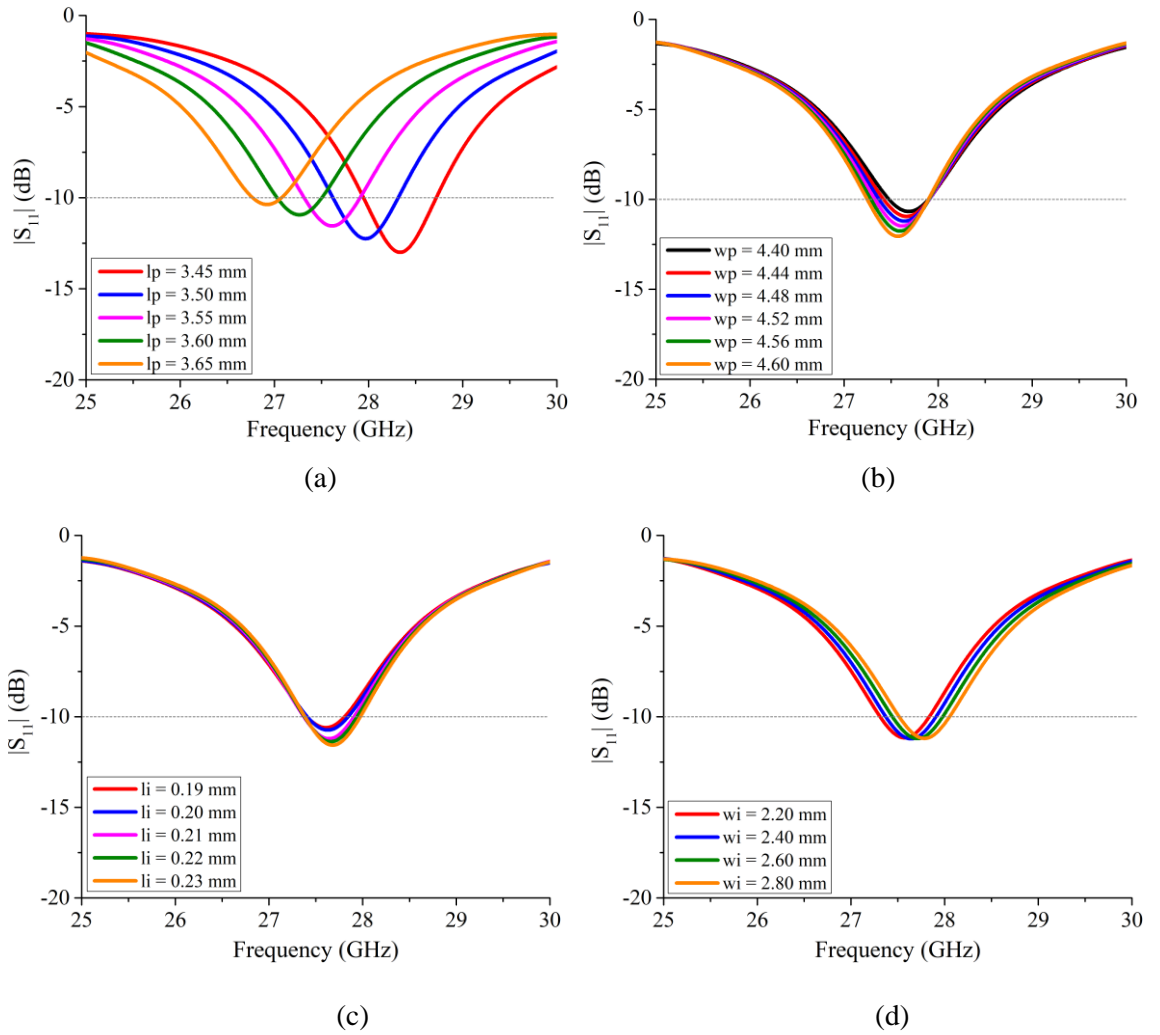


Figure 3.2. $|S_{11}|$ of patch antenna with inset varying (a) l_p (b) w_p (c) l_i (d) w_i .

The parametric analysis of the microstrip patch antenna is presented in **Figure 3.2(a)-(d)**. All simulations are performed by varying the parameter in discussion and keeping others constant. **Figure 3.2(a)** shows the effect of varying length of the patch, l_p , on the $|S_{11}|$ response. With each 0.05 mm variation between 3.45 mm to 3.65 mm, the antenna tunes down by approximately 380 MHz in the 28 GHz range. While the overall profile of the response does not change, the increase in l_p by 0.05 mm also improves the impedance matching and increases bandwidth. The effect on the $|S_{11}|$ response by varying the width of the patch, w_p , is presented in **Figure 3.2(b)**. The increment by 0.04 mm in w_p between 4.40 mm and 4.60 mm improves the impedance matching and the bandwidth of the antenna increases by approximately 90 MHz.

Figure 3.2(c) presents the variation of the vertical length of the inset in the patch, l_i , and its effects on performance of the antenna. The increase in l_i improves the impedance matching and increases the bandwidth but contrary to increment in w_p , this improvement in bandwidth comes as a result of better impedance matching in the upper frequency whereas in the other case, presented in **Figure 3.2(b)**, the bandwidth improved in the lower frequency limit. **Figure 3.2(d)** shows the effect variation of inset's horizontal length, w_i , on $|S_{11}|$. The antenna is not as sensitive to change in w_i as with other variations and a 0.20 mm increment, between 2.20 mm and 2.80 mm, tunes the frequency up by around 60 MHz with little to no improvement in impedance matching and bandwidth.

The 3D radiation pattern plot of the antenna is shown in **Figure 3.3**. The radiation pattern plot is observed at 27.20 GHz having peak realized gain of 7.44 dBi. As expected with the full ground plane, the radiation pattern is directive at broadside with wide HPBW of 73.2° in xz-plane, 69.6° in yz-plane and sidelobe level of -19.0 dB.

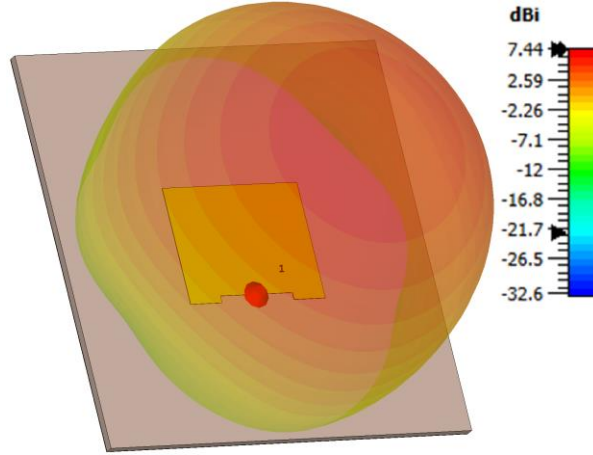


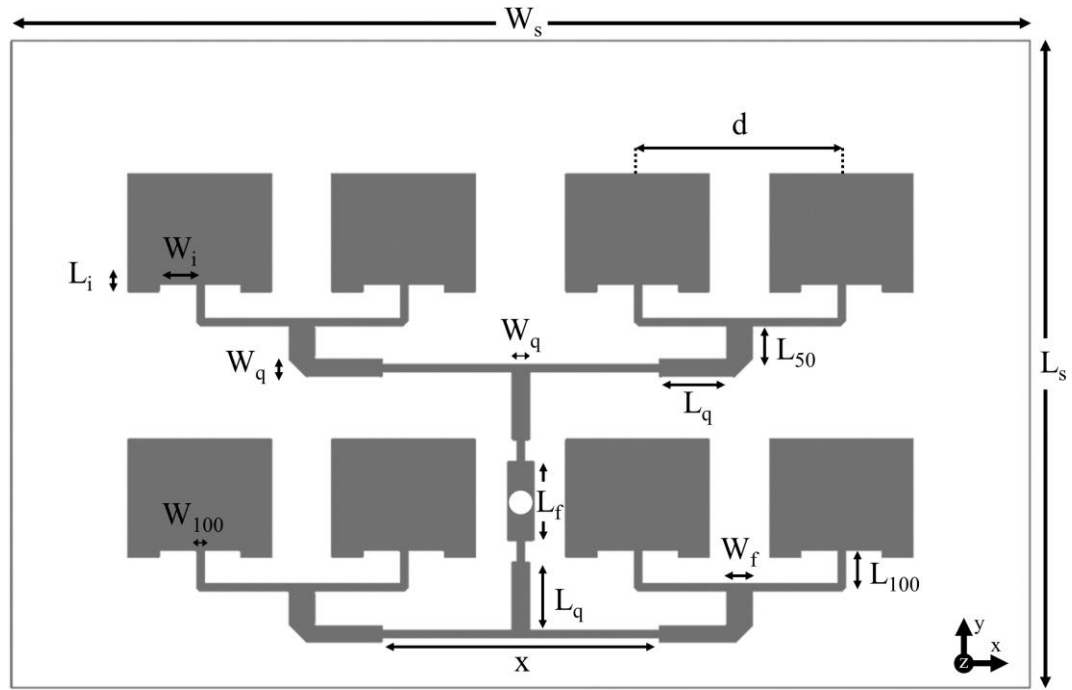
Figure 3.3. 3D radiation pattern of microstrip patch antenna with inset at 27.40 GHz.

3.3 4×2 Center-Fed Microstrip Patch Antenna Array

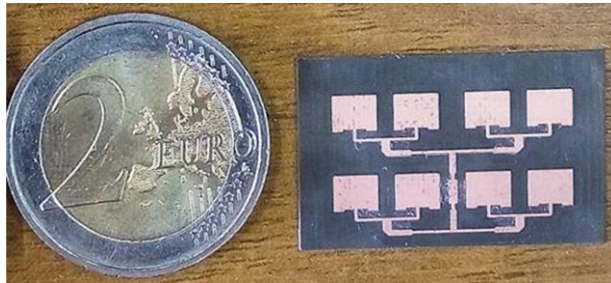
3.3.1 Transmission Line Network Design and Array Geometry

A 4×2 corporate-fed array of the microstrip patch geometry, based on **Figure 3.1**, is presented in **Figure 3.4**. The array consists of 8 microstrip patch antennas with a spacing of approximately 0.75λ between the row elements, represented by d . The probe feed is replaced by a microstrip feed, and each patch is connected to a $100\ \Omega$ line, joining another $100\ \Omega$ line from the adjacent patch and then to a matching arrangement using quarter wave transformers (approximately $70\ \Omega$). All the bends in the design are mitred for better efficiency. The two rows of the array are connected through a network of one wavelength transmission line which includes two-quarter wave transformers and a $50\ \Omega$ pad to which the connector is soldered from the bottom through a 0.5 mm via hole. The dimensions L_i and W_i are optimised for high frequency to make realistic fabrication on the LPKF Protomat C60. The proposed antenna is simulated using CST Microwave Studio Suite with a $50\ \Omega$ modelled SMK connector and fabricated using 0.254 mm thick Rogers RT/duroid

5880 substrate [103]. **Table 3.1** shows the design parameters of the antenna in detail.



(a)



(b)

Figure 3.4. 4×2 element rear-fed array (a) Geometry (b) Prototype.

Parameter	Symbol	Dimension (mm)
Substrate width	W_s	30.0
Substrate length	L_s	19.0
Patch width	W_p	4.48
Patch length	L_p	3.55
Inset width	W_i	1.10
Inset length	L_i	0.20
Quarter-wave transformer width	W_q	0.48
Quarter-wave transformer length	L_q	1.99
Feed width	W_f	0.8
Feed length	L_f	2.30
100 Ω line width	W_{100}	0.20
100 Ω line length	L_{100}	1.11
Element spacing	D	6.0
Mid column spacing	X	8.17

Table 3.1. Optimised design parameters of the proposed antenna array.

3.3.2 Parametric Analysis, Results and Discussion

The effect of the spacing between the patch elements in the array, d , on the $|S_{11}|$ is shown in **Figure 3.5**. The frequency response tunes down and the bandwidth decreases as the spacing between the elements increases from 0.75λ to 3λ . The increase in the distance also results in impedance mismatching. From λ to 3λ , between 26 GHz and 29 GHz, there are additional resonances and mismatching at resonance frequencies observed. The optimisation at approximately 0.75λ , i.e., when d is 6.0 mm, the antenna array has $|S_{11}|$ centred at 27.40 GHz.

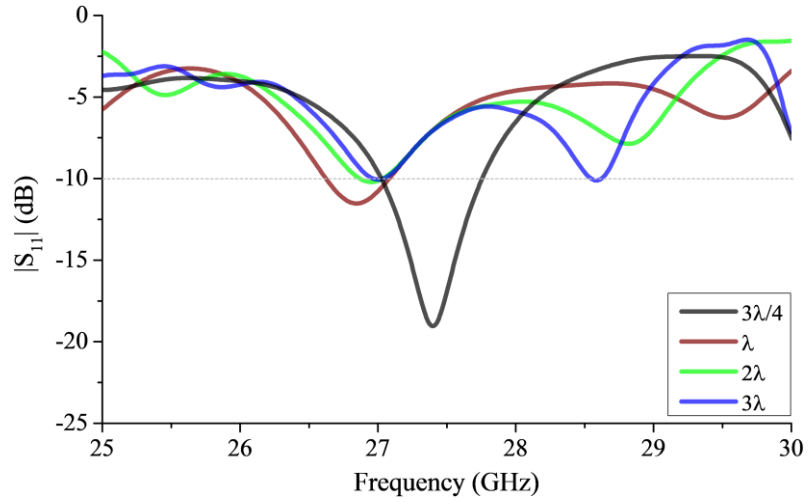


Figure 3.5. Parametric analysis with element spacing.

3.3.2.1 Impedance Bandwidth

The simulated and measured $|S_{11}|$ of the antenna array are presented in **Figure 3.6**. The antenna array is measured using Rohde and Schwarz Vector Network Analyzer (ZVA40) and shows good agreement with the simulated results. The simulated results show that the antenna has $|S_{11}| < -10$ dB between 27.04 GHz and 27.71 GHz centred at 27.40 GHz with fractional bandwidth (FBW) of 2.44%. The measured results show that the antenna

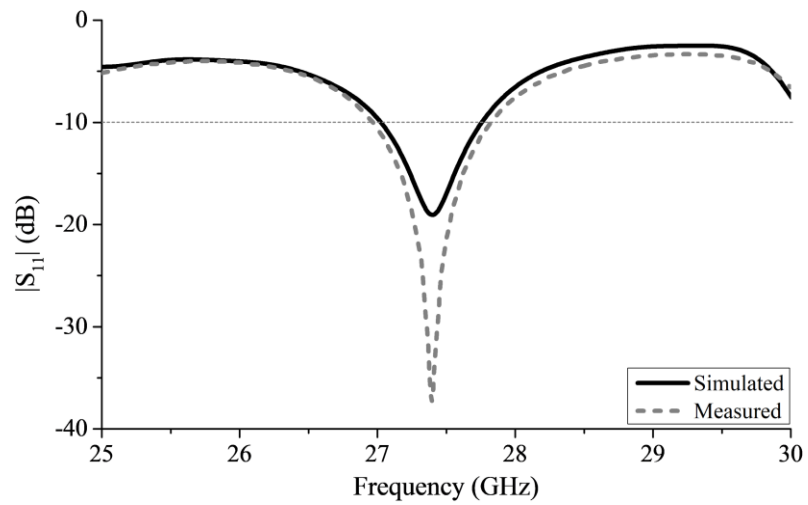


Figure 3.6. Simulated and measured $|S_{11}|$ at 27.40 GHz.

is operating between 26.97 GHz and 27.82 GHz with a minimum value of $|S_{11}|$ at 27.40 GHz. The measured FBW is more than 3.1%.

3.3.2.2 Efficiency

The simulated radiation and total efficiencies of the array are presented in **Figure 3.7**.

The radiated efficiency in all directions can be calculated using (3.1) [104]:

$$\eta = \frac{P_r}{P_{IN}} \quad (3.1)$$

where P_r is the radiated power in all directions and P_{IN} is the input power of the antenna at the port. The total efficiency of the antenna also includes the input mismatch and antenna losses. At 27.40 GHz, the antenna has the maximum efficiency and the percentage of the power to the antenna to the power radiated from the antenna is more than 85%.

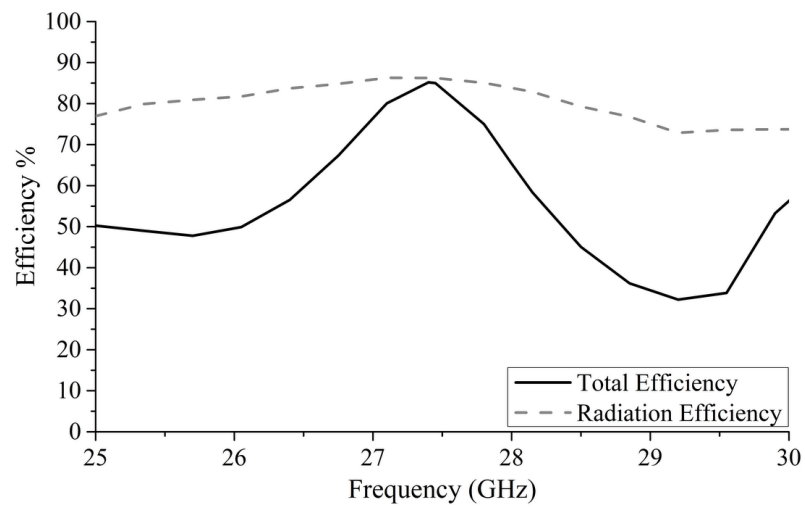


Figure 3.7. Simulated total and radiation efficiency.

3.3.2.3 Realized Gain

Figure 3.8 shows the measured and simulated realized gain of the array antenna, which is one of the key parameters to define the performance of mm-wave antenna, as it takes into account mismatch losses between antenna impedance and transmission line. It is observed that the array has a high measured gain between 27.0 GHz and 28.0 GHz with a peak gain of 16.10 dBi at 27.40 GHz. The simulated gain at 27.40 GHz is 15.80 dBi.

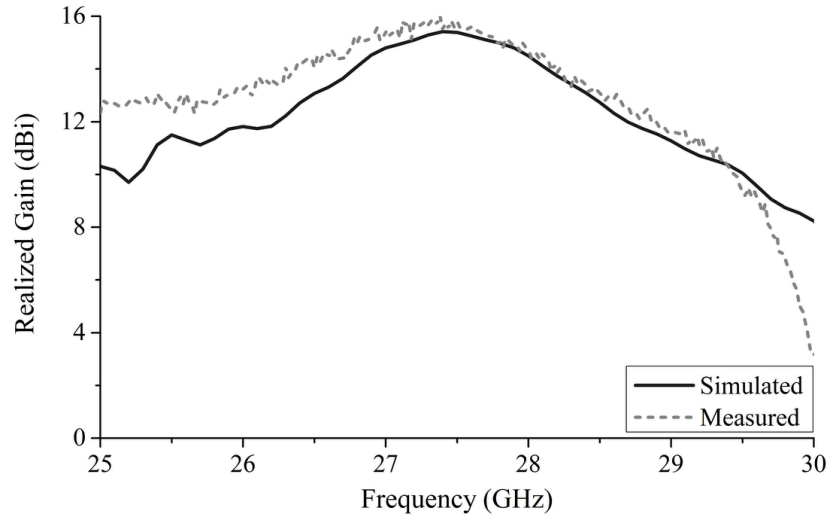


Figure 3.8. Simulated and measured gain for the 4×2 array.

3.3.2.4 Radiation Pattern

The simulated and measured polar plots are shown in **Figure 3.9**. **Figure 3.9(a)** shows the polar plot for xz-plane of the antenna. The antenna has 20° HPBW and SLL of -11.60 dB in xz-plane. **Figure 3.9(b)** shows the polar plot in the yz-plane. The radiation pattern, tested in an anechoic chamber, has a directive radiation pattern with a HPBW of 35° in yz-plane. The squint visible in the yz-plane of the rear-fed antenna array is a result of the addition of quarter-wave transformers or microstrip lines [105] and the asymmetry of the 50 Ω feeding pad with respect to the top and bottom row of elements. The 3D

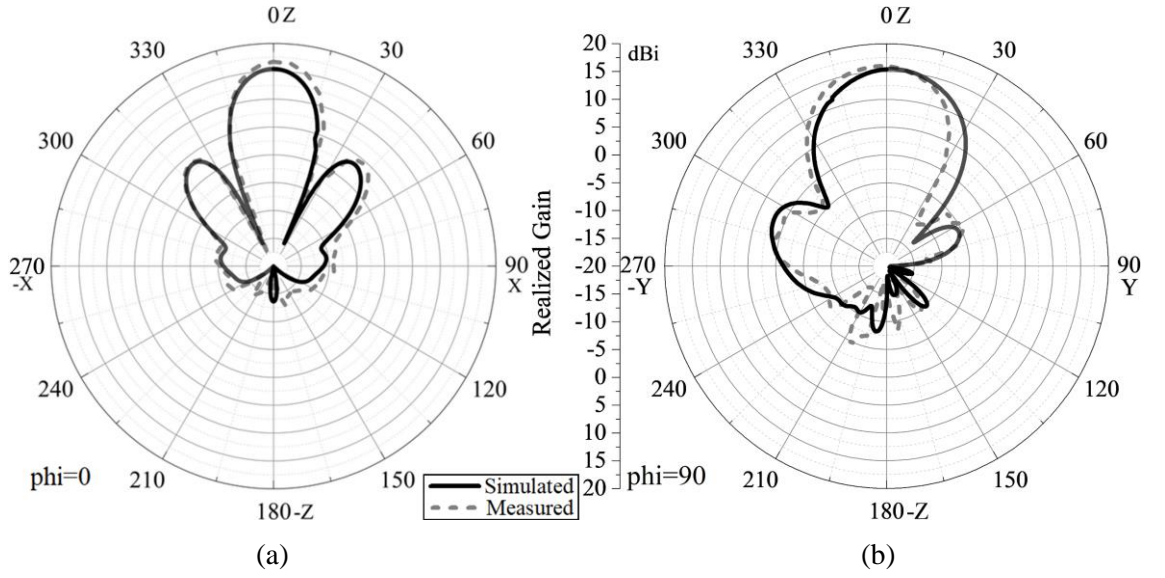


Figure 3.9. Simulated and Measured polar plots at 27.40 GHz (a) xz-plane (b) yz-plane.

radiation pattern at 27.40 GHz is shown in **Figure 3.10**. The antenna array has one single beam normal to the planar structure and it further verifies the simulated peak gain at 27.40 GHz to be 15.80 dBi.

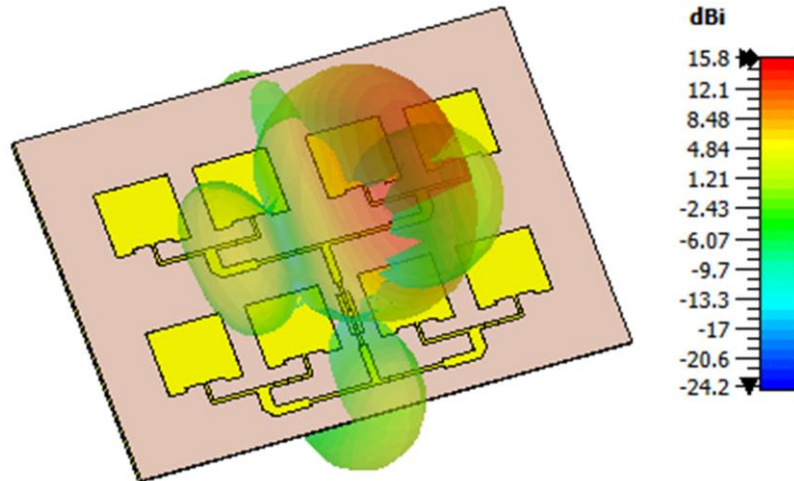


Figure 3.10. 3D Radiation pattern of rear-fed microstrip patch antenna array at 27.40 GHz.

3.3.2.5 Current Distribution

In order to examine the radiation response of the antenna, the surface current distribution across the antenna's bandwidth should be analysed but since we know that the antenna has a fixed broadside radiation pattern and for simplicity of the analysis, the surface current distribution at 27.40 GHz, where the antenna has peak realized gain, is presented in **Figure 3.11**. It is observed that the current density in each patch element is identical and uniformly distributed thereby contributing to broadside radiation pattern.

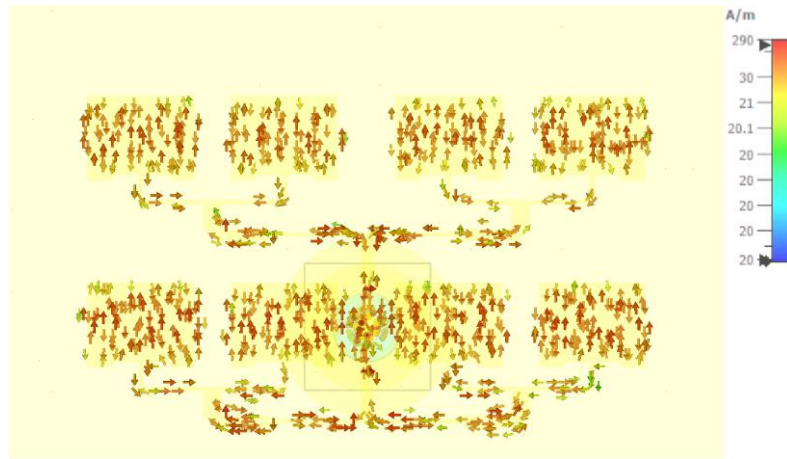


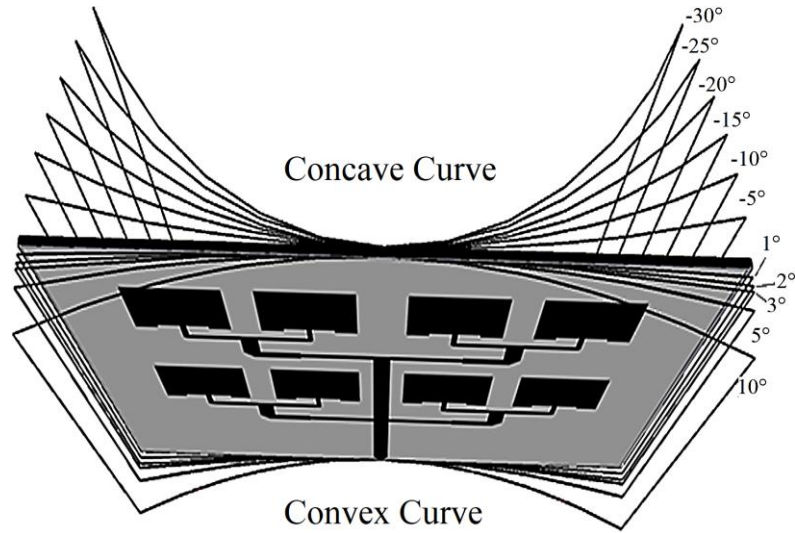
Figure 3.11. Surface current distribution at 27.40 GHz at phase = 0°.

3.4 Edge-Fed Microstrip Patch Antenna Array on Curved Substrate

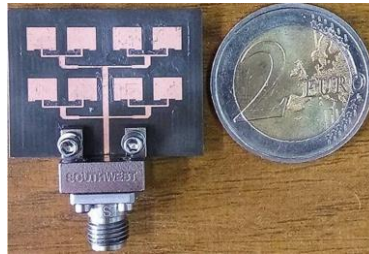
3.4.1 Modelling of Antenna

The effects of mechanically curving the substrate on matching and radiation properties were studied to determine tolerances. With the configuration shown in **Figure 3.4**, it is not realistically possible to curve the substrate because of the soldered connector at the

bottom of the antenna. However, some arrays may have edge fed connectors and an array shown in **Figure 3.12(a)** was prototyped. In place of the feed line connecting the two rows of the array shown in **Figure 3.4**, a $50\ \Omega$ line is introduced which connects the two rows with a one wavelength line and the feed line extends to the edge of the substrate. The edges of the line are tapered to avoid shortening of the connector with the microstrip line and is widely practiced for wideband impedance matching [106]. The dimensions of this antenna are $23.0 \times 30.0 \times 0.254\ \text{mm}^3$. The rest of the configuration is same as in **Figure 3.4**. The prototype of the antenna is shown in **Figure 3.12(b)**.



(a)



(b)

Figure 3.12. Edge-fed microstrip patch array antenna with curved substrate (a) Geometry (b) Prototype.

3.4.2 Discussion and Results of Curved Substrate

The results presented in this section are simulated and experimental verification is not possible due to the hardware limitation as accurate and uniform bending of the Rogers RT/duroid 5880 substrate would require suitable material designed specifically for the antenna for different degrees of bending to conform to. The purpose of these simulations is to show how bending the substrate, knowingly or unknowingly, effects on antenna's results and whether care should be practiced during fabrication of the antenna. Rogers RT/duroid 5880 substrate usually does not deteriorate uniformly during cutting the board, fabrication, placing connector, using cables or even hard handling of the substrate however the impact of changing the planar characteristic, even uniformly, can change the results as discussed in the upcoming sections. Simulating non-uniform bending of the substrate is not possible due to a large number of combinations of the way the substrate can be bent, in concave and convex directions, from different corners. The results of bending the substrate may vary for other antenna designs depending on the antenna structures and configurations, number of elements and their array factors.

3.4.2.1 Concave Bending

The effects of concave bending of the substrate on simulated $|S_{11}|$ are presented in **Figure 3.13**. With reference to 0° , i.e., flat substrate, a -5° bend tunes down the frequency by 120 MHz. A further concave bending up to -15° tunes down the frequency by 40 MHz after which it tunes up by 140 MHz as the substrate is bent up to -30° . Although a -5° bend is visible to the naked eye on a flat surface and while these resonance shifts are minute and the impedance bandwidth remains unaffected with concave bending, it is important to note the tolerance of Rogers RT/duroid 5880 substrate for fabrication and hand-

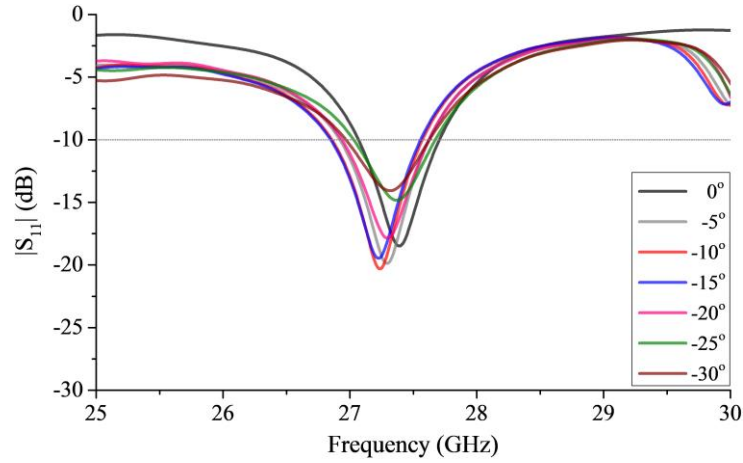


Figure 3.13. Simulated $|S_{11}|$ with concave bending.

ling with the connector during measurement for future antennas as the concave bending of the flexible substrate may result in undesired frequency shifts.

Figure 3.14 shows the simulated realized gain plot of the array with different degrees of concavity. With reference to the gain for flat surface, the gain does not vary drastically with each degree of concave bending and the antenna's gain profile, between 27 GHz and 28 GHz, drops approximately at an average of 0.02 dBi/degree for bending from 0° to -30°.

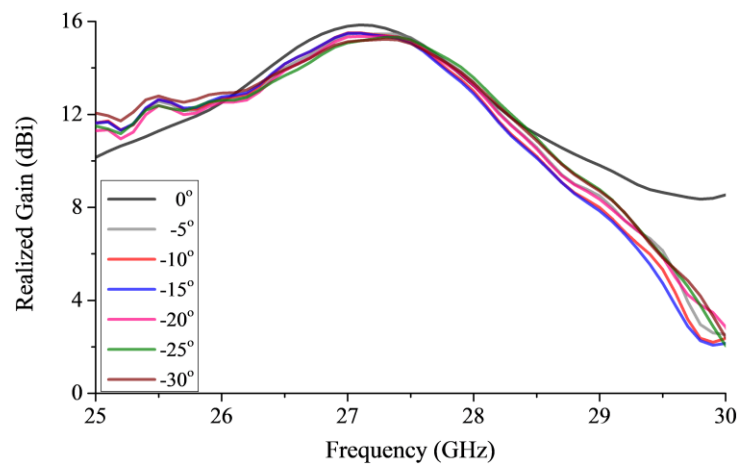


Figure 3.14. Simulated realized gain with concave bending.

The simulated 2-D polar plots on the curved substrate are shown in **Figure 3.15**. The increase in bending in concave direction increases the sidelobe level in the xz-plane, shown in **Figure 3.15(a)**, which leads to a wider HPBW but reduced gain. **Figure 3.15(b)** shows the pattern for the yz-plane of the antenna. It is observed that the increase in the concave angle does not affect the overall gain pattern but has small variations in the gain.

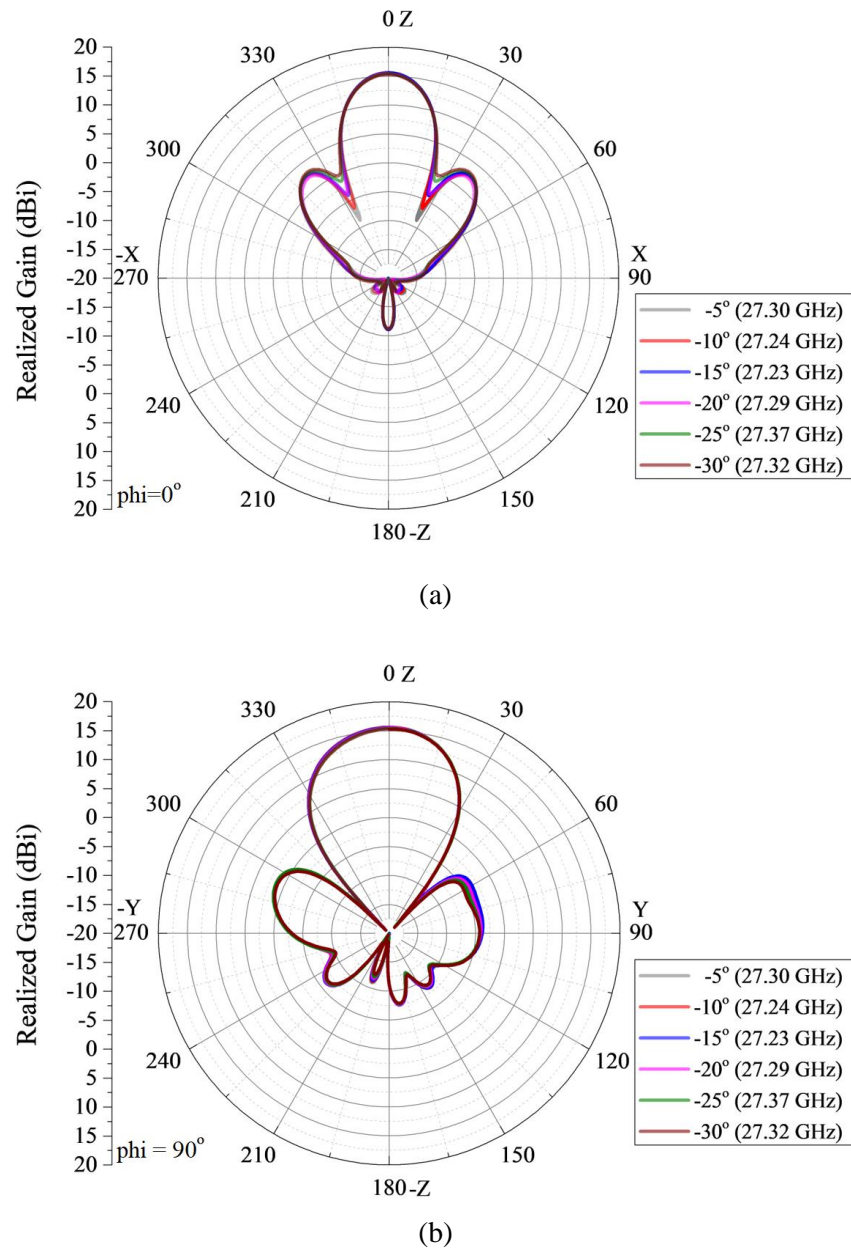


Figure 3.15. Simulated polar plots with concave bending (a) xz-plane (b) yz-plane.

3.4.2.2 Convex Bending

The antenna shown in **Figure 3.12** is bent in convex shape to observe tolerance. The simulated $|S_{11}|$ response, presented in **Figure 3.16**, shows that a bend in the substrate, as little as 1° , tunes the frequency higher than the reference 27.40 GHz by approximately 520 MHz. At $+3^\circ$ bend, another resonance emerges at 25.23 GHz and tunes upwards as the convexity increases. This is because of the reduced separation between patches resulting in mutual coupling, which effects the reflection coefficients, gain and terminal impedances [58], [107], as the usual, centre-to-centre, distance between the elements in the array factor is for planar geometries however in this case, the central and farthest elements are separated at an angular distance which forms an arc. Similar to concave bending, the antenna impedance matching degrades with increased curve angle, but little changes are observed in the bandwidth. Apart from this tolerance, the antenna in convex shape may also be considered for its reconfigurability feature, with the ability to tune frequency upwards for 0° to $+10^\circ$ bend between 27.40 GHz and 29.21 GHz, without the additional circuitry and exploiting the substrate's flexible properties.

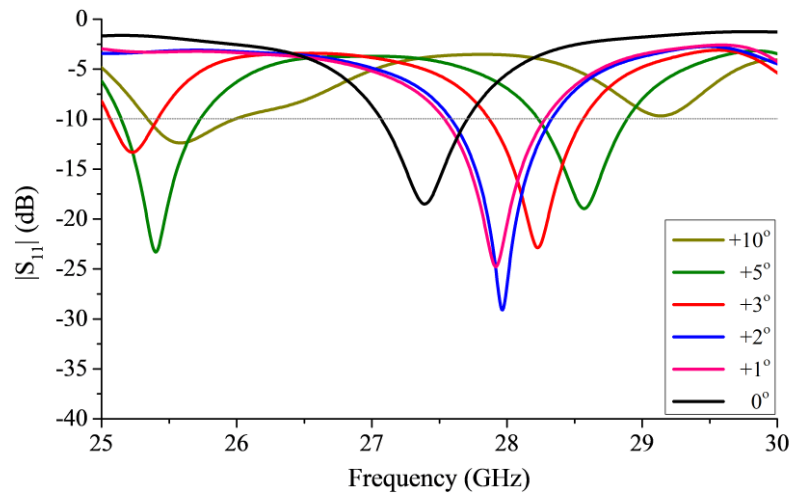


Figure 3.16. Simulated $|S_{11}|$ variation with different degrees of convexity.

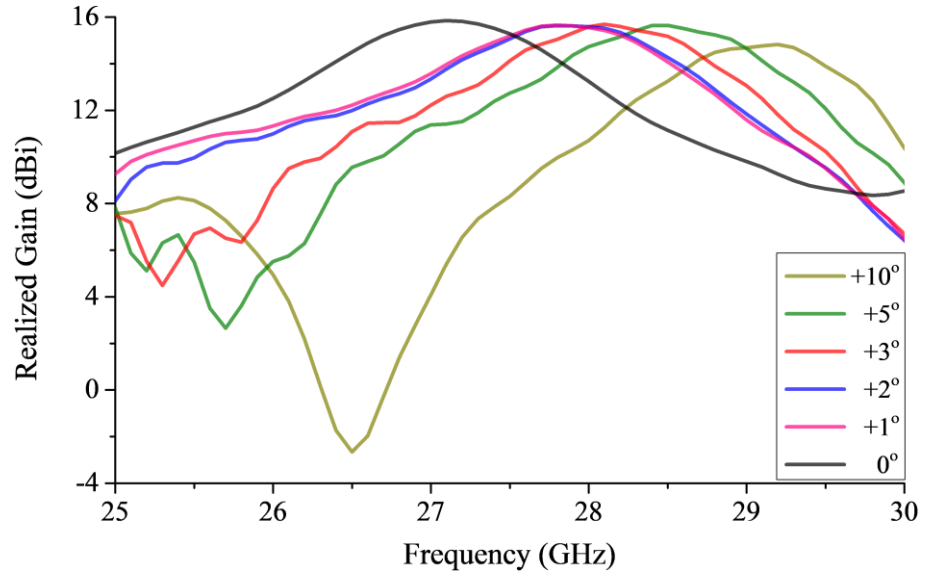
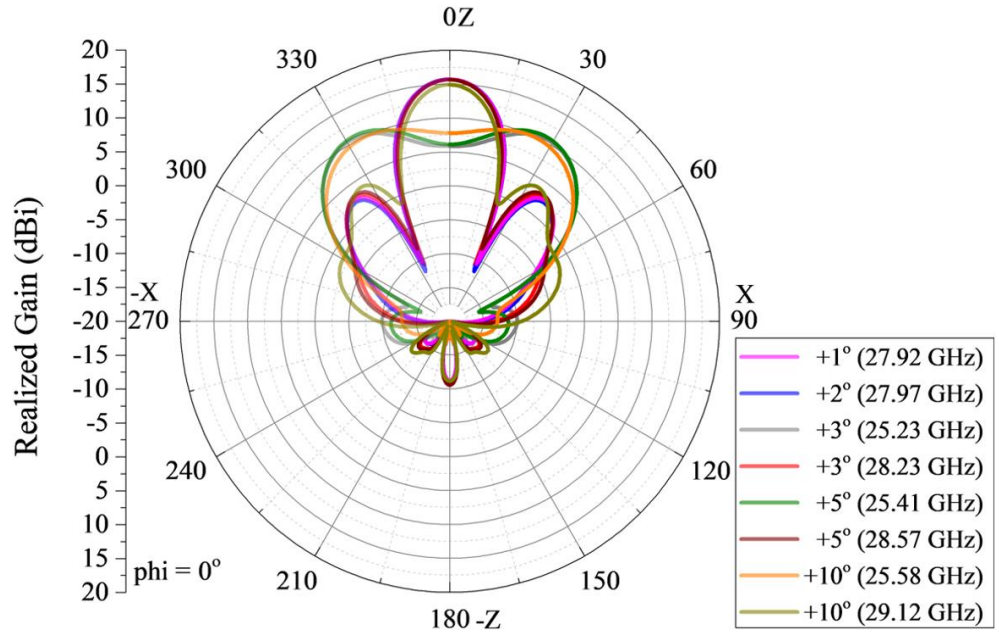


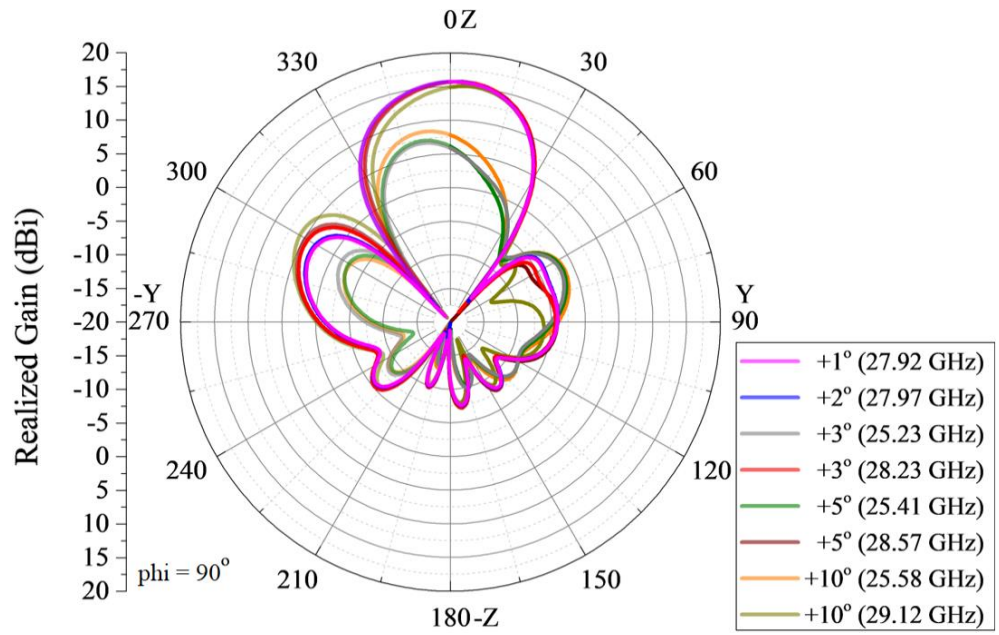
Figure 3.17. Simulated realized gain variation with different degrees of convexity.

The gain profile of convex bending is presented in **Figure 3.17**. Although the peak gain remains consistent as the convexity increases, the corresponding frequency tunes upwards.

The simulated polar plots for variation of degree of convexity are shown in **Figure 3.18**. The xz -plane in **Figure 3.18(a)** shows the dual beam symmetrical distribution of radiation along the end-fire direction at 3° convex bend for 25.23 GHz, which is the additional resonance. Similar distributions are observed for the subsequent additional resonances up to 10° . In the yz -plane, presented in **Figure 3.18(b)**, the SLL can be seen to increase by 1 dB per 10° convex bend. At 3° bend and above, the plots of additional resonances are plotted which are found to have low gain compared to the main resonance. As for the mechanical reconfigurability feature, the antenna has optimum gain in the broadside direction for each shift in frequency with minute degradation of SLL and no change in HPBW.



(a)



(b)

Figure 3.18. Simulated polar plots with convex bending (a) xz-plane (b) yz-plane.

3.5 Summary

In this chapter, a 4×2 element microstrip patch antenna array of dimension $19 \times 30 \times 0.25 \text{ mm}^3$ for 28 GHz communications, providing a 16.10 dBi measured broad-side gain, is described. Initially, a single microstrip patch antenna with inset feed, symmetric to the width of the antenna, is analysed and the performance is observed. The microstrip antenna is later incorporated into rear-fed and edge-fed arrangements where the inset feed is used. The simulated and measurement results are found to be in good agreement.

In order to observe tolerance of Rogers RT/duroid 5880, the effects of curving the substrate in concave and convex directions are investigated on the array with edge feed arrangement. Rogers RT/duroid 5880 is a flexible substrate and, although widely used for planar antennas for mm-waves, the handling during fabrication and measurements may deform the substrate which might not be visible to naked eye. A summary of substrate's tolerance and performance of the antenna with bending angles is presented in **Table 3.2**. Concave curving of the substrate was found to have minimal effect whereas performance is shown to be heavily dependent on convex curve angle.

The results from this study show that care is to be observed in future antenna fabrications while handling the substrate, during installation of connector, cutting the substrate, scrapping metal, drilling holes or just hard hand grip. Although the effects might be different depending on the elements and configuration of antenna in an array, but results may change if caution is not exercised for future fabrications with unintentional substrate bending and deformation.

Bending (°)	Bandwidth (GHz)	Peak Realized Gain (dBi)	HPBW (°) xz/yz – planes	SLL (dB) xz/yz – planes
-30	26.96 – 27.63	15.23 (27.32 GHz)	22.60 / 36.60	-12.40 / -13.80
-20	26.94 – 27.62	15.35 (27.29 GHz)	22.50 / 36.50	-13.30 / -14.40
-10	26.86 – 27.57	15.51 (27.24 GHz)	22.10 / 36.40	-13.20 / -14.60
-5	26.92 – 27.63	15.60 (27.30 GHz)	22.10 / 36.10	-13.40 / -14.70
0	27.03 – 27.76	15.84 (27.40 GHz)	21.50 / 35.90	-12.10 / -13.60
3	25.06 – 25.42 27.86 – 28.56	15.68 (28.23 GHz)	21.0 / 35.30	-12.60 / -11.50
5	25.15 – 25.73 28.23 – 28.90	15.64 (28.57 GHz)	20.60 / 34.60	-12.30 / -10.90
10	25.34 – 25.97 29.07 – 29.21	14.82 (29.12 GHz)	20.0 / 33.00	-11.40 / -9.30

Table 3.2. Frequency reconfiguration, realized gain, HPBW and sidelobe level with mechanical bending of Rogers RT/duroid 5880 substrate.

Chapter 4

Dual-Band Millimeter-Wave Grid Array Antenna

4.1 Introduction

First proposed in 1964 by J. D. Kraus, the grid array antenna (GAA) was formed using multiple rectangular wire loops [108], [109]. Kraus's initial proposal was a traveling wave antenna that was a function of frequency and scanned in backward angle-fire direction. Each loop consists of long sides and short sides, with the former acting as transmission lines and the latter behaving as both transmission line and radiating element. The design was later transformed to non-traveling wave printed microstrip technology, with high gain and broadside beam, by Conti et. al in 1981 [110]. **Figure 4.1** presents a basic arrangement of microstrip GAA with 5 rectangular loops on an air substrate with metallic ground plane cladding. Depending on the GAA's structural configuration, the antenna can be fed from the center or the edge using a coaxial cable. The electrical lengths of the sides of the GAA dictate the ability of the structure to be used as a resonant or non-resonant antenna [111]. For the structure shown in **Figure 4.1** to be resonant, the long sides are approximately one guided wavelength long and the short sides are approximately half the length of the long side. In this way, the currents in the long sides are kept out of phase, therefore cancelling in broadside, while currents in the short sides of the loops are in phase which contribute to radiation.

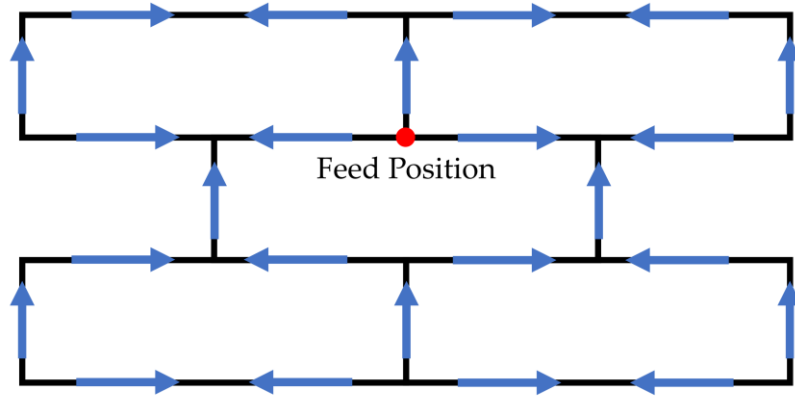


Figure 4.1. A 5-loop grid array antenna arrangement showing current distribution in long sides and short sides.

Although introduced as a traveling-wave antenna in 1964, the GAA has not found much popularity in that domain. Similar to the non-resonant structure, the edge-fed traveling-wave GAA also has constructively and destructively interfering currents in the short and long side of the loops, respectively. In 1974, Tiuri et al. expanded on Kraus's idea and proposed the lengths of the short side loops may have the dimensions of 0.4 times the wavelength whereas the long side lengths should be equal to a wavelength in the dielectric [112]. A squint in the beam is observed in the GAA acting as a traveling-wave antenna when it is fed from the edge and the other end is either terminated with [112] or without load [108]. This enables the GAA to develop scanning characteristics with change in frequency without any additional beamforming or phase shifting network or circuitry but it does not offer beam control in terms of the direction or fixed frequency beam scanning [111], [113].

The GAA has not been extensively studied for mainstream applications since its invention. The conventional wire GAA's input impedance was greater than $50\ \Omega$ and had narrow impedance bandwidth [114], [115]. To overcome these challenges Nakano et al.

furthered the analysis and design on lower microwave frequencies to enhance the GAA's performance by deploying Method of Moment and interpolation techniques to reduce computational time [115]. Their research group also proposed resonant center-fed GAA [116], miniaturized the GAA using meandering the loop approach [117], modified the microstrip GAA structure for circularly polarized antenna [118], a frequency-scanning GAA with Rhombic loops [119], off-center-fed GAA for dual band applications at 2.27 GHz and 17.70 GHz [120] and several others [121], [122]. There are many other variants or recognizable forms of the GAA such as chain antenna [112], mesh patch antenna [123], brick wall antenna [124], and the honeycomb antenna [125] and their performance may vary with change in substrates, their thickness and frequency with the close proximity of placement of elements in the mm-wave region due to shorter wavelength.

The first implementation in the mm-wave region was conducted by Zhang et al. when they designed a basic microstrip GAA on LTCC at 60 GHz for antenna-in-package technology [126]. Since then several GAA designs at mm-wave have been introduced such as multiport sub-grid arrays [113], in which different GAAs at 61.5 GHz are meshed together to improve the unsynchronized current resulting in broadside beam, multiport MIMO GAA at 24.0 GHz for radar and sensing applications [127]. Few works in the upper 26 GHz 5G and beyond applications are found in the literature which include wide-band GAA from 27.54 GHz to 32.33 GHz with peak gain of 12.66 dBi [128], 14 rectangular loop 28 GHz GAA with 11.32 dBi gain [129], dual beam wide band GAA with circular patches for 5G applications with peak gain of 11.34 dBi at 32.5 GHz [130] and its 4-element MIMO array with peak gain of 11.57 dBi at 29 GHz [131] and a miniaturized GAA replacing the long sides with bent lines at 28 GHz with compact size on a 1.50 mm thick substrate to obtain wideband performance [132].

In this chapter, 20 rectangular loops are arranged in a quasi-rhombic shaped symmetric microstrip GAA configuration for dual band mm-wave applications. A comparison with equal sized microstrip patch array is also presented to analyse the performance. The GAA operates in the upper 26 GHz mm-wave band [133] and has two frequency bands in close proximity.

4.2 Quasi-Rhombic Grid Array Antenna Geometry

The top view of the geometry of proposed grid array antenna is illustrated in **Figure 4.2**. The grid structure of the antenna is printed using copper cladding on a flexible Rogers RT/duroid 5880 substrate with loss tangent of 0.0009, thickness of 0.254 mm, relative permittivity of 2.2. The ground plane also has a copper cladding of 0.017 mm. Similar to the other microstrip grid array antennas proposed in the literature, the proposed antenna's unit-cell, referred to as brick, is formed using two types of microstrip lines i.e., short and long sides [134] and 20 such brick-cells are arranged in a quasi-rhombic pattern which, as a result of shape optimisation investigation, gives the structure the ability to resonate with in-phase addition of currents in the vertical elements. Each brick-cell has horizontal spacing of W_t and vertical spacing of L_t . W_t is kept wider than L_t to mitigate the undesired cross-polarized radiation [113]. The long side of each brick cell, W_b , acts as a transmission line and the short side, L_b , operates as radiating element as well as the transmission line. The lengths W_b and L_b are approximately equal to $1.08\lambda_g$ and $0.54\lambda_g$, respectively, which makes the currents out of phase for W_b and in-phase for L_b , theoretically [135]. The antenna is fed between the first and the second row from the top at an optimized point 0.20 mm below the lower long side, on the y-axis. The geometric details of the parameters

are tabulated in **Table 4.1**.

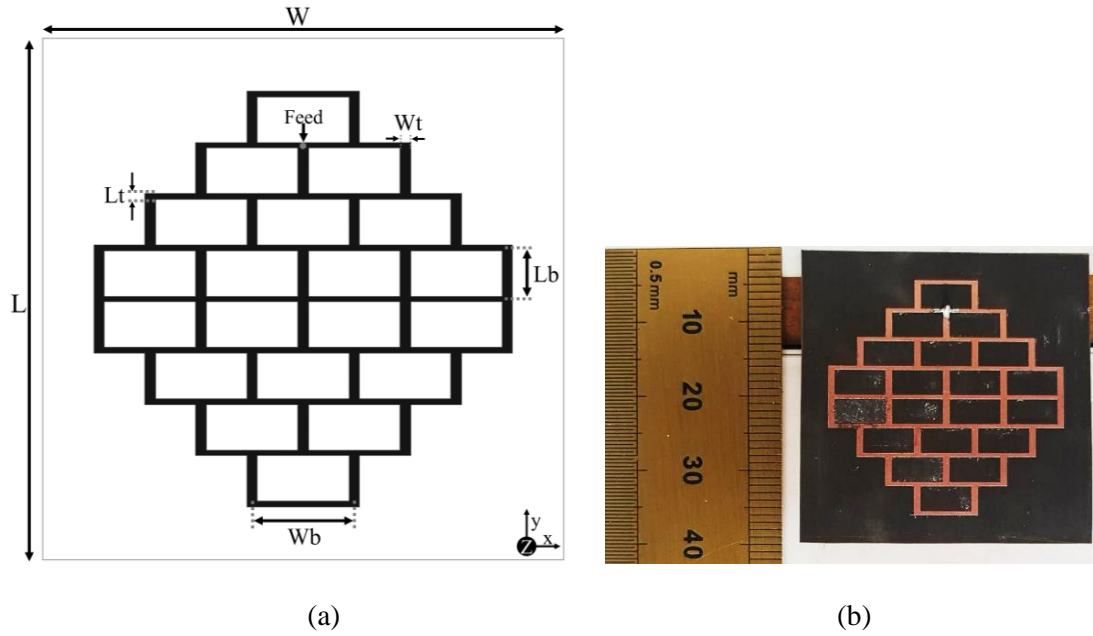


Figure 4.2. Rear-fed grid array antenna (a) Geometry (b) Prototype.

Parameter	Symbol	Dimension (mm)
Width of substrate	W	40.0
Length of substrate	L	40.0
Width of horizontal line	L_t	0.42
Width of vertical line	W_t	0.80
Length of vertical line	L_b	4.35
Length of horizontal line	W_b	8.63

Table 4.1. Design parameters of Grid array antenna.

4.3 Parametric Analysis

4.3.1 Effect of Feed Position

The proposed quasi-rhombic grid array antenna is geometrically symmetric in both xz and yz -planes. The diameter of the probe pin of the connector is 0.64 mm, therefore, for realistic simulations, the antenna can be fed on the microstrip line with wider width i.e., L_t . The possible feed position locations, illustrated in **Figure 4.3**, are chosen at the edge of each length L_b in the upper half of the yz -plane. *Position 4* is the optimized feed position described in Section 4.2. Taking advantage of the properties of symmetric planes, the results with mirrored feed positions in the lower half will have the same $|S_{11}|$ and mirrored radiation pattern in the yz -plane.

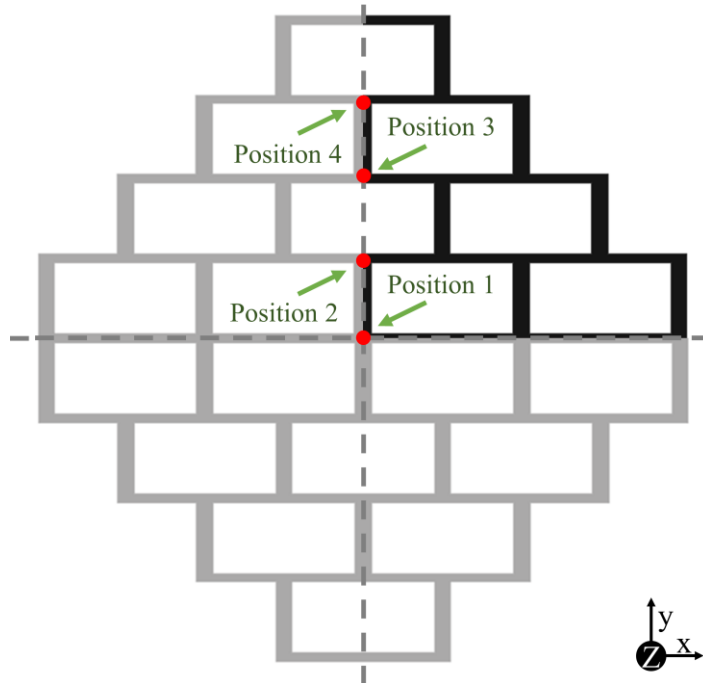


Figure 4.3. Feed position locations along the upper symmetric half of the yz -axis.

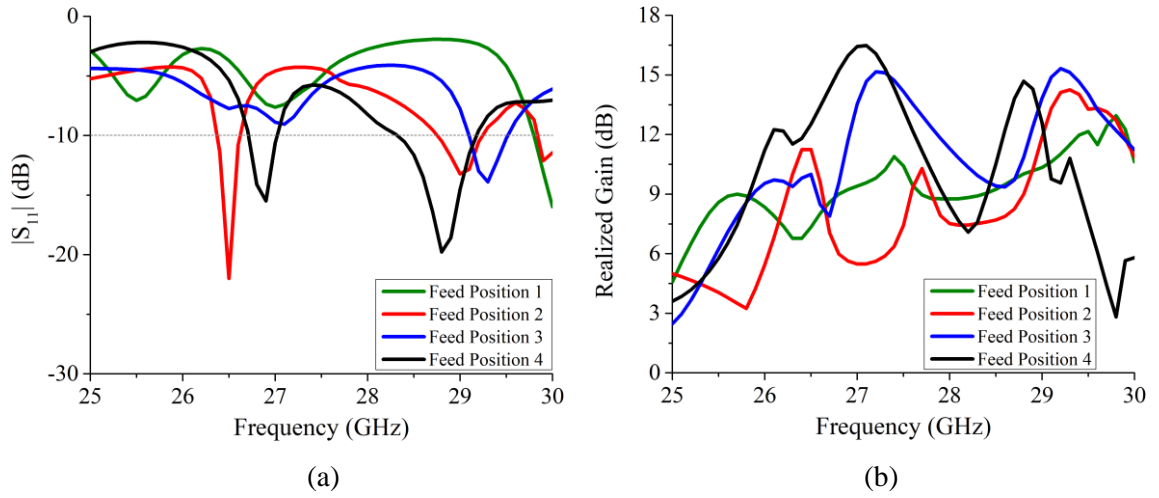


Figure 4.4. Feed positions analysis (a) $|S_{11}|$ (b) Realized gain.

Figure 4.4(a) shows the simulated $|S_{11}|$ for the feed positions 1 through 4 simulated using the parameters presented in **Table 4.1**. When fed through the centre of the antenna, i.e., *position 1*, impedance mismatching is observed until a resonance appears at 29.80 GHz. This mismatching is reflected with low realized gain in **Figure 4.4(b)** which is expected because of the currents travelling in opposite direction, in the yz -plane, follow phase progression in either direction leading to dual-beam radiation. At *position 2*, the antenna has two narrow resonances with $|S_{11}| \leq -10$ dB between 26.40 GHz to 26.60 GHz and 28.80 GHz to 29.92 GHz, with currents adding up in phase largely in one direction than the other resulting in having peak gain of 11.24 dBi and 14.12 dBi in these frequency bands. Although the GAA, fed at *position 3* moving further away from the center, has better gain at the first resonance around 27.0 GHz than *position 2*, the $|S_{11}| > -10$ dB for the first resonance is not matched. At feed *position 4*, the antenna has wider bandwidth in both frequency bands than the other feed positions. For the first frequency band, the antenna's peak gain is significantly better than the other feed positions and in the second band, although not better than the GAA when fed at *position 3*, the gain is comparable.

4.3.2 Effects of Varying Design Parameters

Figure 4.5 shows the analysis of the parameters associated with the brick cell, individually, by varying one parameter and keeping the others constant. **Figure 4.5(a)** shows the effect of variation of the short side length, L_b , on the $|S_{11}|$. The increase in L_b by 0.20 mm between 4.15 mm and 4.55 mm tunes down the first frequency band by approximately 800 MHz, due to increase in the wavelength which is inversely proportional to frequency, with no considerable change in the bandwidth. The feed position is optimized for $L_b = 4.35$ mm therefore the same feed position, when applied on

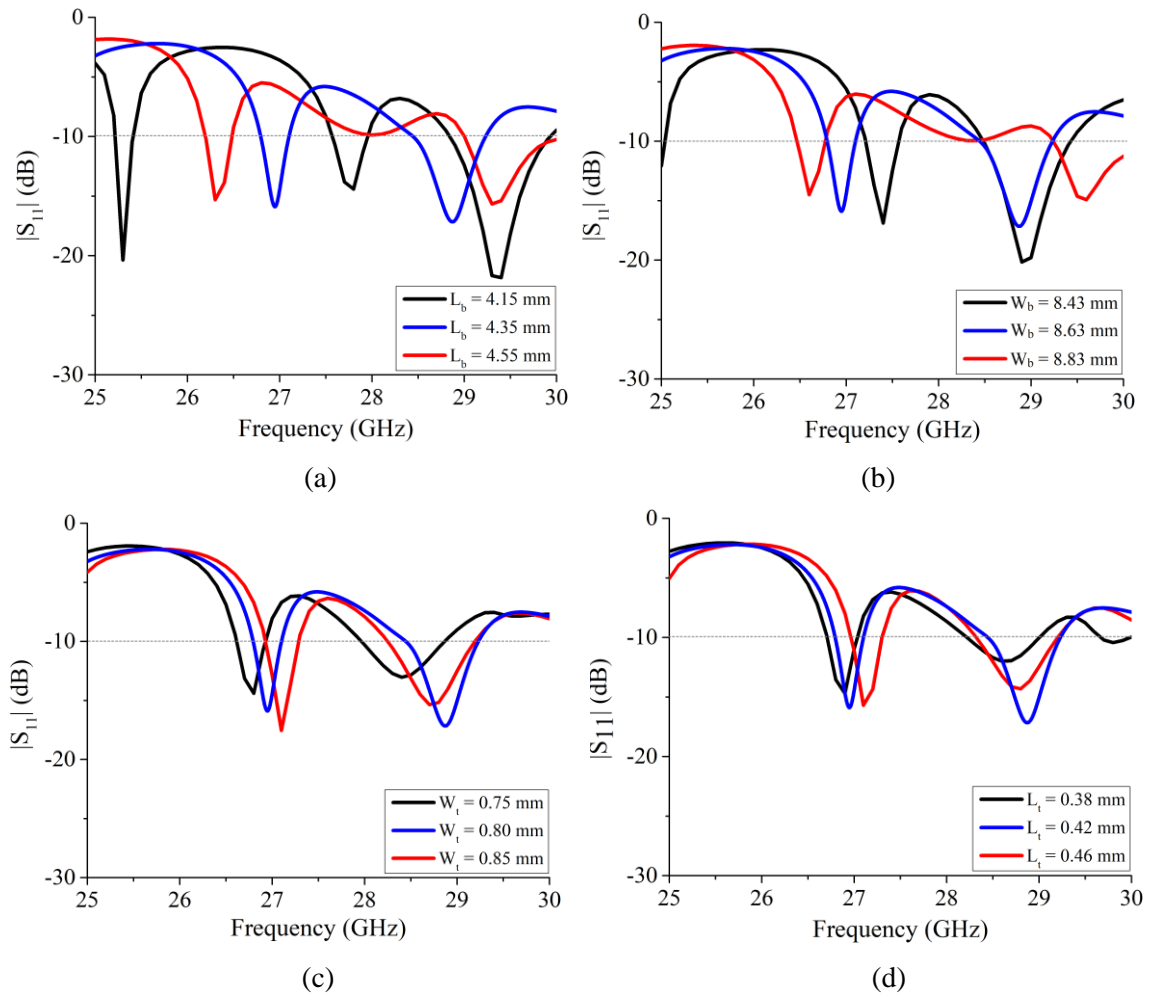


Figure 4.5. Parametric analysis varying (a) L_b (b) W_b (c) W_t (d) L_t .

a different length of L_b , tunes the frequency upwards where impedance matching is observed to be better with $L_b = 4.15$ mm than 4.55 mm variation with no significant change in bandwidth. As mentioned in the previous section, the antenna and its wavelengths are calculated and designed for the first frequency band i.e., 27 GHz, however the effects of variation in parameters are observed for both frequency bands between 25 GHz and 30 GHz to achieve best optimised performance for both bands. **Figure 4.5(b)** shows the effect of varying the long side length, W_b , on the $|S_{11}|$ of the GAA. The frequency, in the first frequency band, tunes down by approximately 750 MHz, as increase in wavelength reduces the resonant frequency, when W_b is increased by 0.20 mm from 8.43 mm to 8.83 mm. For the second band, the bandwidth reduces by 200 MHz when W_b is increased from 8.43 mm to 8.63 mm, but it tunes upwards by approximately 500 MHz when W_b is 8.83 mm. The effect of varying the short side width, W_t , is presented in **Figure 4.5(c)**. The impedance matching slightly improves and the frequency tunes upwards as W_t is increased by 0.05 mm between 0.75 mm and 0.85 mm ($\sim 50 \Omega$ to 46Ω), but the impedance matching is better in the second band when W_t is 0.80 mm ($\sim 48 \Omega$) than the other variations. As mentioned in Section 4.2, the width of the long side, L_t , is kept narrower than W_t . **Figure 4.5(d)** shows the effect of varying L_t by 0.04 mm between 0.38 mm and 0.46 mm. Minute upward tuning on the frequency by approximately 40 MHz, with no effect on bandwidth, in the first band, is observed with this variation whereas, in the second band, the impedance matching shows improvement when L_t is 0.42 mm ($\sim 71 \Omega$) which is nearly half of that of W_t .

4.4 Results and Discussion

Figure 4.6 shows the $|S_{11}|$ of the quasi-rhombic GAA show in **Figure 4.2(a)**. The proposed GAA is measured using Rohde and Schwarz Vector Network Analyzer (ZVA40). The simulated GAA has $|S_{11}| < -10$ dB from 26.79 GHz to 27.10 GHz and 28.44 GHz to 29.23 GHz with FBW of 3.89%. However, the measured results of the GAA show that the antenna operates from 26.84 GHz to 27.86 GHz and from 28.37 GHz to 28.85 GHz having FBW of 5.41%. This is because simulation of the GAA requires a lot of computational resources because it needs very fine meshing throughout the structure due to its slot-based geometry which comprises of numerous bends and edges that affect the operation of the structure [135]–[137]. The position of feed in GAA, along with solder joint, can also greatly affect the results. A minute displacement in the feed position, while manufacturing the design, can change the results altogether because of the sensitive optimization of the geometry. The simulated radiation efficiency of the antenna, presented in **Figure 4.7**, is found to be above 80% in the first and 90% in the second frequency band.

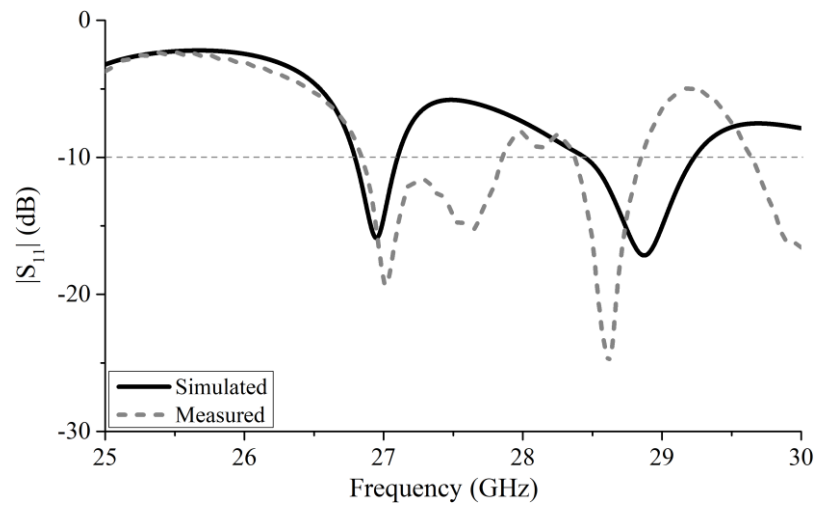


Figure 4.6. Simulated and measured $|S_{11}|$ of the quasi-rhombic grid array antenna.

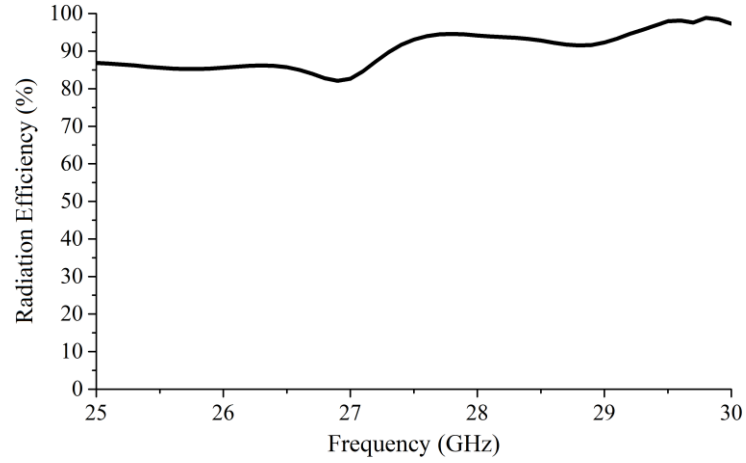


Figure 4.7. Simulated radiation efficiency of the grid array antenna.

The surface current distribution at 27.0 GHz is presented in **Figure 4.8(a)**. The current distribution can be seen to be strong and in-phase in the short sides of the GAA. In the wide long sides, the currents appear to be out of phase thereby destructively interfering and acting as transmission lines as discussed in the theory of GAA in Section 4.1. **Figure 4.8(b)** shows the current distribution at 29.10 GHz. From the centre of the structure, the currents on the vertical short sides of the brick-cell of the GAA are observed to

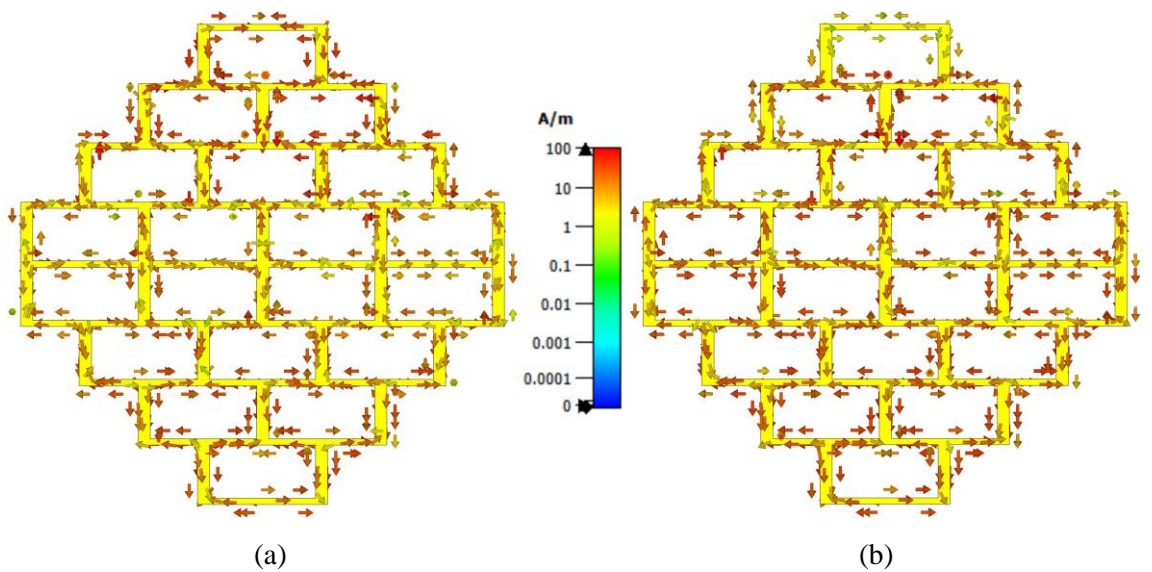


Figure 4.8. Surface current distribution at phase = 0° (a) 27.0 GHz (b) 29.10 GHz.

flow in opposition direction because the brick-cell is designed for 27.0 GHz and the currents at 29.10 GHz do not add-up in phase.

The simulated and measured 2-D polar plot, in the xz-plane, at two frequencies, i.e., 27.10 GHz and 28.70 GHz is presented in **Figure 4.9(a)**. A directive radiation pattern is observed with peak gain of 16.5 dBi and HPBW of 25° at 27.10 GHz. The gain at 28.70 GHz reduces as a result of the beam-split, shown in the yz-plane shown in **Figure 4.9(b)**. The tilt in the beam from broadside observed at 27.10 GHz is because of the feed placement away from the centre of the GAA. The simulated and measured results have good agreement.

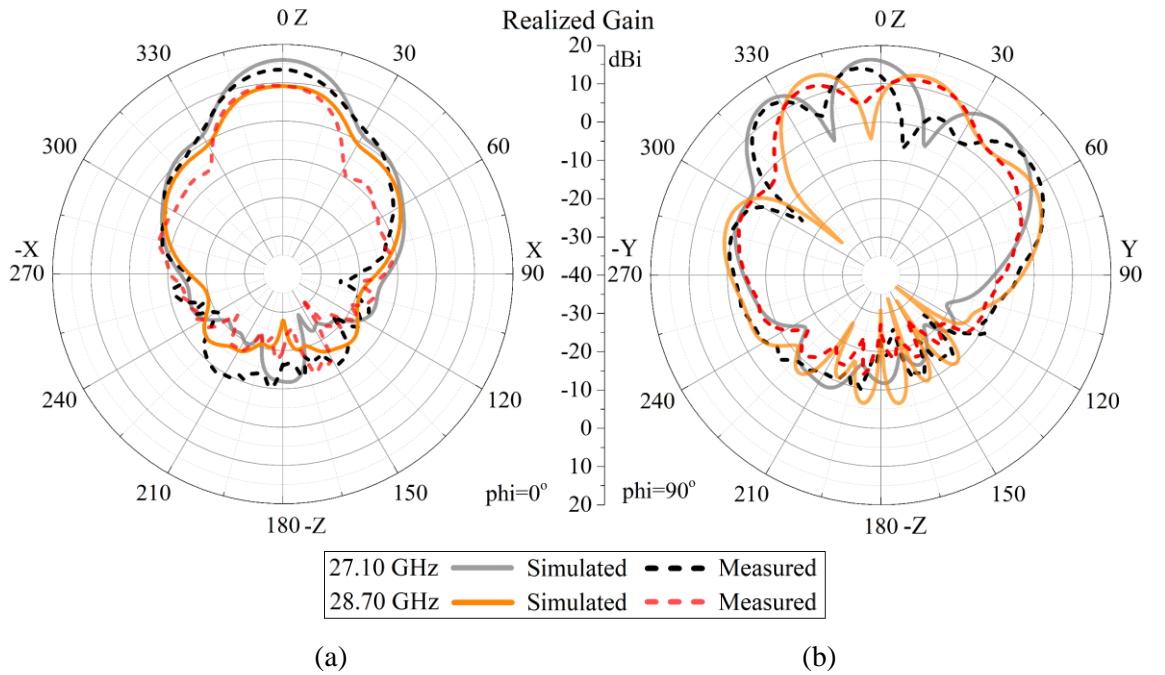


Figure 4.9. Simulated and measured polar plots of grid array antenna (a) xz-plane (b) yz-plane.

4.5 Comparison with equidimensional Microstrip

Patch Array Antenna

A performance comparison between the GAA and microstrip patch array antenna is presented. The geometry, shown in **Figure 4.10**, is an extension of the rear-fed 4×2 microstrip patch array antenna, presented in Section 3.3, with 4×4 array structure in order to compare with the quasi-rhombic GAA, of the same size, presented in Section 4.2. Similar to the earlier work, the microstrip array is designed on Rogers RT/duroid 5880 substrate having thickness of 0.25 mm. The array consists of 16 radiating elements with 0.75λ spacing between the patches in the same row. The patches are connected to $100\ \Omega$ lines and then to a matching network using quarter-wave transformers. The rows of the array

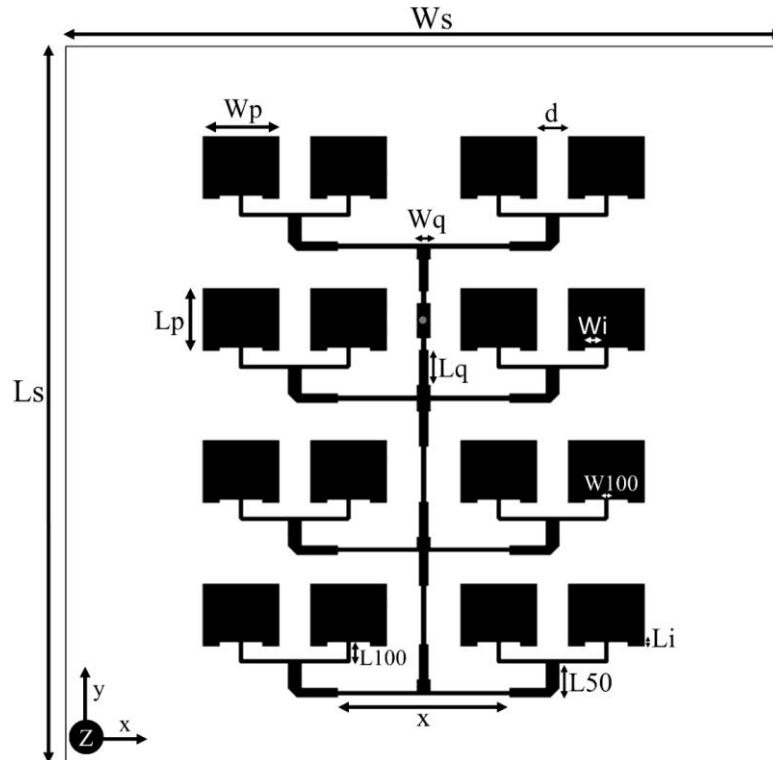


Figure 4.10. Geometry of 4×4 rear-fed microstrip patch array antenna.

Parameter	Dimension (mm)	Parameter	Dimension (mm)
W_s	40.0	L_s	40.0
W_p	4.48	L_p	3.55
W_i	1.10	L_i	0.20
W_q	0.48	L_q	1.99
W_f	0.80	L_f	2.30
W_{100}	0.25	L_{100}	1.11
d	1.52	x	8.10

Table 4.2. Design parameters of 4×4 microstrip patch array antenna

are connected through a 100 Ω one wavelength network where each network consists of two quarter-wave transformers and two 50 Ω lines. An additional 50 Ω pad is placed between the top two rows to drill a 0.5 mm hole to excite the array. **Table 4.2** presents the detailed parameters of the antenna.

Figure 4.11(a) shows the $|S_{11}|$ of the 4×4 microstrip patch array antenna. In the comparison with the dual band GAA, the patch array has one frequency band having $|S_{11}| < -10$ dB from 27.42 GHz to 28.08 GHz with 2.38% fractional bandwidth, approximately 1.5 percentage points less than the former. The radiation efficiency of the patch array, presented in **Figure 4.11(b)**, is 90% in the operating range which is approximately 7 percentage points more than the efficiency of the first frequency range of the GAA and comparable with second frequency band. **Figure 4.11(c)** and **Figure 4.11(d)** present the 2-D radiation patterns of the patch array antenna, at 27.80 GHz, in the xz-plane and yz-plane, respectively. The microstrip array has higher peak gain of 18.41 dBi and better sidelobe level than the GAA but the latter's HPBW in both planes is better than the microstrip patch array.

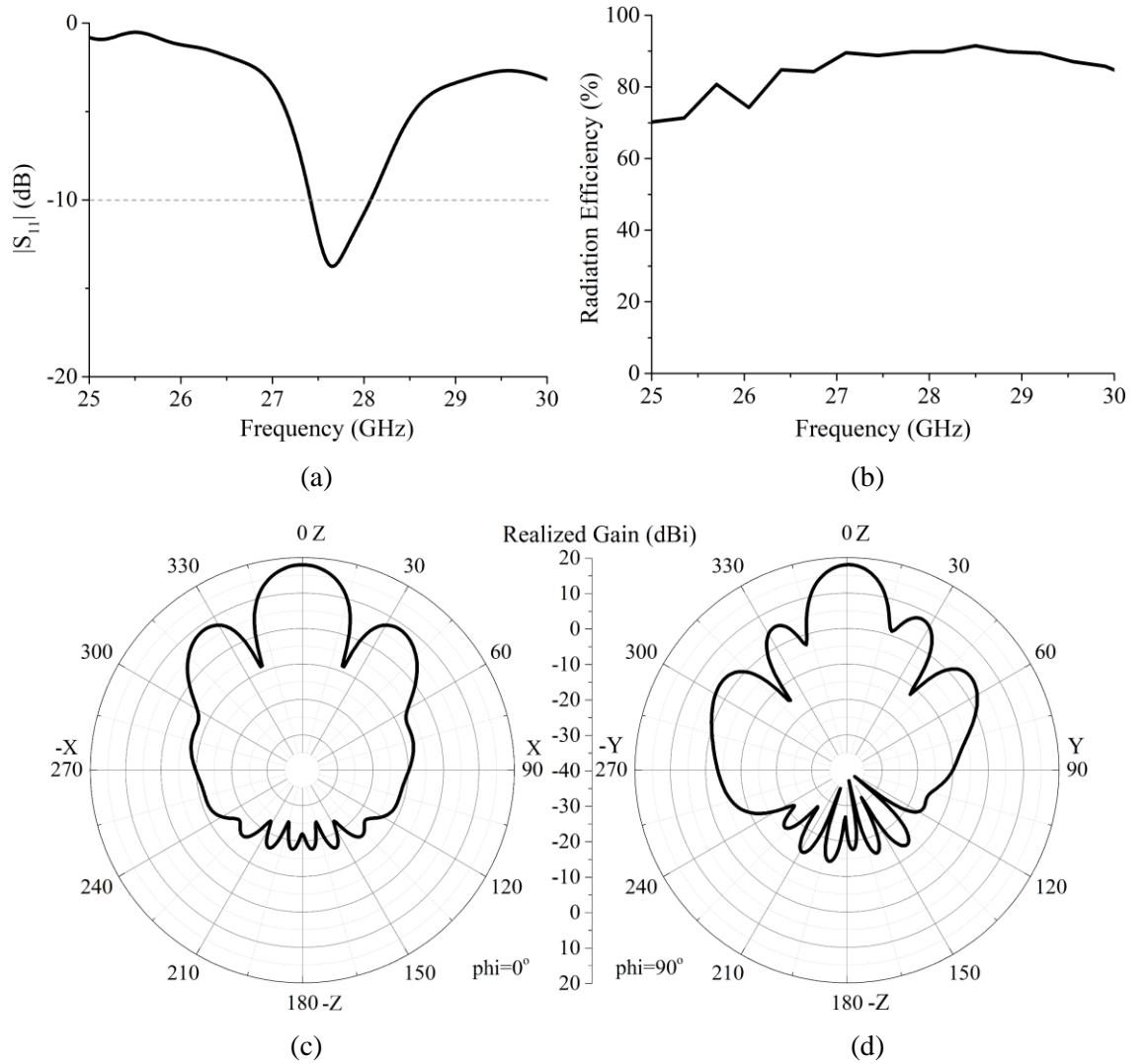


Figure 4.11. 4×4 element microstrip patch array antenna showing simulated (a) $|S_{11}|$ (b) Radiation Efficiency (c) polar plot in xz-plane (d) polar plot in yz-plane.

4.6 Summary

A 40×40 mm² quasi-rhombic, meandered line loop unit-cell, grid array antenna is presented in this chapter. The antenna has dual-band operating range in the upper 26 GHz range. The first frequency range has broadside radiation and dual beam radiation is observed in the second band which provides radiation diversity in tunnels, cellars, caverns

	Grid Array		Patch Array
Dimensions (mm ²)	40×40		40×40
S ₁₁ < -10 dB (GHz)	Simulated	Measured	Simulated
	26.79 – 27.10 28.44 – 29.23 (3.90%)	26.84 – 27.86 28.37 – 28.85 (5.41%)	27.42 – 28.08 (2.38%)
Peak Realized Gain (dBi)	16.5		18.41
HPBW (xz / yz -plane)	25° / 17.1°		19.4° / 16.5°
Radiation Efficiency	> 83%		> 90%

Table 4.3. Performance comparison between proposed GAA and MPA.

and other narrow corridors. The proposed grid array antenna is also compared with a 4×4 microstrip array antenna of the same dimensions. The grid array antenna has 1.5 percentage points more fractional bandwidth than the microstrip array's 2.38%, for the same footprint, having the capacity to accommodate a greater number of 5G and mm-wave devices. Both arrays have very high gains but the microstrip array's gain is about 1.90 dBi higher than the grid array with the grid array's standout feature is having both single and dual beam radiation characteristics compared to patch array antenna's single beam radiation. The proposed antenna boasts a number of advantages such as its wide fractional bandwidth, wide beamwidth and simple and compact geometry. This performance comparison is tabulated in **Table 4.3**.

The next chapter deals with another iteration of planar meandered line geometry with multiband mm-wave performance based on the theory of wire Bruce array antennas.

Chapter 5

Tri-Band Millimeter-Wave Bruce Array Antenna

5.1 Conventional Bruce Array Antenna

In 1931, Edmond Bruce patented the idea of Bruce array antenna (BAA) in which a long wire antenna was bent in equal and periodic meandered intervals [138]. The antenna was designed for radio amateur applications in which bi-directional broadside radiation and high gain is required. **Figure 5.1** shows four variations of a typical BAA fed from the vertical segment of the structure using a twin-line feed mechanism. In the figure, the lengths and directions of the arrows are a representation of the magnitudes and flow of the current, respectively. The horizontal and vertical segments, of the meander line, were both kept equal in size, i.e., approximately $\lambda/4$, for radio ham applications except for the last two inward bent segments which are half the length of the other segments. The currents in the horizontal segments, represented by light grey colour, flow in opposite direction, add destructively and are cancelled in the space consequently do not contribute to any radiation, ideally. These horizontal elements are, therefore, considered as interconnecting segments. The flow of currents, in the vertical segments, being in the same direction, add constructively in phase to give broadside radiation which is why these segments are termed as radiating elements. The half inward bent segments, on either ends of the

structure, have little to no magnitude of current therefore maintaining reasonably low cross-polarized radiation [138].

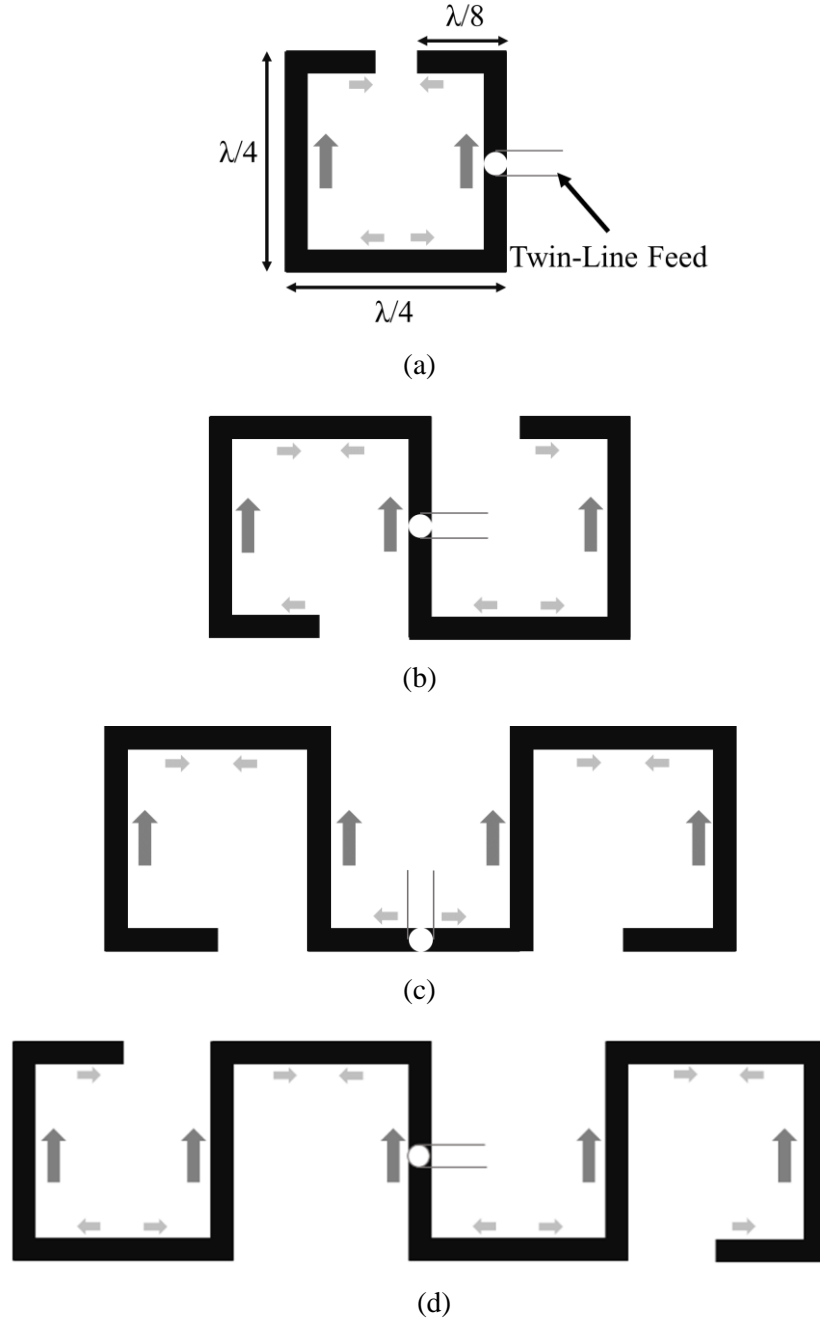


Figure 5.1. Variations of Twin-Line fed wire Bruce array antenna with number of vertical radiating elements (a) 2 (b) 3 (c) 4 (d) 5. (adapted from [139])

As the number of radiating elements are added to the structure, HPBW in E-plane becomes sharper with the increase in peak realized gain and the radiation pattern in the broadside becomes so compressed and narrow that it is shaped as bi-directional fan-beam radiation pattern as shown in **Figure 5.2**. The BAA offers reduced complexity, substantially greater bandwidth than other wire antennas such as the bobtail curtain and half-square antennas and for a relatively low height requirement, it can achieve maximum possible gain in a given area [139]. Suited to a particular installation, the wire BAA can also be fed at points other than the center, the lengths can be varied to tune the resonant frequency and it, usually, does not require a ground system but an extensive ground system can be deployed, under the BAA, to mitigate the losses provided there is adequate space [139].

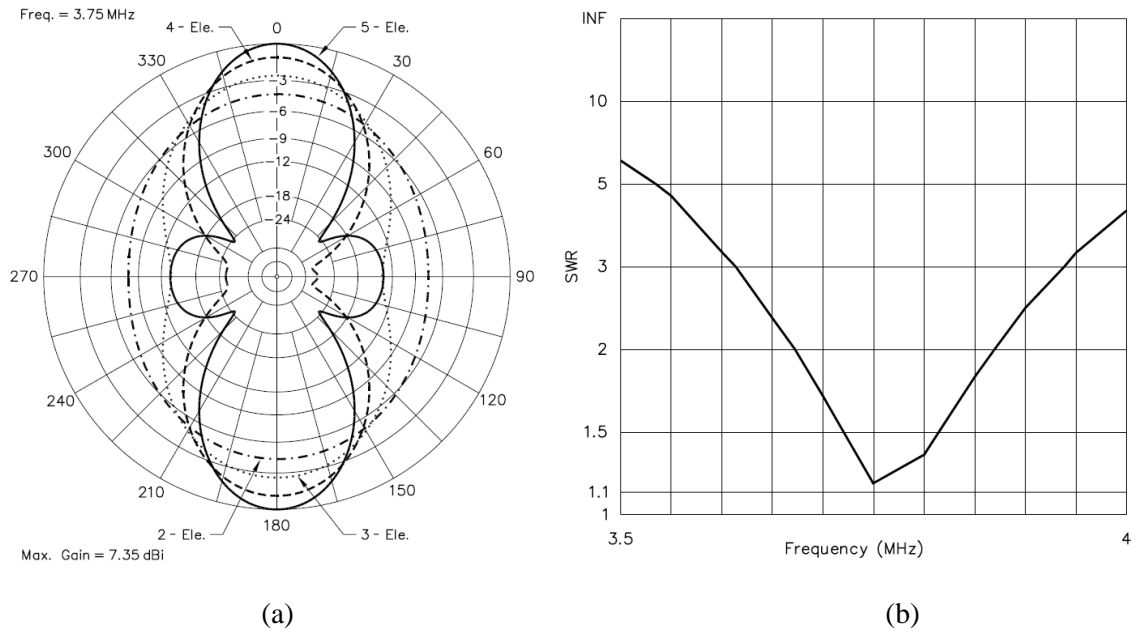


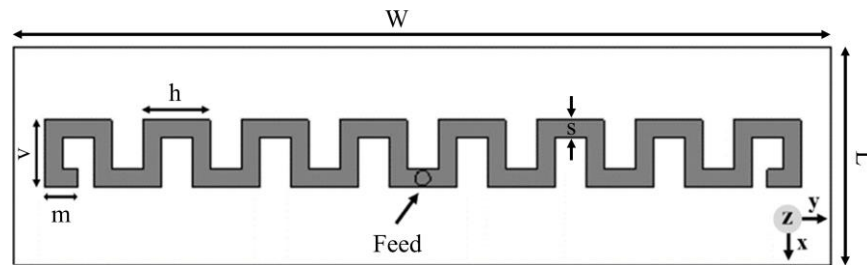
Figure 5.2. 80-meter wire Bruce array antenna (a) free-space E-plane patterns for 2, 3, 4 and 5 vertical elements (b) SWR of a 4 vertical element structure [139].

The BAA has been around for over a century but, in spite of the simplicity of the structure, it has been mainly overlooked by the mainstream researchers to further the concept and propose modifications for utilization in modern day antenna applications. There are only a handful of ideas proposed to make use of the structure which includes Nakano et al.'s concatenation of Bruce and Franklin antennas' performance at 12.50 GHz [140], Chen's twin-line fed slot-type BAA planar equivalent [141].

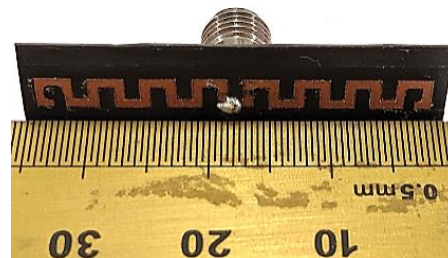
In this chapter, the transition from wire Bruce array antenna to planar technology is discussed. The proposed planar Bruce array antenna operates in three frequency bands with optimization focus on 28.0 GHz band that has a directive fan-beam radiation pattern at broadside whereas the other two operating frequency ranges, i.e., 31.13 GHz to 31.99 GHz and 33.85 GHz to 34.85 GHz, have dual beam radiation patterns for mm-wave dual-beam-single-frequency (DBSF) applications. With the expansion in technology and increasingly complex structures, only a few antennas based on meander line antenna theory are presented in the literature for mm-wave applications [142], [143]. Usually, this bending of the microstrip line technique is used for structure miniaturization which leads to poor radiation efficiency [55], but the proposed antenna has over 90% radiation efficiency. The chapter is divided into four sections. Section 5.1 and 5.2 cover the working principle of conventional wire Bruce array antenna and its planar equivalent. The parametric effects are discussed in Section 5.3 and the impedance bandwidth, realized gain, radiation patterns and other results of the rear-fed planar geometry are discussed in Section 5.4.

5.2 Planar Bruce Array Antenna Geometry

Figure 5.3(a) shows the transformation of wire Bruce array antenna to its planar counterpart with 16 vertical radiating elements. The antenna is designed on the principles of wire Bruce array, with a full ground plane, except for the horizontal and vertical lengths which are increased to $1.46 \times \lambda/4$ because at 28.0 GHz, the gap between vertical elements, v , with $\lambda/4$ becomes so small that unwanted resonances appear as a result of mutual coupling. The antenna is fabricated on Rogers RT/duroid 5880 substrate with thickness of 0.254 mm, relative permittivity of 2.2 and dielectric loss tangent of 0.0009 with 0.017 mm copper cladding on both sides. CST Studio Suite is used to simulate and analyse the results of the antenna [144]. The optimised dimensions of the proposed structure are presented in **Table 5.1**. The antenna is fed from the bottom using 50 Ω Southwest



(a)



(b)

Figure 5.3. (a) Geometry and (b) Prototype of rear-fed planar Bruce array antenna with 16 vertical elements.

Parameter	Symbol	Size (mm)
Width of antenna	W	35.0
Length of antenna	L	9.0
Vertical segment's length	v	3.50
Horizontal segment's length	h	3.50
Inward bent segment's length	m	1.75
Width of trace	s	0.76

Table 5.1. Optimised parameters of planar BAA.

SMK 1014-33SF connector and therefore the width of the horizontal line, s , to which the connector is soldered, is matched to $50\ \Omega$ which will otherwise result in impedance mismatching should a different width, corresponding to different impedance, is chosen. The prototype of the antenna is shown in **Figure 5.3(b)**.

5.3 Parametric Analysis

5.3.1 Variation of Vertical and Horizontal lengths

The proposed antenna is analysed by parametric study of both horizontal and vertical lengths of the antenna to make its performance suitable to work for mm-wave frequencies. In all these parametric variations, m is maintained at half the length of the horizontal segment. The effect of varying v , while keeping h constant at 2.87 mm ($\approx 1.46\times\lambda/4$), is presented in **Figure 5.4(a)**. Across all the three frequency bands, a downward tuning of the frequency profile, by approximately 650 MHz, is observed with when v is increased by 0.07 mm ($\approx 0.04\times\lambda/4$) between 2.79 mm ($\approx 1.42\times\lambda/4$) and 2.94 mm ($\approx 1.50\times\lambda/4$). With

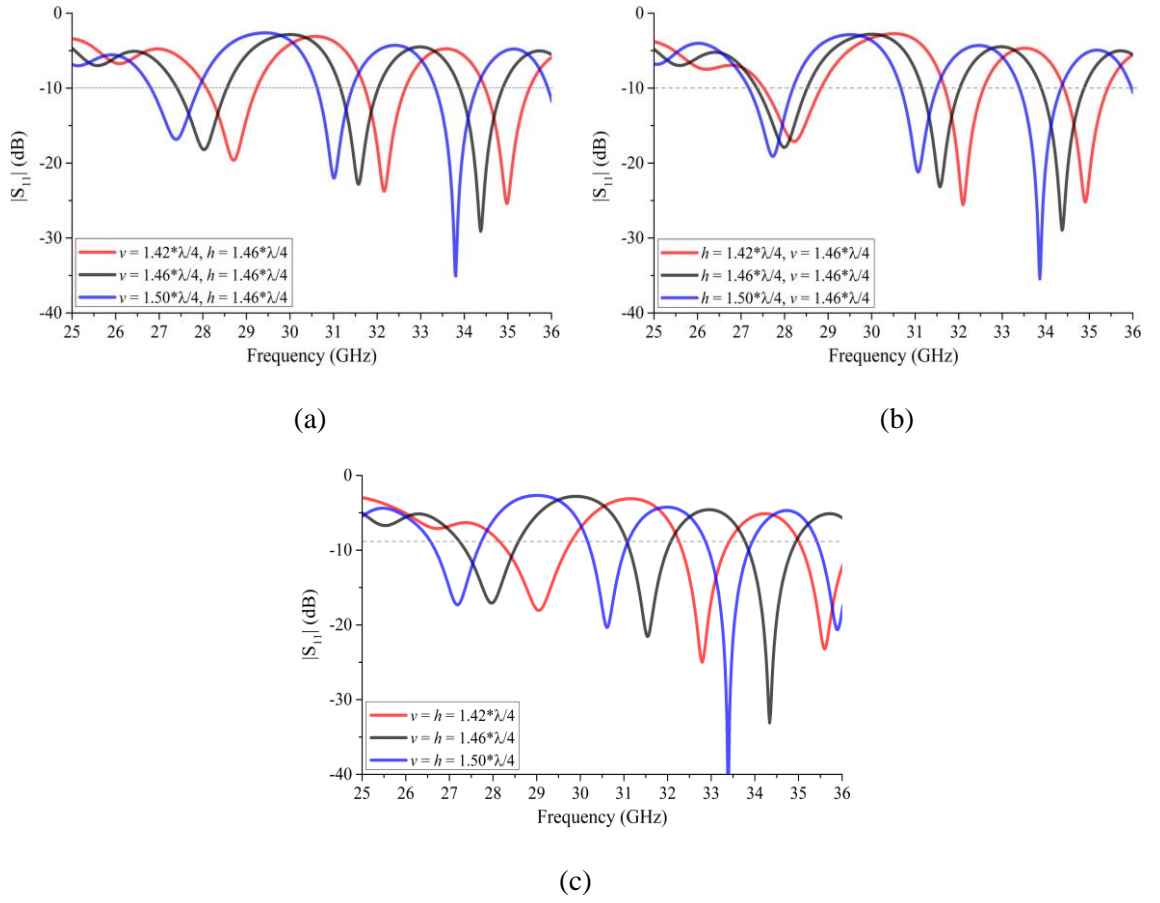


Figure 5.4. Effect of parametric variation on $|S_{11}|$ (a) varying v and keeping h fixed at $1.46 \times \lambda/4$ (b) varying h and keeping v fixed at $1.46 \times \lambda/4$ (c) varying h and v simultaneously.

this increase in v , the impedance matching minutely deteriorates in first and second resonant regions while significant improvement is observed in the third resonant region.

The effect of varying h between $1.42 \times \lambda/4$ and $1.50 \times \lambda/4$ is shown in **Figure 5.4(b)**. The vertical length, v , is kept fixed at $1.46 \times \lambda/4$ for this parametric study. From the figure it can be seen that increasing h by $0.04 \times \lambda/4$ tunes down the frequency profile in the first resonant region by 270 MHz and second and third resonant bands by approximately 500 MHz. An improvement in impedance matching is observed in the first and third resonant bands with increase in h .

Figure 5.4(c) shows the effect of varying the vertical and horizontal lengths, v and h , simultaneously and equally, on $|S_{11}|$. The frequency response tunes down by around 800 MHz as the lengths increase by $0.04 \times \lambda/4$ and behaves otherwise as the lengths of radiating and interconnecting elements decrease. The variation in lengths has no considerable effect on the bandwidth of the antenna however the impedance matching improves as the lengths are decreased from $1.50 \times \lambda/4$ to $1.42 \times \lambda/4$.

5.3.2 Inward Bent Segments

The effect of the inward bent segments, m , with 16 vertical elements and $h = 1.46 \times \lambda/4$, on $|S_{11}|$ is presented in **Figure 5.5**. Without these elements, the frequency response tunes up by approximately 450 MHz without any considerable improvement in bandwidth.

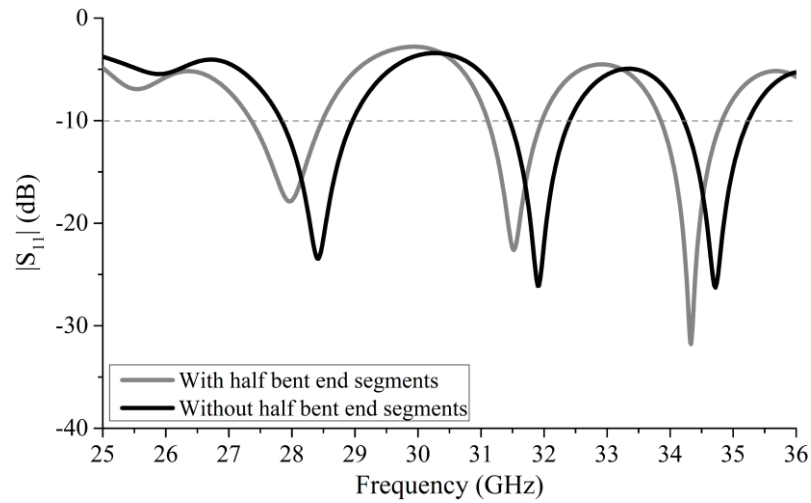


Figure 5.5. $|S_{11}|$ with and without $1.46 \times \lambda/8$ inward bent element with 16-element structure.

5.3.3 Odd Number of Elements

The parametric study described in Sections 5.3.1 – 5.3.2 is with 16 even number of elements for which the structure was fed in the middle of the structure i.e., horizontal seg-

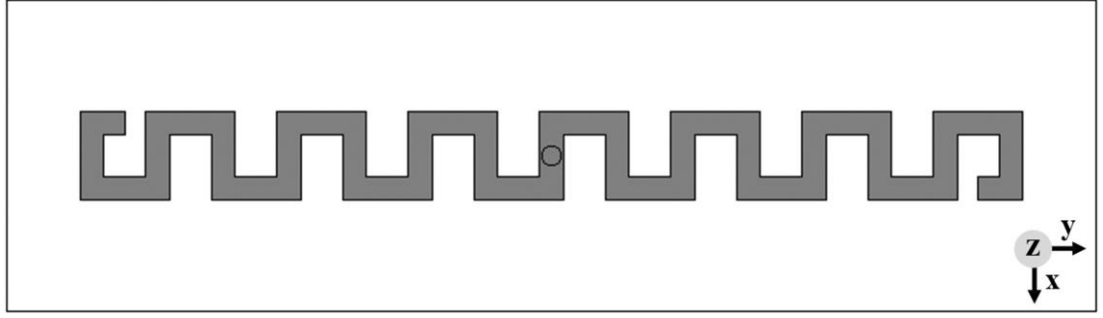


Figure 5.6. Geometry of Planar Bruce Array antenna with 15 vertical elements.

ent. **Figure 5.6** shows the geometry of the antenna with 15 vertical elements. The dimensions of the meander line are $v = h = 2.87$ mm and fed in the middle of the vertical segment to equally distribute the currents in the $+yz$ -plane and $-yz$ -plane making the structure a flipped mirror symmetry, with respect to the feed position, in yz -plane.

The $|S_{11}|$ plot in **Figure 5.7** shows the frequencies tuned down approximately 1.40 GHz with 15 vertical elements. The impedance bandwidth of the antenna, compared to the even 16-element structure has reduced by 300 MHz in the first band, 700 MHz in second band and by 320 MHz in the third frequency band.

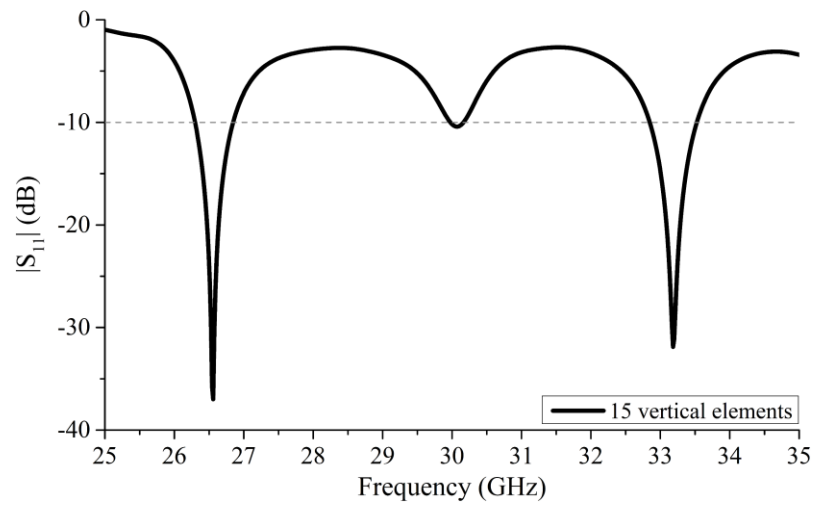


Figure 5.7. Simulated $|S_{11}|$ of Planar Bruce Array antenna with odd 15-elements.

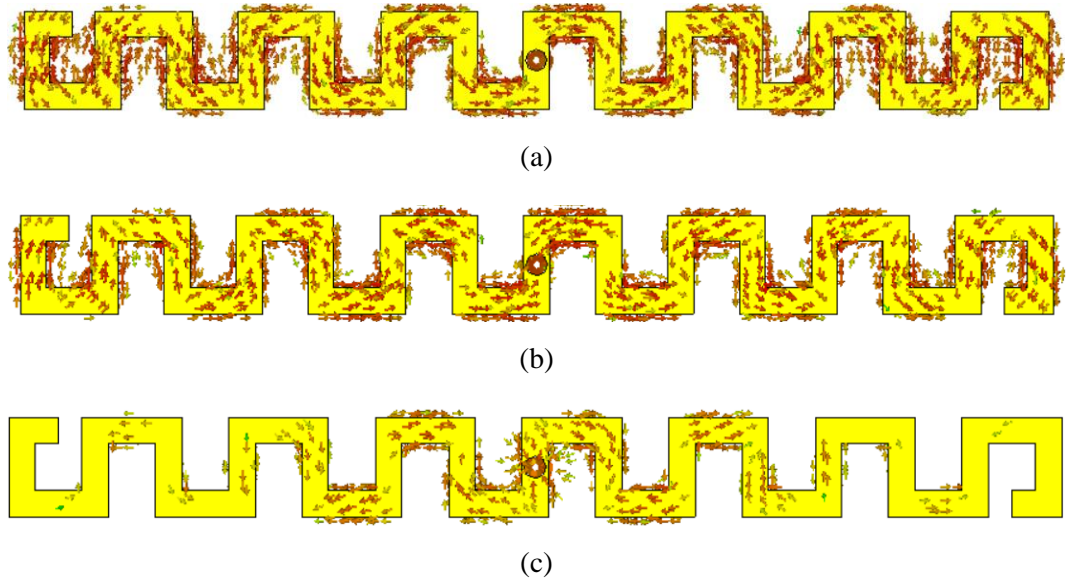


Figure 5.8. Current distribution of 15-element BAA at phase = 0 (a) 26.60 GHz (b) 29.90 GHz (c) 33.10 GHz.

The surface current distribution of the 15 vertical element structure is shown in **Figure 5.8**. At the three resonances identified in **Figure 5.7**, 26.60 GHz, 29.90 GHz, 33.10 GHz, the surface currents are distributed in both vertical and horizontal elements therefore acting as radiating elements. **Figure 5.9** shows dual beams 3D radiation patterns

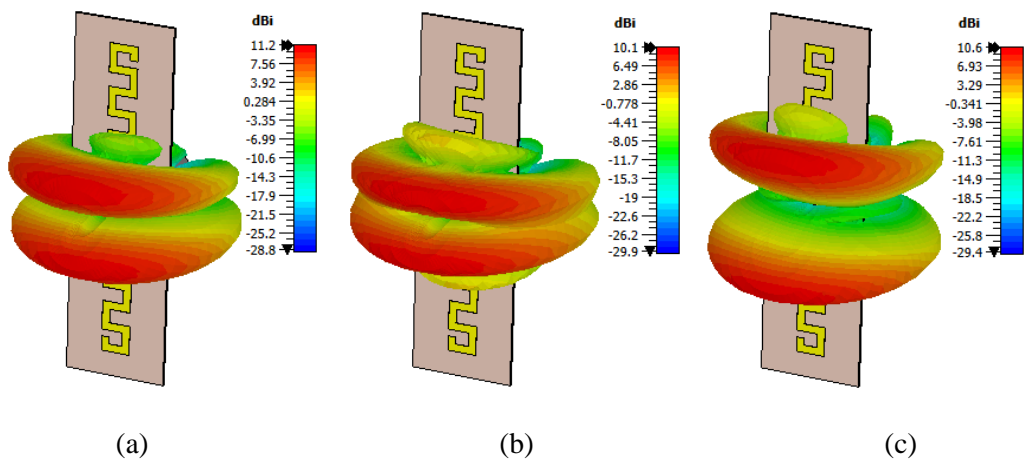


Figure 5.9. 3D radiation pattern of odd 15-element Bruce Array antenna structure (a) 26.60 GHz (b) 29.90 GHz (c) 33.10 GHz.

across all three frequency bands as a result of addition of the currents from both vertical and horizontal elements.

5.4 Results and Discussion

5.4.1 Impedance Bandwidth

The simulated and measured $|S_{11}|$ response of the 16-element centre-fed BAA, shown in **Figure 5.3**, with optimised dimensions shown in **Table 5.1**, is presented in **Figure 5.10**.

The antenna is measured using Rohde and Schwarz Vector Network Analyzer (ZVA40).

The simulated antenna has $|S_{11}| \leq -10$ dB between 27.36 GHz to 28.50 GHz, 31.13 GHz to 31.99 GHz and 33.85 GHz to 34.85 GHz while the measured response's operating range is between 27.48 GHz to 28.50 GHz, 30.66 GHz to 31.60 GHz and 33.80 GHz to 34.48 GHz. The simulated and measured fractional bandwidth are 9.72% and 8.66%, respectively.

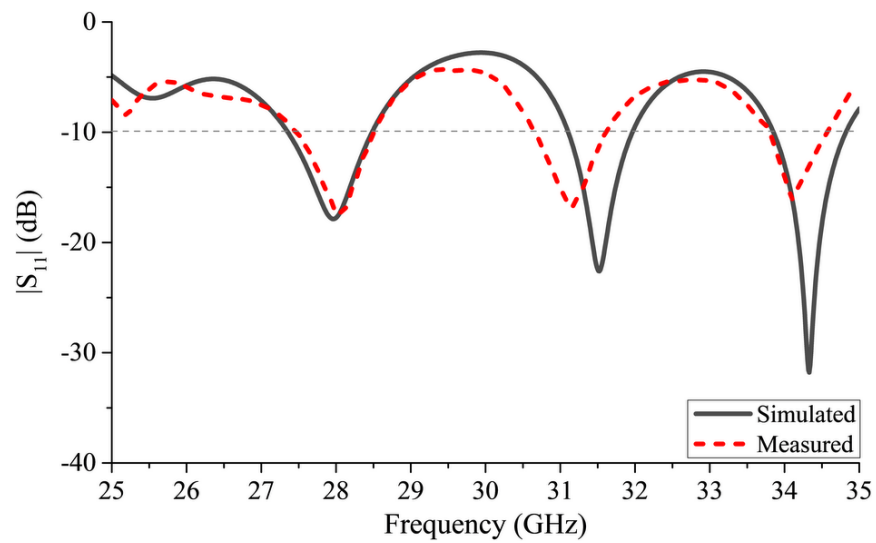


Figure 5.10. Simulated and measured $|S_{11}|$ of planar Bruce array antenna.

5.4.2 Efficiency

The simulated radiation and total efficiencies of the antenna are shown in **Figure 5.11**. The antenna has over 85% total efficiency in the operating frequency bands and has more than 90% efficiency at 28.0 GHz, 31.50 GHz and 34.30 GHz.

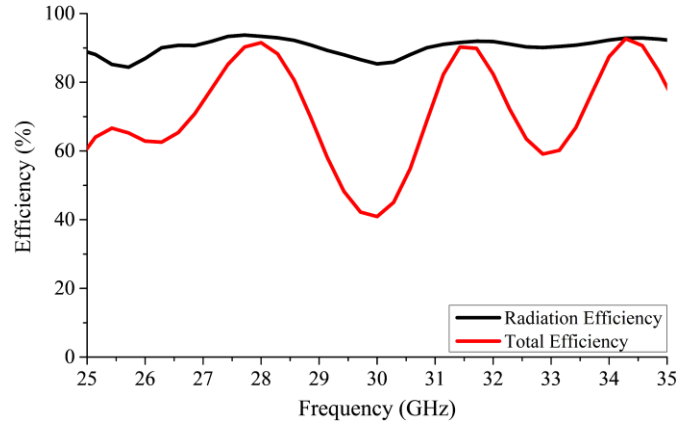


Figure 5.11. Simulated total and radiation efficiency of planar Bruce array antenna.

5.4.3 Current Distribution

Figure 5.12 shows the surface current distribution plots. As discussed in the wire Bruce array antenna theory in section 5.2, the vertical elements add in phase to give rise to radiation. The radiating vertical elements, at 28.0 GHz in **Figure 5.12(a)**, have high distribution of current than the horizontal elements which effectively means that the currents in the vertical elements will add-up in phase constructively to radiate. **Figure 5.12(b)** and **Figure 5.12(c)** show the current distribution at 31.54 GHz and 34.34 GHz, respectively. It can be seen from these figures that the currents are distributed in vertical and horizontal elements, of which, the latter behaved as interconnecting elements at 28.0 GHz. Since the antenna is fed from centre, the currents traveling in opposite direction are giving rise to dual beams in either direction as shown in **Figure 5.12(b)-(c)**.

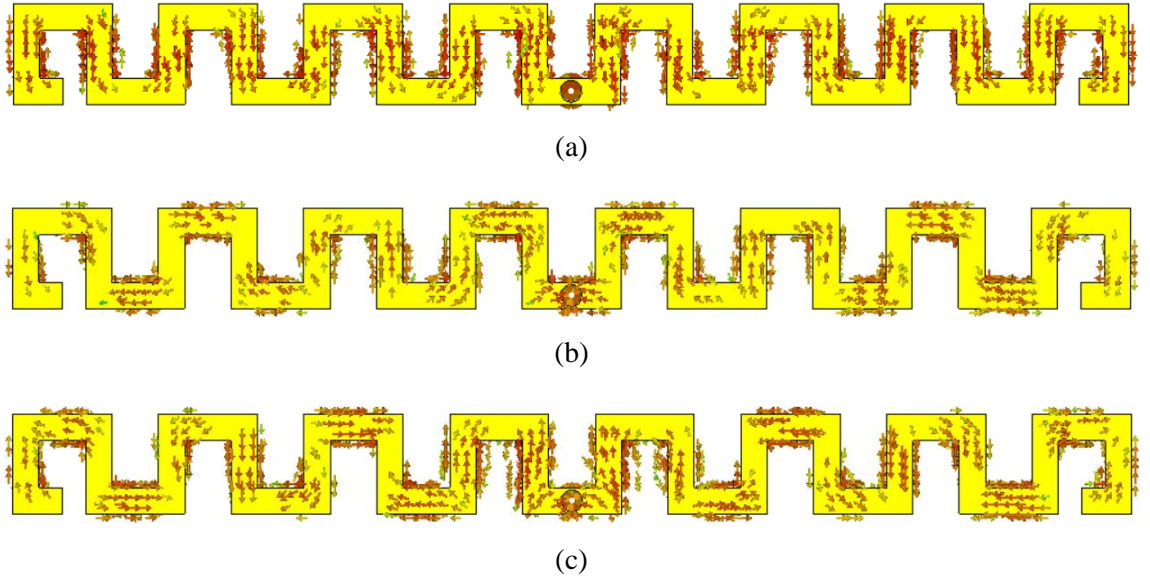


Figure 5.12. Current distribution of 16-element BAA at phase = 0° (a) 28.0 GHz (b) 31.54 GHz (c) 34.34 GHz.

5.4.4 Radiation Characteristics

The 3D visualisations of radiation patterns of the proposed antenna, with single and dual beams, at 28.0 GHz, 31.54 GHz and 34.34 GHz are shown in **Figure 5.13**.

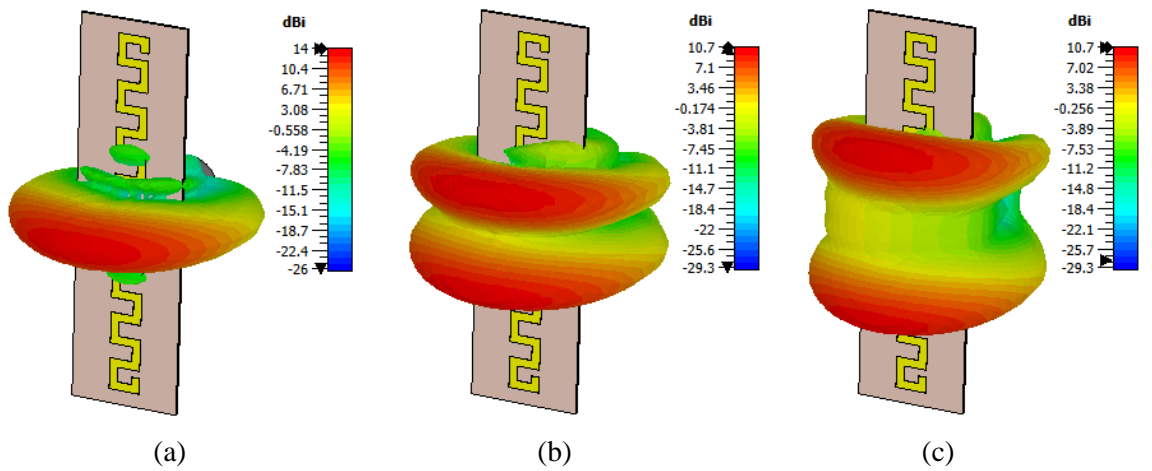


Figure 5.13. 3D radiation pattern plots at (a) 28.0 GHz (b) 31.54 GHz (c) 34.34 GHz.

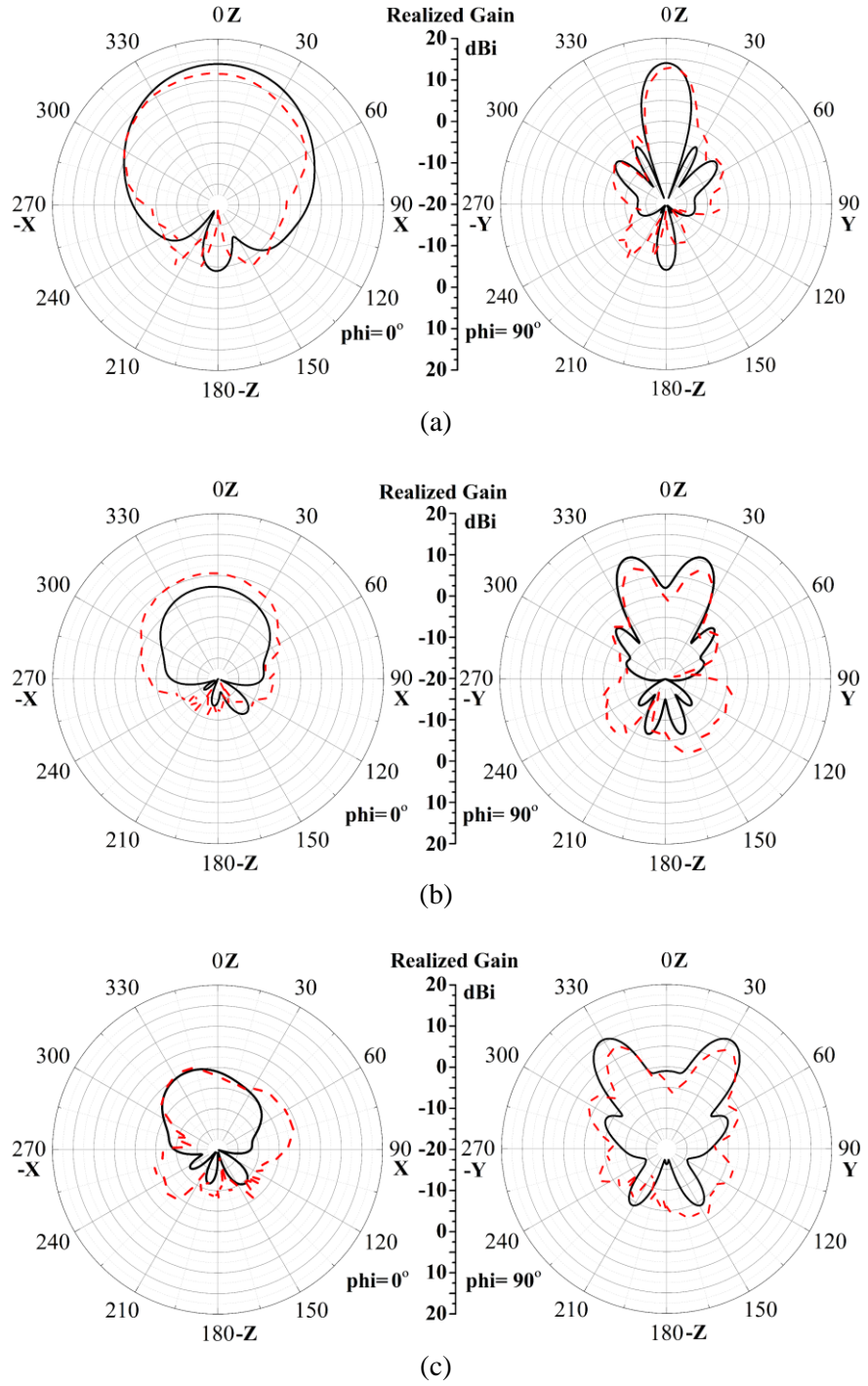


Figure 5.14. Simulated and measured xz-plane and yz-plane radiation pattern plots at (a) 28.0 GHz (b) 31.54 GHz (c) 34.34 GHz.

The simulated and measured radiation pattern plots are presented in **Figure 5.14**. The polar 2D plot of xz and yz-planes of the antenna, at 28.0 GHz, is shown in

Figure 5.14(a). The antenna has a highly directive radiation pattern with narrow HPBW thereby verifying the fan-beam radiation pattern. Dual beam patterns are observed at 31.54 GHz and 34.34 GHz with peak-to-peak angular separation of 34° and 62° , respectively, as shown in **Figure 5.14(b)** and **Figure 5.14(c)**. The antenna is symmetric to the substrate in xz-plane but the asymmetry in the feed position in yz-plane results in pattern tilt observed at 31.54 GHz and 34.34 GHz. The other radiation characteristics at these frequencies are presented in **Table 5.2**.

Frequency (GHz)	Realized Gain (dBi) Simulated/ Measured	HPBW (yz-plane)	SLL (dB)
28.0	14.0 / 12.94	17.0	-18.0
31.54	10.70 / 8.30	15.90	-14.0
34.34	10.70 / 8.10	17.50	-11.70

Table 5.2. Radiation characteristics of the proposed 16-element BAA.

5.5 Summary

This chapter discusses the novel transformation and implementation of conventional wire Bruce Array Antenna to printed planar technology for 5G and mm-wave applications, for the first time. The analysis of the antenna is performed with rear feeding arrangement with a full ground plane. A thorough parametric study is performed in terms of number of radiating elements, even and odd elements and variation in dimensions of the antenna. The study shows that for a compact and simple structure, having overall antenna dimensions of $35.0 \times 9.0 \times 0.254 \text{ mm}^3$, using the BAA's approach, a highly directional and high gain fan-beam, at broadside at 28.0 GHz, is obtained by feeding the an-

tenna through the center of the 16 radiating element structure for point-to-point communication applications. The proposed antenna has multi-band operation with frequency ranges between 27.36 GHz to 28.50 GHz, 31.13 GHz to 31.99 GHz and 33.85 GHz to 34.85 GHz, where the latter two bands have dual beam characteristics which provide radiation diversity in narrow passages.

A further iteration of Bruce array antenna is discussed in the next chapter for mm-wave and Ka-band applications to enhance the performance by introducing modifications to make the structure operate for leaky-wave frequency scanning operation.

Chapter 6

Millimeter-Wave Frequency Scanning Bruce Array Antennas

6.1 Introduction

As discussed in Section 2.5, the distinctive features of Leaky-Wave antennas (LWAs) are their wide impedance bandwidth, high gain, inexpensive and easy to fabricate geometry and elimination of phase shifters for beam-scanning thereby minimizing circuitry required in phased array antennas and reducing the energy consumption [145]. A variety of LWAs have been proposed based on different technologies which includes spoof surface plasmon transmission line (SSP-TL) structure [146]–[148], continuous transverse stub (CTS) based waveguide [149], substrate integrated waveguide (SIW) [148], [150]–[153], sharpening the bends [154], meander-line rampart array [155]–[157], slot or coplanar lines [158], composite right/left-handed structures (CRLH) [159], [160], squarely modulated reactance surface (SquMRS) [161], periodically loaded microstrip structures [162] and Goubau line structures [163], [164].

In order to perform scanning from backward to forward endfire regions, the *open-stopband* (OSB) limits scanning at broadside in which the incident power is reflected back to the source, rather than being radiated, due to coupling of a pair of contra-directional space harmonics (Floquet modes) resulting in severe gain degradation, when the

$n = -1$ space harmonic is excited [165]–[167]. From a physical perspective, at OSB, the traveling-wave behaves like a standing-wave type antenna where all the radiating elements of the array are excited with equal phase [145]. The problem of radiation in the broadside direction has been plaguing the research community for over forty years [165]. This OSB has adverse effect on the attenuation (leakage) constant, at broadside frequency range, due to which the LWAs suffer from impedance mismatching and gain degradation [168]. The gain degradation makes the antenna inefficient to scan seamlessly which, in turn, restricts the practical usability therefore if actions are not taken, the occurrence of the OSB renders the exploitation of the scanning characteristics useless [145], [169].

Several methods have been presented in the literature to mitigate or suppress the effects of OSB at broadside. In [40], balanced transmission line in metamaterial LWAs is used to increase gain from backward endfire to broadside having bandwidth between 24 GHz to 27 GHz with scanning range from -17° to 13° . The balanced transmission line approach is also used in [170] in which a complex three-layer waveguide structure is used to mitigate OSB effect and achieve scanning range between -29° to $+31^\circ$. Width variation of transversal lines in meandered unit-cell is another approach adopted in [155], which results in 118° scanning space between 3.70 GHz and 6.80 GHz with peak gain of 10 dBi however the sidelobe level is not taken into consideration as it deteriorates towards scanning in either endfire direction. Shorting vias in periodic SIW structure, on substrate with relative permittivity of 10.2, have been used to mitigate the effects of OSB in [150] to achieve scanning range of 103° between 13.20 GHz and 15.60 GHz. Although the scanning is rapid and utilizes less bandwidth, the depth resolution for wide scanning imaging systems requires high bandwidth [171] and using shorting vias adds complexity to the

structure for fabrication compared to a planar geometry. The use of quarter-wave transformers in 1.575 mm thick combline structure around 10 GHz [166] and stub matching around 26.50 GHz [167] have also shown promising results to suppress the OSB however both structures have very narrow bandwidth with overall scanning space less than 10° . An approach of using non-identical elements in the unit-cells of 0.80 mm thick combline SIW structure, presented in [172], also assists in suppression of the OSB. A lattice network approach is applied on periodic structures at lower frequencies between 0.85 GHz to 1.15 GHz and 4.80 GHz to 6.80 GHz focusing on the suppression of the OSB with no mention about the overall scanning range [173]. A detailed comparison, along with the proposed antennas, is presented in Section 6.5.

In this chapter, two approaches to transform the wire BAA structure to edge-fed printed LWA are discussed. As discussed in Chapter 5, the periodically modulated wire BAA was designed for radio ham applications in which a long wire antenna was bent at equal intervals. A configuration of 11 vertical elements, conventionally fed using twin-line feed from the center, is shown in **Figure 6.1**. Having been around for nearly a century and despite the simplicity of structure, the research community has not extended the concept of BAA for further research. Apart from the work presented in Chapter 5 [144], only a handful research works are found that have used the BAA structure for modern antenna technology [140], [141]. In the first approach, presented in this chapter, a quasi-periodic

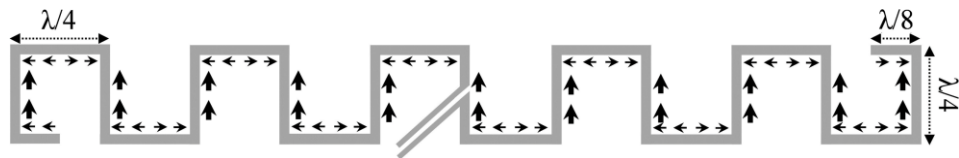


Figure 6.1. A twin-line fed geometry of conventional meandered 11 vertical element wire BAA showing magnitudes and direction of current distribution with in-phase vertical elements.

array, using wire BAA theory and the mitigation of the OSB effect at broadside, by optimizing the vertical and horizontal lengths, is discussed. The unit-cell of the antenna is a meander line structure designed at the broadside frequency. The improved case unit-cell, having low attenuation constant resulting in mitigation of OSB, is further investigated to increase the realized gain of the structure by making a dual Bruce array using a Klopfenstein tapered feed which shows good performance throughout the K-Band (18.0 GHz – 27 GHz) and Ka-Band (26.50 GHz – 40 GHz). In the second approach, a modification of planar, edge-fed, periodic array using meandering concept of conventional wire BAA geometry and the suppression of the OSB around broadside, by replacing horizontal and vertical segments with semi-circular and novel bowtie elements, respectively, is presented. The numerical results and optimizations have been performed using CST Microwave Studio where the effects of metallization and dielectric losses are properly considered. The prototypes of these antennas have been fabricated and the measurement results have been compared to the simulated data through which good agreement is obtained.

6.2 Edge-Fed Planar Bruce Array Antenna

6.2.1 Conventional Unit-Cell

6.2.1.1 Geometry of Unit-Cell

The geometry of the unit-cell, with full ground plane, is presented in **Figure 6.2**. As mentioned earlier, according to the BAA's theory, the vertical and horizontal lengths of the meandered structure, v and h , are both approximately a quarter-wavelength long for HF/VHF applications but because the $\lambda/4$ gap between the vertical elements is so small in

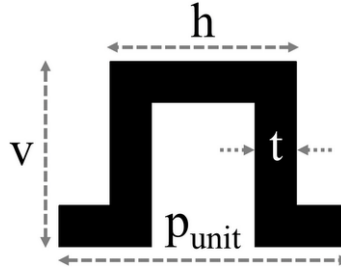


Figure 6.2. Geometry of meandered unit-cell printed on a 0.254 mm thick grounded Arlon DiClad 880.

the mm-wave region, the mutual coupling results in multiple resonances. Therefore, these lengths have been modified and increased to mitigate this effect. The thickness of the trace, t , is 0.76 mm and period of the unit-cell, p_{unit} , equals $2 \times (h - t)$.

Figure 6.3(a)-(b) show the effect of variation of horizontal and vertical lengths of the unit-cell on the normalized attenuation constant (α/k_0) and phase constant (β_{-1}/k_0), res-

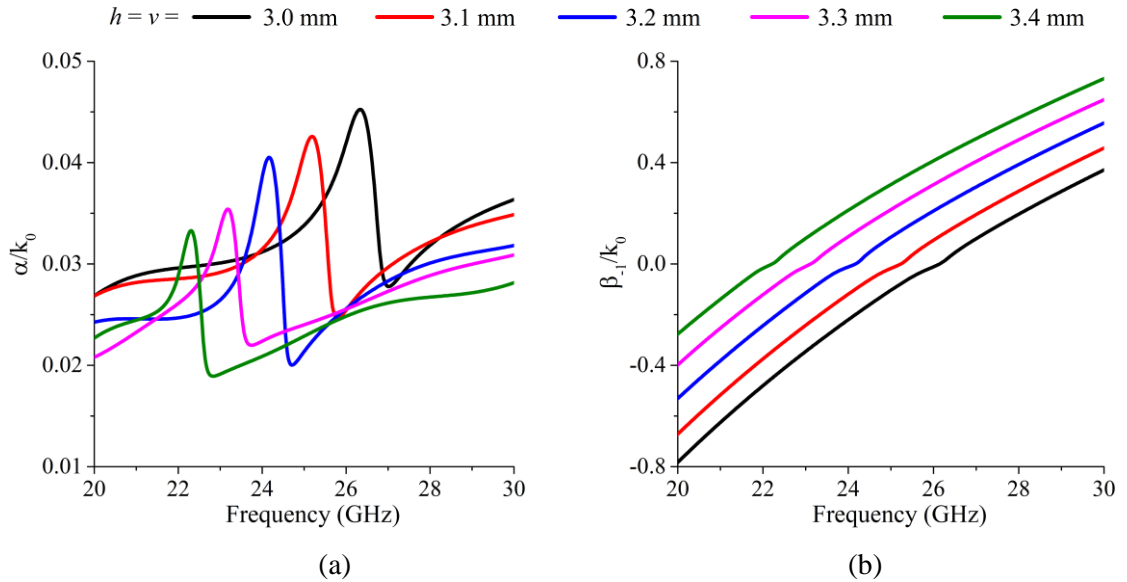


Figure 6.3. (a) Attenuation constant and (b) phase constants normalized to the free-space wavenumber (k_0) for the unit-cell consistent with conventional wire BAA theory varying lengths v and h simultaneously.

pectively. The prominent *bump* in the α/k_0 plot, **Figure 6.3(a)** represents the region of OSB at broadside ($\beta_{-1}/k_0 = 0$). The width of the trace, t , is fixed at 0.76 mm on the dielectric substrate with $\epsilon_r = 2.2$. As both lengths of the unit-cell, h and v , are increased simultaneously from 3.0 mm to 3.40 mm, the magnitude of the bump of α/k_0 decreases however the frequency tunes down by approximately 900 MHz with every 0.10 mm increment in the lengths of h and v . This pattern is also observed in **Figure 6.3(b)** where the OSB frequency shifts with increase in h and v . It should also be noted that the HPBW in the yz -plane becomes narrower as the amplitude of α/k_0 is reduced due to the increase in p_{unit} .

6.2.1.2 Results of Bruce Array Antenna based on Conventional Unit-Cell

Figure 6.4 presents the geometry of BAA structure based on the unit-cell presented in **Figure 6.2**. The structure consists of a transmission line of length 6.37 mm, connected to a series of 11 meander line unit-cell elements which is then terminated with a matched load of 50 Ω . The structure is printed on 0.254 mm thick Arlon DiClad 880 substrate with ϵ_r of 2.2 and loss tangent of 0.0009 with 0.035 mm copper cladding on both sides.

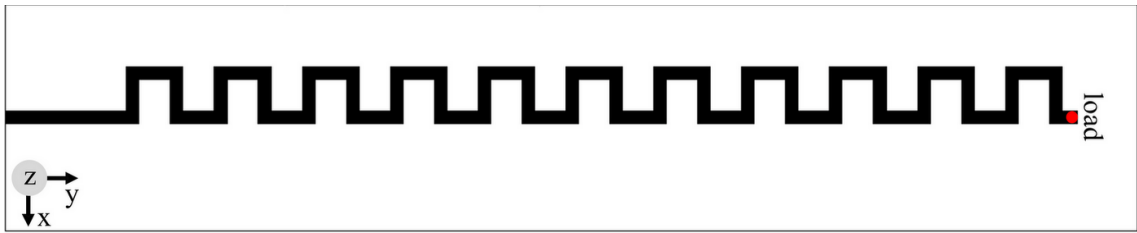


Figure 6.4. Geometry of a 1-D periodic edge-fed BAA-LWA based on conventional equi-dimensional unit-cell printed on a 0.254 mm thick grounded Arlon DiClad 880.

The effect of number of vertical elements in the structure is shown in **Figure 6.5**. A large number of unit-cells in the structure prevents the increase in gain due to the lower

power delivered to the last unit-cells therefore an optimum number of unit-cells is sought to get high gain on smaller footprint while having adequate HPBW. **Figure 6.5(a)** shows the $|S_{11}|$ when the number of vertical elements is increased in the structure from 19 to 25 which essentially means that with every 2 vertical elements, a unit-cell is added to the structure. The $|S_{11}|$ increases in the OSB region around 22.50 GHz however the region gets narrower. As is the case with linear arrays, the addition of unit-cells in series increases the realized gain however the HPBW in the scanning plane, shown in **Figure 6.5(b)**, is observed to decrease as the longitudinal length of the structure increases.

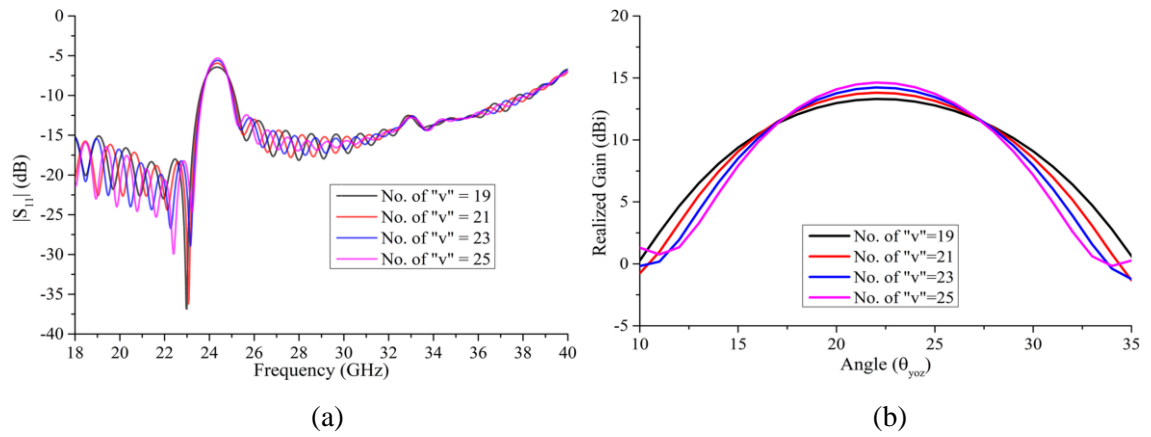


Figure 6.5. Simulated Effect of adding number of vertical elements in BAA (a) $|S_{11}|$ (b) HPBW.

Figure 6.6 shows the simulated and measured S-parameter plot of the 11 unit-cell element structure with equal v and h dimensions of 3.40 mm. The antenna has a wide bandwidth and has $|S_{11}| \leq -10$ dB below 21.96 GHz and from 22.80 GHz to 36.0 GHz. The region between 21.96 GHz and 22.80 GHz shows mismatching which is consistent with the OSB region, identified in **Figure 6.3** for when v and h are 3.40 mm.

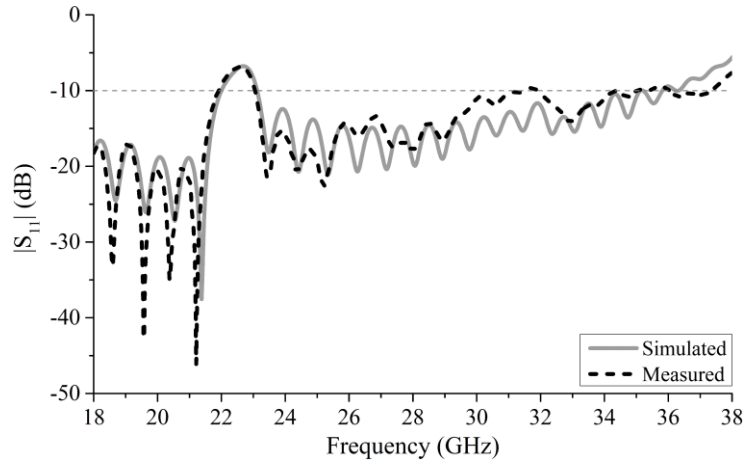


Figure 6.6. Simulated and measured $|S_{11}|$ plot of 11 unit-cell elements with conventional equi-dimensional v and h .

The realized gain of the BAA based on conventional equi-dimensional unit-cell with v and h of 3.40 mm is presented in **Figure 6.7**. Severe degradation of realized gain at 22.50 GHz is observed which is consistent with the earlier identified OSB region. Another gain drop is observed between 31.0 GHz and 35.20 GHz as the sidelobe level increases with the rise of back lobe when the beam scans from broadside to the forward endfire direction.

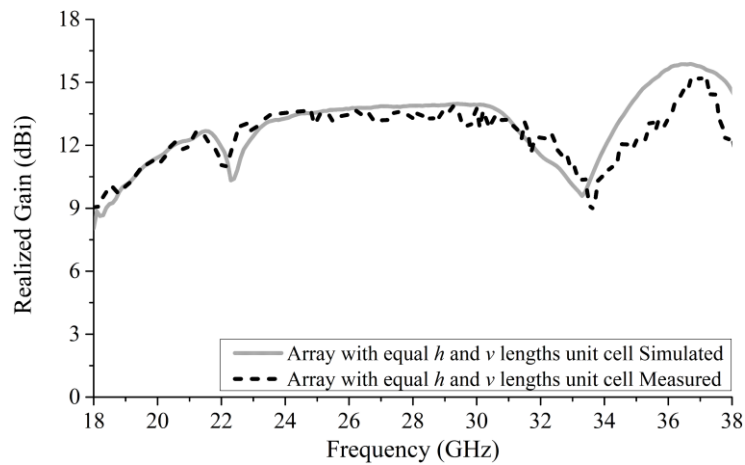


Figure 6.7. Simulated and measured realized gain plot of 11 unit-cell elements with conventional equi-dimensional v and h .

Figure 6.8 shows the scanning range of the periodic planar BAA, in the forward endfire direction, with conventional equal h and v lengths of the unit-cell (3.40 mm). The antenna has a wide scanning range between 0° and 55° . Although the bump of α/k_0 improves at 3.40 mm, as the lengths are simultaneously increased with this conventional unit-cell with equal h and v , as shown in **Figure 6.3**, the gain at the broadside frequency i.e., 22.50 GHz, degrades and recovers from 4° therefore resulting in inefficient scanning at the broadside frequency.

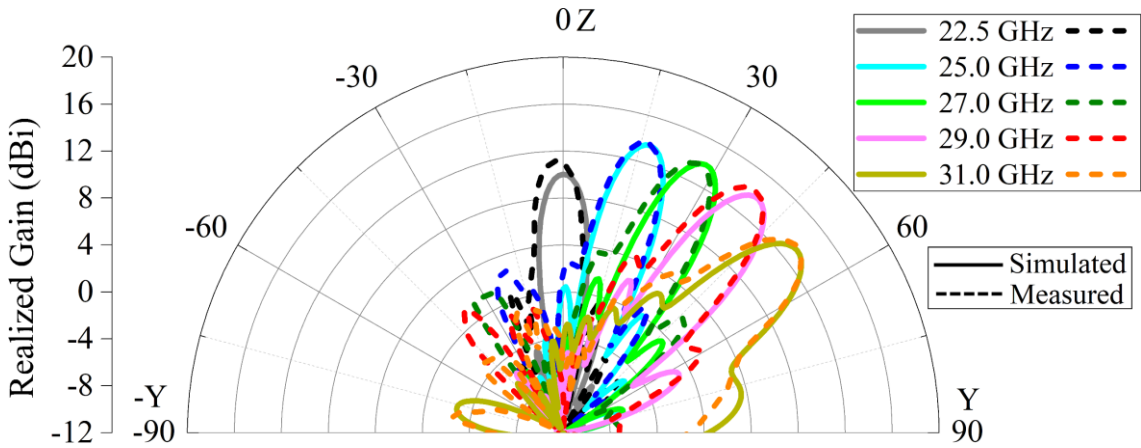


Figure 6.8. Scanning in forward quadrant of planar 11 element BAA with equal 3.40 mm conventional dimensions with broadside gain degradation.

6.2.2 Modified Bruce Array Antenna Structure

6.2.2.1 Modified Unit-Cell Analysis

In order to mitigate the OSB at broadside identified in **Figure 6.3**, the lengths of the unit-cell, h and v , are varied in such a way that the frequency does not tune up or down. The normalized attenuation and phase constant plots of unit-cells, in case of both conventional equi-dimensional h and v with 3.40 mm ($\approx 1.39 \times \lambda/4$) lengths and improved unit-cell, when h and v are modified to 3.46 mm ($\approx 1.42 \times \lambda/4$) and 3.34 mm ($\approx 1.37 \times \lambda/4$), respecti-

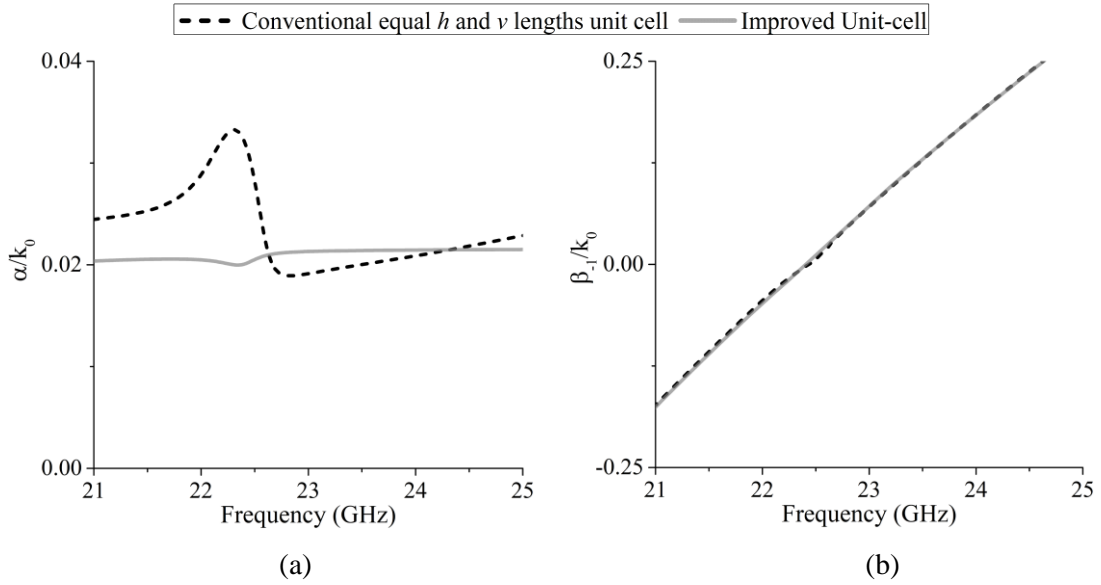


Figure 6.9. (a) Attenuation constant and (b) phase constants normalized to the free-space wavenumber (k_0) with conventional and proposed modified dimensions of h and v showing mitigation of open-stopband effect.

vely, is presented in **Figure 6.9**. As wavelength is inversely proportional to frequency, this increment in length of h reduces the input reactance of the antenna structure and decrement in the length of v allows to prevent the tuning of the broadside frequency. The absence of bump and significant amplitude reduction of the attenuation constant, in **Figure 6.9(a)**, at broadside frequency for the improved unit-cell, i.e., between 22.0 GHz and 23.0 GHz, validates the mitigation of the OSB. The frequencies for which $\beta_{-1}/k_0 < 0$ and $\beta_{-1}/k_0 > 0$, in **Figure 6.9(b)** represents scanning in the backward and forward endfire directions, respectively.

The dispersion diagram of the modified BAA's unit cell is shown in **Figure 6.10**. Three distinct radiation regions in three frequency bands are apparent. In the first and third region, the structure has backward radiation characteristics whereas the second radiation region exhibits forward radiation properties. The 'Air line' is given by $k_0 p_{unit}$.

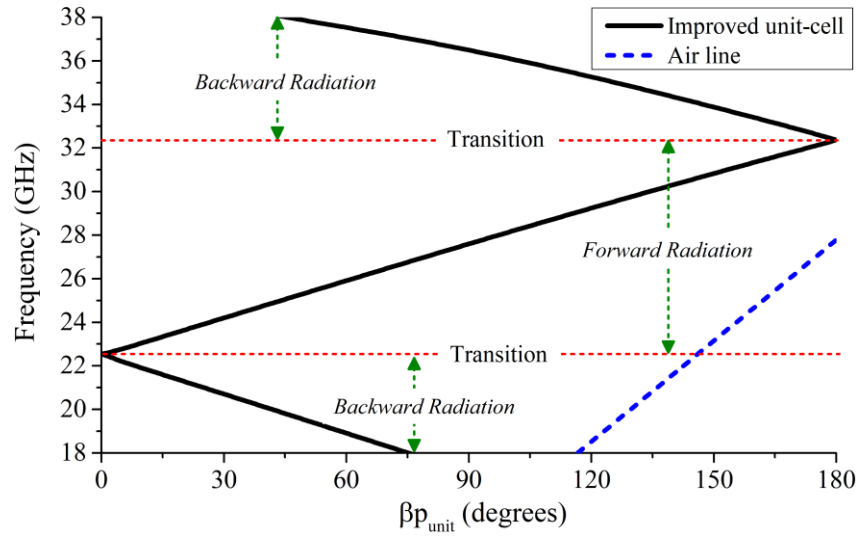


Figure 6.10. Dispersion diagram of modified BAA unit cell.

6.2.2.2 Edge-Fed Modified Bruce Array Antenna Geometry

The improved unit-cell, with modified v and h , is added in series to form an array of 11 unit-cells with an element h_s , terminated with $\sim 50 \Omega$ thick film surface mount resistor, as shown in **Figure 6.11(a)**. The overall dimensions of the quasi-periodic BAA, with improved unit-cell and h_s element, are $70.0 \times 13.50 \times 0.254 \text{ mm}^3$ [174]. The fabricated prototype presented in **Figure 6.11(b)** is fed using Southwest Sub-Miniature K-Type (SMK) connector and measured using Rohde and Schwarz Vector Network Analyzer (ZVA40). The dimensions of the structure are presented in **Table 6.1**.

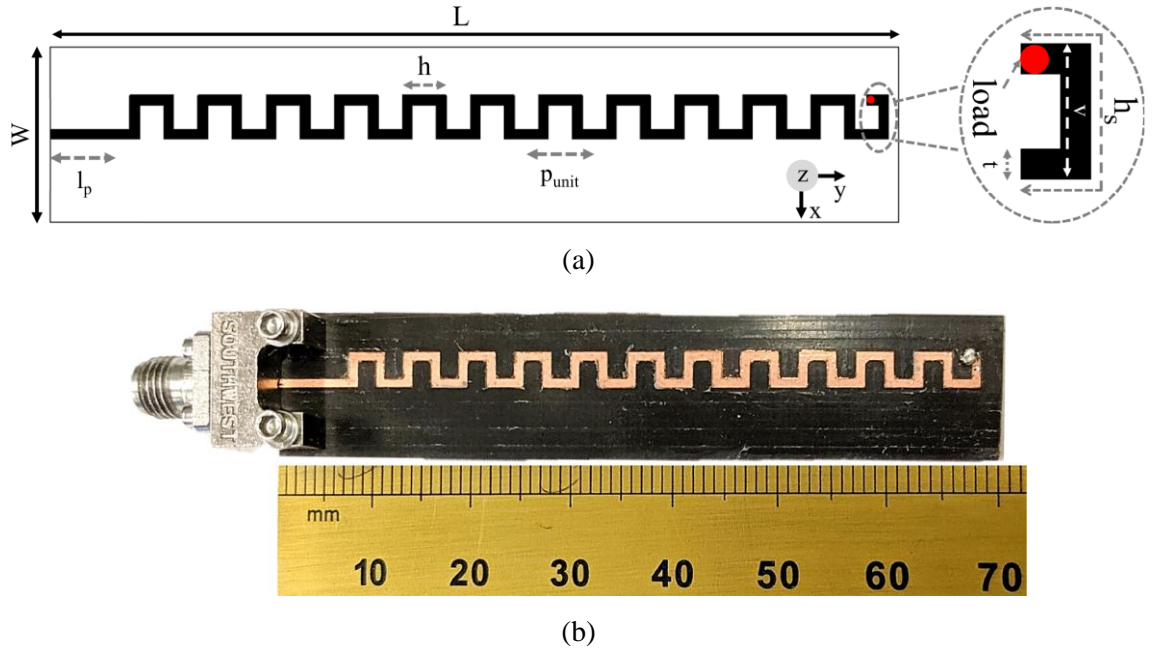


Figure 6.11. (a) Geometry with detail of the h_s element and (b) prototype of a 1-D quasi-periodic BAA-LWA printed on a 0.254 mm thick grounded Arlon DiClad 880.

Parameter	Symbol	Size (mm)
Width of antenna	W	13.50
Length of antenna	L	70.0
Length of inward bent end element	h_s	6.80
Vertical length of unit-cell	v	3.34
Horizontal length of unit-cell	h	3.46
Width of trace	t	0.76
Length of transmission line	l_t	6.37
Period of unit-cell	p_{unit}	5.40

Table 6.1. Design parameters of Bruce array antenna with modified unit-cell.

6.2.2.3 Results and Discussion

6.2.2.3.1 Impedance Bandwidth

Figure 6.12 shows the simulated and measured $|S_{11}|$ plots of the BAA structure with and without the h_s element. As opposed to the equal lengths case, shown in **Figure 6.6**, the mismatching in the OSB region improves considerably without any tuning of frequency. While the improvement in the mismatching region is obvious, the $|S_{11}|$ is slightly greater than -10 dB between 22.46 GHz and 22.85 GHz without h_s element. In the second case, with the addition of the inward bent element, h_s , to the periodic structure, the impedance matching in the OSB region improves. The antenna has $|S_{11}| \leq -10$ dB from below 18.0 GHz to 37.20 GHz.

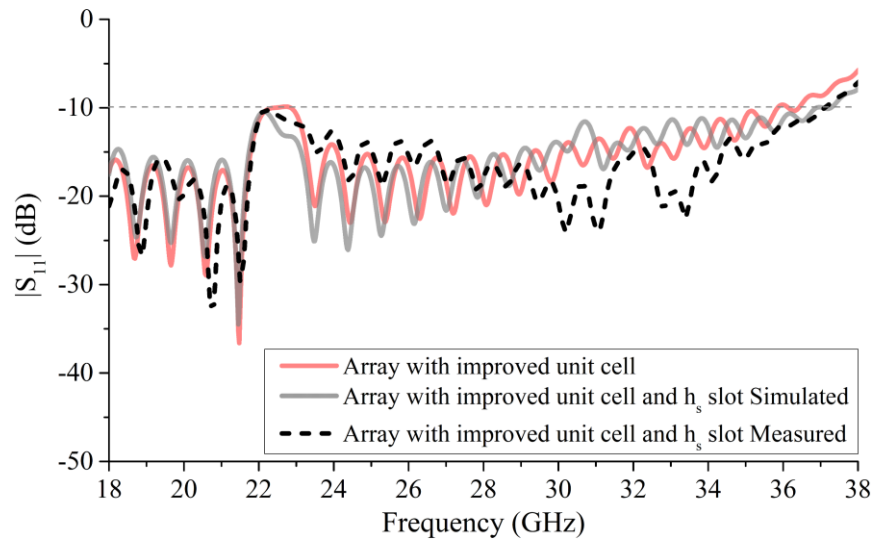


Figure 6.12. Simulated and measured $|S_{11}|$ plot of 11 unit-cell elements with improved unit-cell and the addition of h_s element to the periodic structure.

6.2.2.3.2 Realized Gain

The simulated and measured realized gain of the BAA structure, with h_s element, is shown in **Figure 6.13**. The gain in the mitigated OSB region is noticeably better and has increased to 12.90 dBi at 22.50 GHz, i.e., the broadside frequency, compared to 10.02 dBi with equal lengths case shown in **Figure 6.7**.

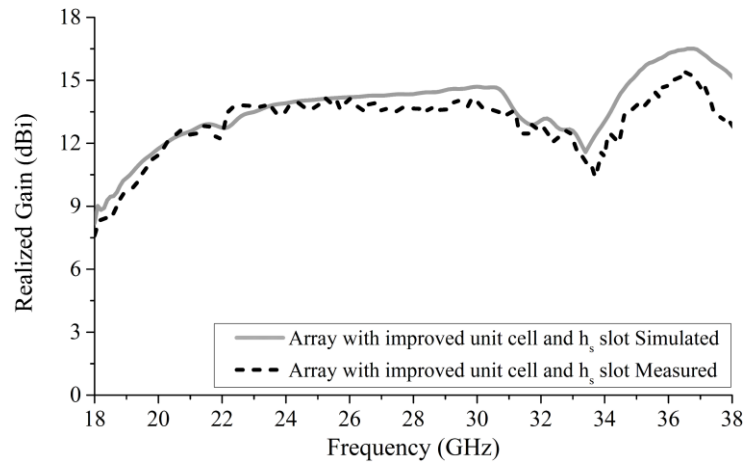


Figure 6.13. Simulated and measured realized gain plot of 11 unit-cell elements with improved unit-cell and the addition of h_s element to the periodic structure.

6.2.2.3.3 Main Beam Direction and SideLobe Level

The simulated main beam direction of the antenna is presented in **Figure 6.14(a)**. Two clear scanning ranges are observed between 18.0 GHz to 33.30 GHz and 33.32 GHz to 38.0 GHz. The modified BAA has wide bandwidth and high gain for wide area scanning but, as the main lobe approaches forward endfire, the back lobe rises and the SLL increases. Therefore, an SLL threshold of -10 dB is considered as the benchmark of scanning range as shown in **Figure 6.14(b)**. The BAA with modified unit-cell element and h_s element has $SLL \leq -10$ dB between 18.0 GHz to 31.20 GHz and 35.30 GHz to 37.20 GHz.

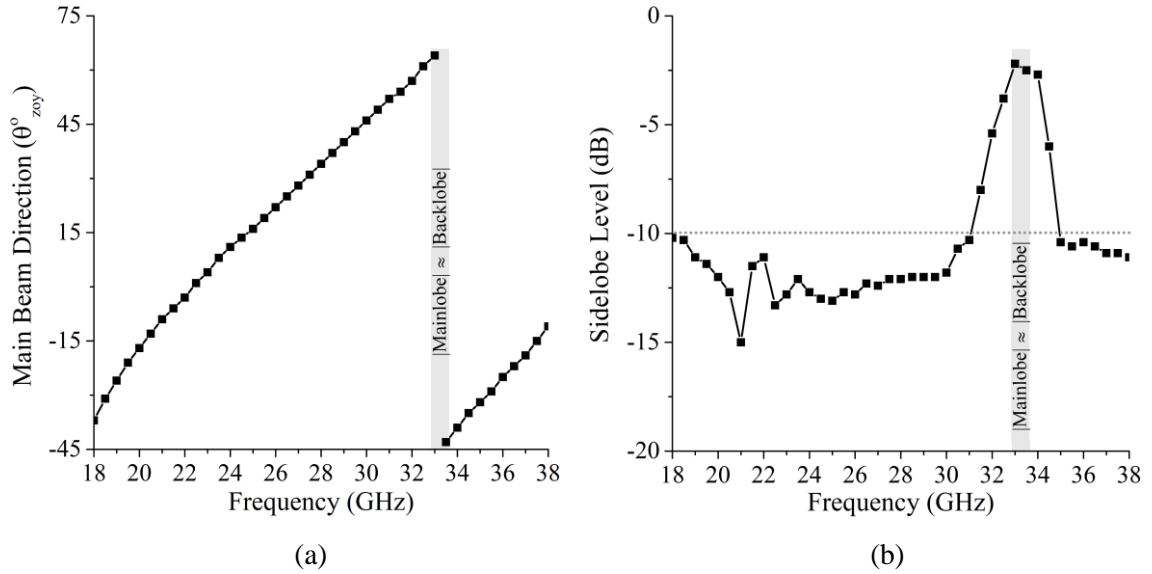


Figure 6.14. (a) Main beam direction and (b) Sidelobe Level plots of BAA with modified dimensions of h and v .

6.2.2.3.4 Scanning Range

Figure 6.15 shows the scanning ranges of the planar BAA with h_s element. In the first scanning range, presented in **Figure 6.15(a)**, the antenna scans the space from -38° at 18.0 GHz and the realized gain gradually stabilizes from backward endfire region as it approaches broadside. The antenna scans seamlessly through the broadside until 55° , i.e., 31.20 GHz, and has stable gain as shown in **Figure 6.15(b)**. Although bandwidth is available after 31.20 GHz to scan, the SLL degrades and becomes greater than -10 dB until it reaches the point that the back and main lobes become equal at 33.30 GHz resulting in a dual beam with 110° angular separation. As the beam continues to scan, the main and back lobes switch roles after 33.30 GHz and the SLL becomes -10 dB at 35.30 GHz enabling a second scanning space in the backward endfire region as shown in **Figure 6.15(c)**. The second scanning space of the antenna ranges from -31° to -17° between 35.30 GHz and 37.20 GHz after which the next OSB limits scanning through

broadside. This additional scanning range may not be used in continuation with the first scanning space, but it may be utilized for short range scanning or fixed frequency applications.

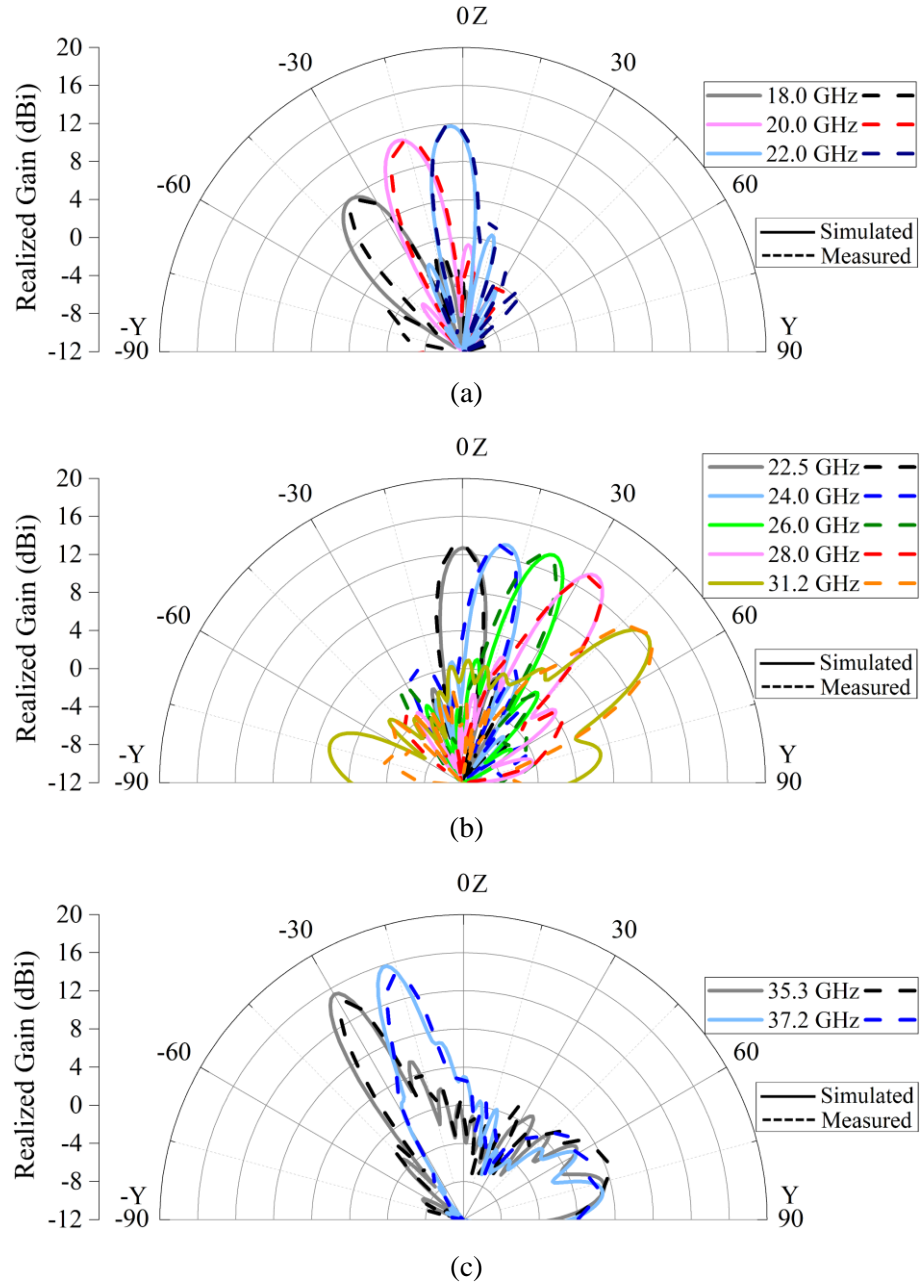


Figure 6.15. Proposed 1-D quasi-periodic BAA-LWA with improved unit-cell dimensions (a) 1st scanning range in backward quadrant (b) 1st scanning range in forward quadrant and (c) 2nd scanning range after role reversal of main and back lobe.

6.2.2.3.5 Half Power BeamWidth and Radiation Efficiency

Figure 6.16 shows the HPBW of the BAA in xz and yz-plane. In the xz-plane, as the back lobe rises, the HPBW experiences a decline after 31.0 GHz and recovers from 34.0 GHz as the sidelobe level recovers. The yz-plane shows a consistent narrow beam scanning in both scanning ranges which may be categorized as fan-beam radiation pattern. **Figure 6.16** also shows the radiation efficiency for the proposed BAA. It is observed that the radiation efficiency of BAA is around 20% – 78%. The low radiation efficiency is a common trait of the LWAs because of the dissipation of power, that does not radiate, at the termination load as the wave travels towards the end of the structure [175].

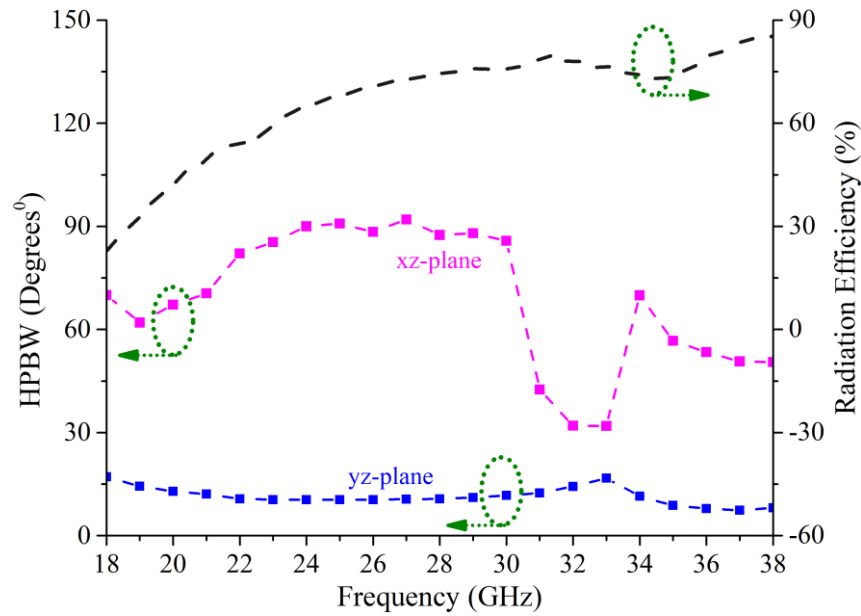


Figure 6.16. Simulated HPBW and Radiation Efficiency of the proposed BAA.

6.3 Dual Bruce Array Antenna

6.3.1 2-Way Klopfenstein Taper Feedline Divider

The conventional power divider techniques, such as Wilkinson power splitters using quarter-wave transformers, are usually applicable for narrow-band frequencies. In order to achieve $|S_{11}| \leq -10$ dB over a wide frequency band for a linear array, a two-way Klopfenstein tapered power divider is proposed in this section. The concept of Klopfenstein taper originates from stepped Chebyshev transformer as the number of sections, of different impedances, increases to infinity [176], [177]. The input reflection coefficient, ρ , for a continuous taper, for maximum achievable bandwidth and a fixed peak magnitude of reflection coefficient, takes the form [178]:

$$\rho = \rho_0 \frac{\cos [\sqrt{(\beta l)^2 + A^2}]}{\cosh (A)} e^{-j\beta l} \quad (6.4)$$

where l and β are the taper length and wavenumber, respectively. In the passband, the parameter A controls reflection coefficient's peak magnitude over the entire frequency range such that $\beta l \geq A$. The value of ρ_0 is calculated using (6.5) taken from [179]:

$$\rho_0 = 0.5 \ln \left(\frac{Z_2}{Z_1} \right) \quad (6.5)$$

where Z_1 and Z_2 are the characteristic impedances at either end of the taper.

6.3.1.1 Geometry of Taper Feedline Divider

The design of a wideband two-way power divider based on Klopfenstein feedline taper is shown in **Figure 6.17**. The taper transitions from $50 \, \Omega$ to $25 \, \Omega$ through 13 stepped sections, with combined length l , and the optimized physical dimensions of each section are

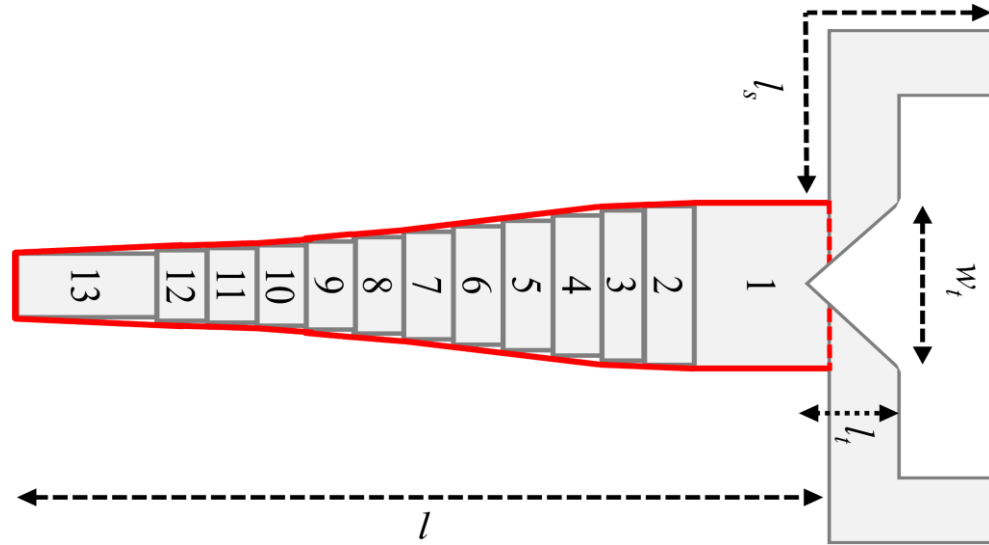


Figure 6.17. Geometry of Klopfenstein taper showing stepped discrete blocks from 25 Ω to 50 Ω , outlined smooth taper and two-way divider.

Block	Z_0 (Ω)	Size (mm ²)	Parameter	Symbol	Size (mm)
1	25.0	1.48×1.96	Taper length	l	8.94
2	25.78	0.54×1.89	Split junction length	l_s	3.43
3	26.91	0.54×1.79	Triangle perpendicular length	l_t	0.90
4	28.42	0.54×1.67	Triangle base length	w_t	1.80
5	30.26	0.54×1.54			
6	32.36	0.54×1.41			
7	34.79	0.54×1.28			
8	37.62	0.54×1.15			
9	40.16	0.54×1.05			
10	42.76	0.54×0.96			
11	45.04	0.54×0.89			
12	46.83	0.54×0.84			
13	50.0	1.52×0.76			

Table 6.2. Geometric details of two-way Klopfenstein taper feed divider.

tabulated in **Table 6.2**. Ideally, the Klopfenstein taper is a smooth and continuous transition therefore, a curve is formed out of the outer edges of each section. Finally, a junction branching from *block 1*, i.e., $25\ \Omega$, to two $50\ \Omega$ lines is added and a triangular section, with dimensions w_t and l_t , is notched for equal power distribution.

6.3.1.2 Impedance Bandwidth of Klopfenstein Divider

Figure 6.18 shows the $|S_{11}|$ response of the standalone taper presented in **Figure 6.17**. The discrete stepped taper has $|S_{11}| \leq -25\ \text{dB}$ from 18 GHz to 40 GHz which includes K-Band and Ka-Band regions whereas the smooth taper improved the matching performance to $-30\ \text{dB}$ for the same frequency range.

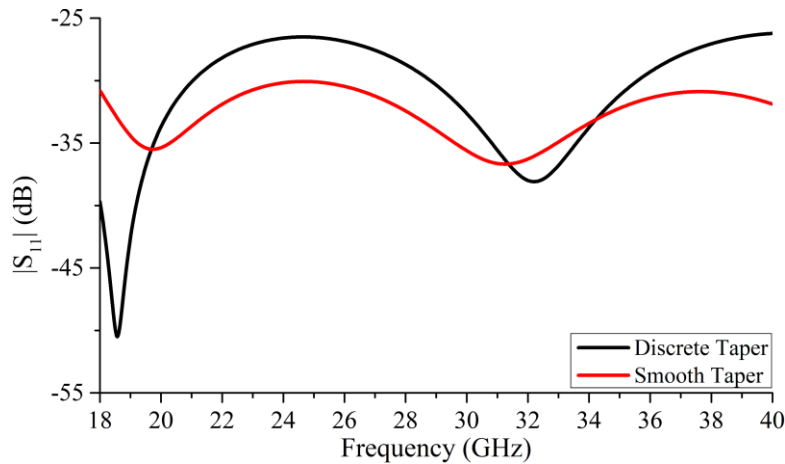


Figure 6.18. $|S_{11}|$ performance of 13-section discrete and smooth wideband Klopfenstein tapered feedline.

6.3.2 Geometry of Dual Bruce Array Antenna

The geometry of 1×2 printed Dual Bruce array antenna (D-BAA), with improved unit-cell, is shown in **Figure 6.19**. Each row of BAA is connected to either end of the two-way Klopfenstein feedline divider. The spacing between the two rows of BAA, w_x , is

5.39 mm. As with the BAA discussed in the Section 6.2, 50 Ω resistors are connected to each row of BAA for termination to ensure there are no reflections. It is noteworthy that the width of the overall structure has remained unchanged with the addition of another row, i.e., 13.50 mm, as the Southwest Endlaunch connector itself is 12.70 mm wide therefore the width of the substrate had to be kept wider than the connector's punch screws in **Figure 6.11**. The overall length of the structure has increased by 3.0 mm, and is now 73.0 mm.

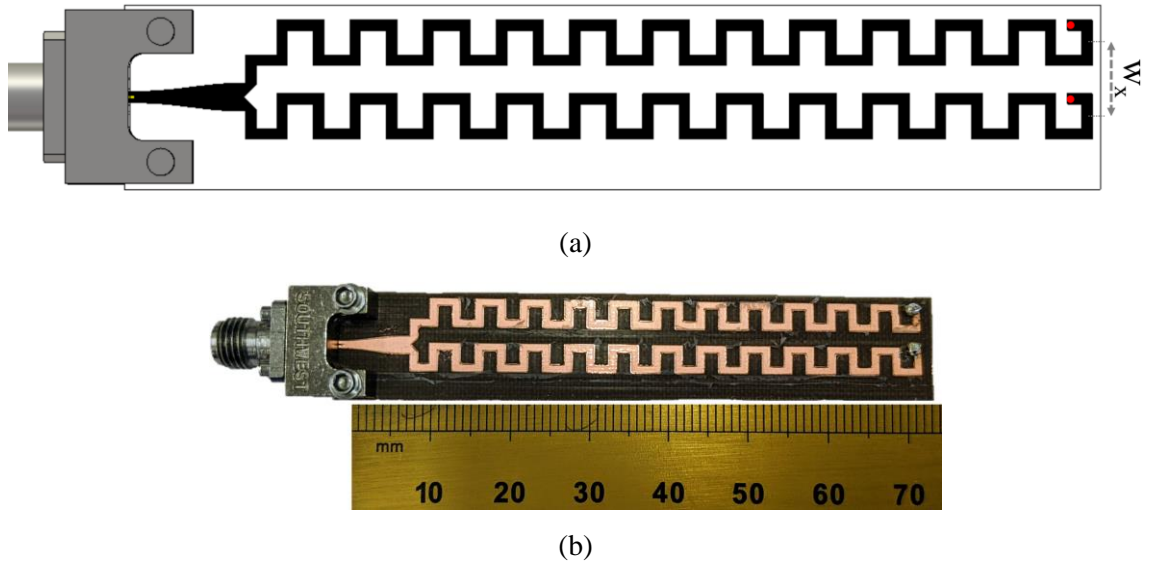


Figure 6.19. D-BAA-LWA with tapered Klopfenstein feed two-way divider based on improved unit-cell (a) Geometry (b) Prototype.

6.3.3 Results and Discussion

6.3.3.1 Impedance Bandwidth

The simulated $|S_{11}|$ plot is shown in **Figure 6.20**. The antenna array has a wide bandwidth with $|S_{11}| \leq -10$ dB below 18.0 GHz to 38.63 GHz with the OSB matched in this region. The measured response of the $|S_{11}|$ shows good agreement with the simulated structure.

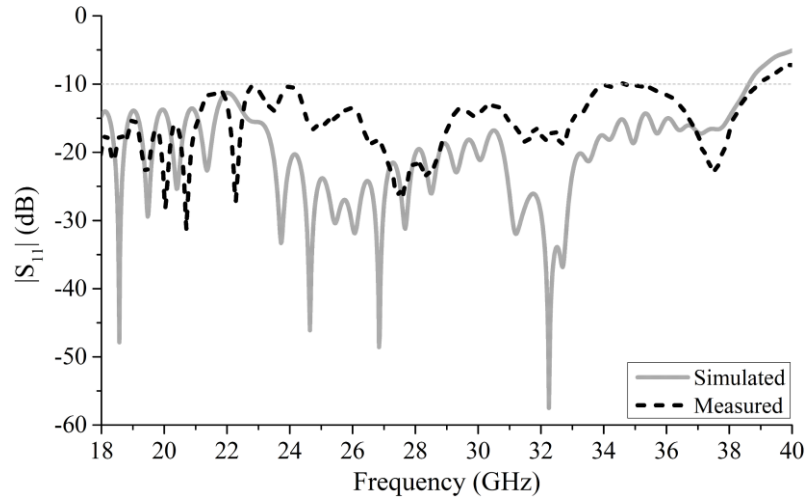


Figure 6.20. Simulated and measured $|S_{11}|$ plot of D-BAA with improved unit-cell.

6.3.3.2 Half Power BeamWidth and Efficiency

The HPBW and the radiation efficiency of the D-BAA are presented in **Figure 6.21**. The HPBW pattern in yz-plane remains almost unchanged throughout the operating frequency band when compared with the standalone BAA in **Figure 6.16**. However, in the xz-plane, the HPBW has become narrower which is a typical feature of linear arrays. The radiation efficiency of the D-BAA is between 32% – 88%.

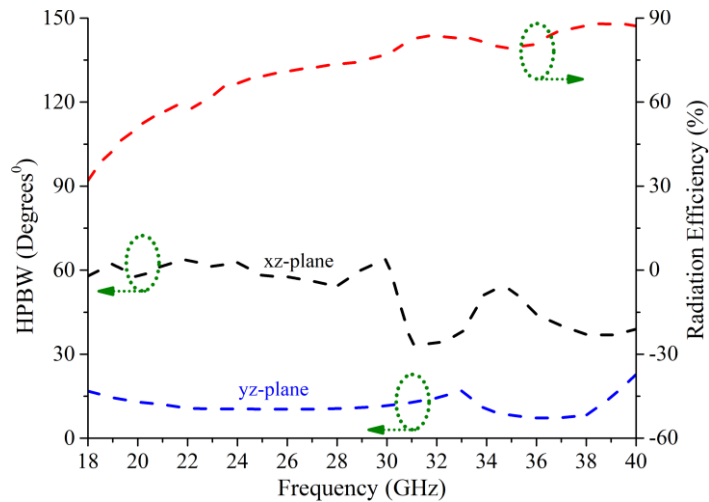


Figure 6.21. Simulated HPBW and Radiation Efficiency of BAA and D-BAA.

6.3.3.3 Scanning Range

The scanning ranges of the D-BAA are shown in **Figure 6.22**. Similar SLL threshold level as BAA is used for D-BAA and the scanning space in the backward endfire is presented in **Figure 6.22(a)**. The antenna scans the space from -38° and the realized gain of the antenna increases progressively between 18.0 GHz to 22.50 GHz. **Figure 6.22(b)** shows scanning in the forward quadrant from broadside to endfire region. Due to the OSB mitigation at broadside, the realized gain between 22.50 GHz and 30.70 GHz the antenna scans from broadside to 54° with peak realized gain of 16.44 dBi. The SLL level at 30.70 GHz is still less than -10 dB but the realized gain experiences a drop due to rise in the back lobe as the scanning beam approaches forward endfire. The realized gain magnitude of the main and back lobes become equal at 33.13 GHz with angular separation of 111° after which the roles of main and back lobes are reversed. **Figure 6.22(c)** shows the second scanning range of the printed D-BAA. The expansion in the operating frequency range allows a wider second scanning range and the antenna scans the space from -32° and -5° between 34.90 GHz to 38.63 GHz.

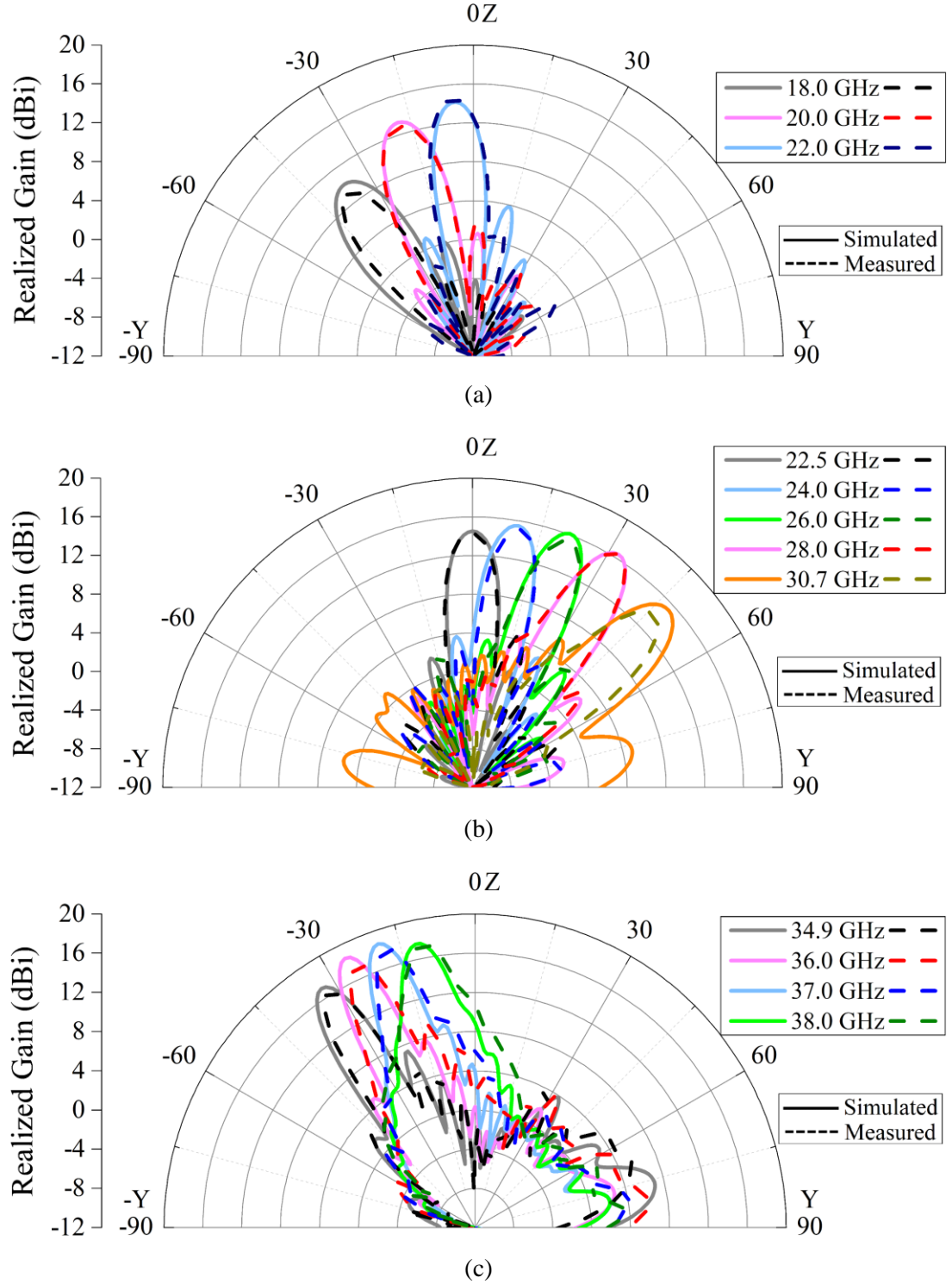


Figure 6.22. Proposed quasi-periodic D-BAA with improved unit-cell dimensions showing simulated and measured (a) 1st scanning range in backward quadrant (b) 1st scanning range in forward quadrant and (c) 2nd scanning range after role reversal of main and back lobe.

6.4 Modified Bruce Array Antenna with Semi-Circular and Bowtie Elements

6.4.1 Unit-Cell Configuration and Antenna Geometry

The configuration of the unit-cell of modified printed BAA is shown in **Figure 6.23**. The vertical and horizontal segments of the meander-line BAA antenna, shown in **Figure 6.1**, are replaced with bowtie and semi-circular elements, respectively. Either ends of the bowtie have the same width as of the semi-circular segment, i.e., w_c . According to the BAA, the meandered segments' lengths are approximately $\lambda/4$ but, in the mm-wave region, this corresponds to a very small size which gives rise to coupling between the vertical segments therefore these lengths are varied however, the length, l_v , and diameter, l_c , of the unit-cell are kept same. The period of the unit-cell, p_{unit} , is defined by $2 \times (l_c - w_c)$.

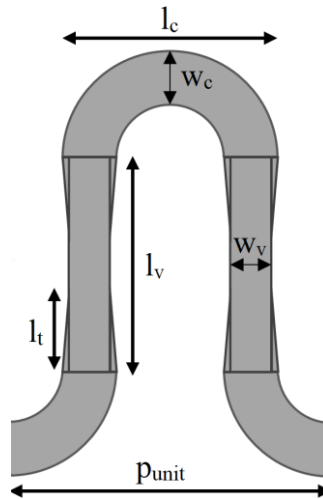
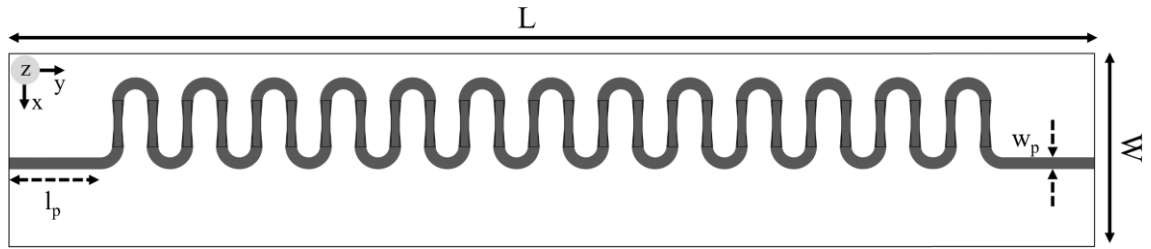
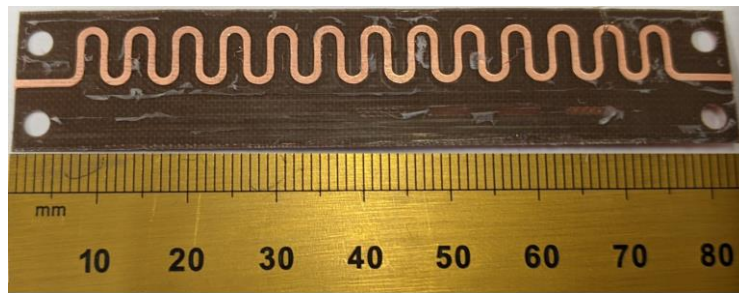


Figure 6.23. Geometry of the modified BAA unit-cell with vertical bowtie and horizontal semi-circular segments printed on a 0.254 mm thick grounded Arlon DiClad 880.

The geometry of the periodic modified BAA antenna, with vertical bowtie and horizontal semi-circular segments, is presented in **Figure 6.24(a)**. 13 unit-cell elements, presented in **Figure 6.23**, are connected in series for simulation and prototyping of the structure [180]. The periodic modulation of the geometry assists with radiation along the length of the antenna. The structure is fed using a transmission line and the last unit-cell element is terminated using a similar transmission line and another $50\ \Omega$ port that acts like a resistor to avoid reflections. Arlon DiClad 880 substrate, with thickness of 0.254 mm, $\epsilon_r = 2.2$ and $\tan \delta = 0.0009$, is used to fabricate the prototype presented in **Figure 6.24(b)**. **Table 6.3** shows the parameters associated with the unit-cell, presented in **Figure 6.23**, as well as the subsequent antenna configuration based on the unit-cell.



(a)



(b)

Figure 6.24. Top view of the proposed periodic 13 unit-cell antenna fabricated on 0.254 mm thick grounded Arlon DiClad 880 substrate (a) Geometry (b) Prototype.

Parameter	Symbol	Size (mm)
Length of antenna	L	83.60
Width of antenna	W	18.0
Diameter of semi-circular element	l_c	3.50
Length of vertical element	l_v	3.50
Perpendicular length of Bowtie segment	l_t	1.68
Width of semi-circular element	w_c	0.76
Width of vertical element	w_v	0.65
Period of unit-cell	p_{unit}	5.48
Length of transmission line	l_p	83.60
Width of transmission line	w_p	0.76

Table 6.3. Parametric details of antenna with semi-circular and bowtie elements unit-cell.

6.4.2 Parametric Analysis

6.4.2.1 Effect of Simultaneously Varying l_c and l_v without Bowtie Segment

Figure 6.25 shows the effects on $|S_{11}|$, for the structure with 13 unit-cell elements presented in **Figure 6.24**, by simultaneously varying l_v and l_c with $w_v = 0.76$ mm, without the vertical bowtie element. The multiplying factor of the wire BAA's $\lambda/4$ is increased to avoid unwanted resonances in the mm wave region and varied from $1.69 \times \lambda/4$ to $1.89 \times \lambda/4$ (3.30 mm to 3.70 mm). With this configuration, mismatching is observed around the broadside frequencies for which $|S_{11}| > -10$ dB which is the indication of presence of OSB and an increase in l_v and l_c by 0.1 mm tunes down the OSB mismatched region by approximately 1 GHz. The $|S_{11}|$ above and below the OSB, between 20 GHz and 40 GHz, remains less than -10 dB.

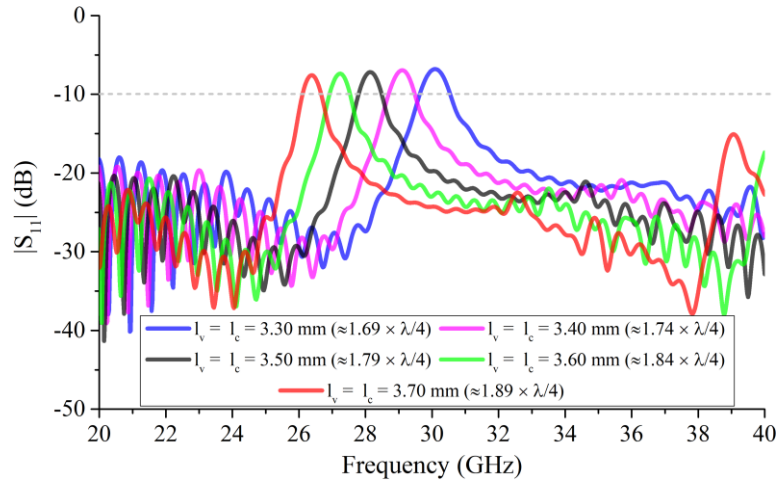


Figure 6.25. Effect of varying length, l_v , and diameter, l_c , simultaneously of 13 unit-cell element periodic structure with $w_v = 0.76$ mm unit-cell segments on $|S_{11}|$.

6.4.2.2 Effect of Varying Bowtie Segment's parameters w_v and l_t

The effect of parameters associated with the vertical bowtie segments, w_v and l_t , of the 13 unit-cell structure, on $|S_{11}|$, is shown in **Figure 6.26**. The other parameters, presented in **Table 6.3**, remain unchanged. A noticeable improvement in impedance matching, around the OSB region, is observed as the width, w_v , is increased from 0.50 mm to 0.60 mm, with

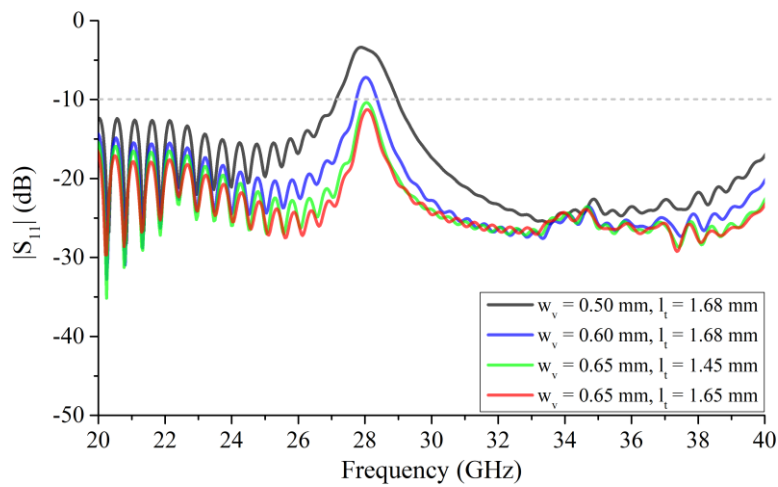


Figure 6.26. Effect of varying vertical bowtie segment parameters, w_v and l_t , of 13 unit-cell element periodic structure independently on $|S_{11}|$ while the other parameters remain constant.

l_t fixed at 1.68 mm, in which $|S_{11}|$ improves from -7.24 dB to -3.54 dB at 28.0 GHz. In the other case, where w_v is kept constant at 0.65 mm, the variation in l_t from 1.45 mm to 1.65 mm improves the impedance matching significantly without any upward or downward tuning of frequency.

6.4.2.3 Effect of Varying l_v and l_c independently with Bowtie Segment

The effect of varying l_v , with fixed $w_v = 0.65$ mm bowtie vertical unit-cell segment, on $|S_{11}|$ is shown in **Figure 6.27(a)**. The frequency tunes down by approximately 1.15 GHz and the impedance matching deteriorates when l_v is increased by 0.20 mm, between 3.40 mm and 3.60 mm, and l_c is kept constant at 3.50 mm. A downward shift in frequency of 0.70 GHz is observed when l_v is fixed at 3.50 mm and l_c is increased from 3.40 mm to 3.60 mm with minute effect on impedance matching, shown in **Figure 6.27(b)**.

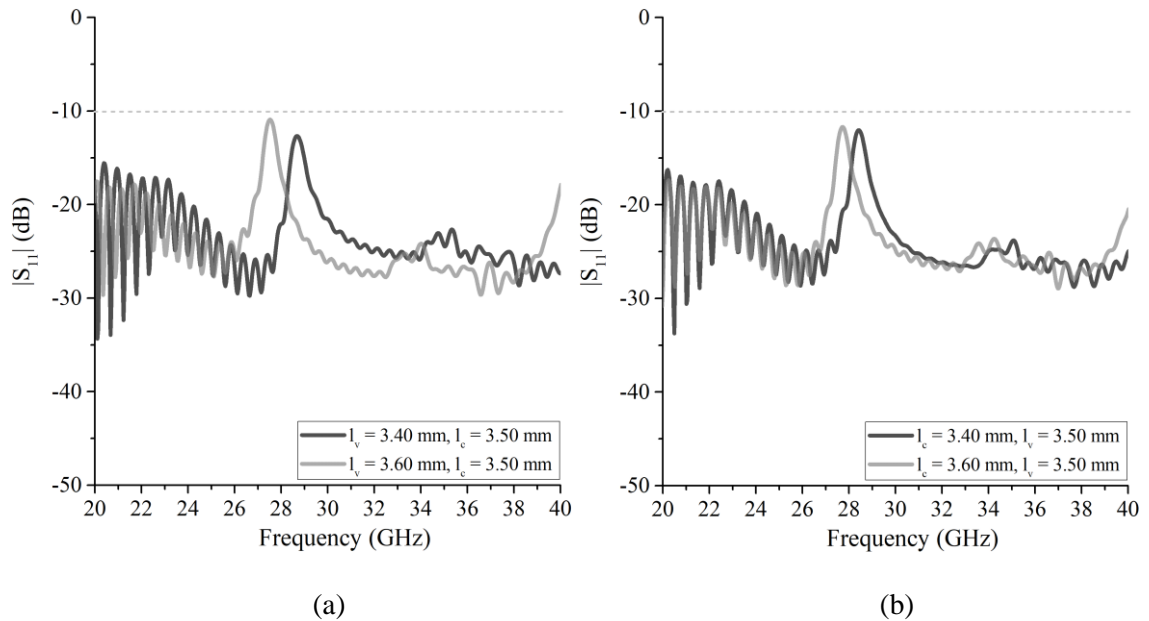


Figure 6.27. Effect of independently varying lengths of 13 unit-cell element periodic structure with fixed $w_v = 0.65$ mm bowtie segments on $|S_{11}|$ (a) Varying l_v with fixed $l_c = 3.50$ mm (b) Varying l_c with fixed $l_v = 3.50$ mm.

6.4.2.4 Realized Gain without Bowtie Element

Figure 6.28 shows the simulated realized gain of the 13 unit-cell antenna structure without vertical bowtie element, between 22 GHz and 38 GHz, with $l_v = l_c = 3.50$ mm and $w_v = 0.76$ mm. The gain rises gradually between 23.0 GHz and 26.0 GHz and, while still under 12.0 dBi at 26.0 GHz, a sharp gain drop is observed around 28.0 GHz. The realized gain around 28.0 GHz is considerably less than the realized gain in the rest of the forward endfire region. This is consistent with the OSB region, identified in **Figure 6.25**, where $|S_{11}| > -10$ dB.

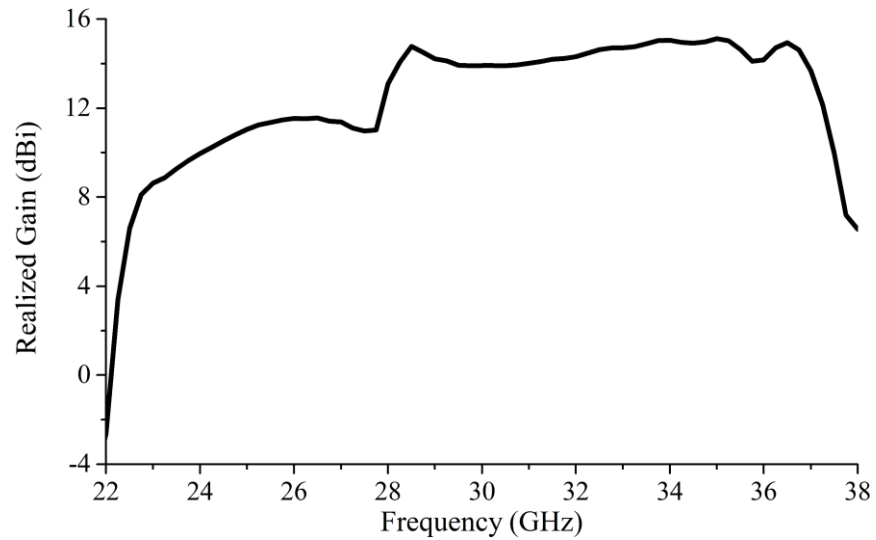


Figure 6.28. Simulated realized gain of 1-D periodic BAA-LWA with $l_v = l_c = 3.50$ mm and $w_v = 0.76$ mm unit-cell showing gain degradation around 28.0 GHz.

6.4.3 Results and Discussion

6.4.3.1 Impedance Bandwidth

Figure 6.29 shows the simulated and measured response of the $|S_{11}|$ of the 13 unit-cell structure with bowtie vertical segments, shown in **Figure 6.24** and parameters presented in **Table 6.3**. The mismatched OSB frequency range, for when l_v and l_c is 3.50 mm ($\approx 1.79 \times \lambda/4$) and $w_v = 0.76$ mm presented in **Figure 6.25**, improves without any frequency tuning resulting in the mitigation of the OSB. The $|S_{11}|$, at 28.0 GHz, improves to -12.01 dB with the vertical bowtie element compared to -7.73 dB without the bowtie element. With the bowtie element, the $|S_{11}| \leq -10$ dB from below 22.0 GHz and above 40.0 GHz with fractional bandwidth of more than 67%. The difference in simulated and measured $|S_{11}|$ is because the contour router does not smoothen out the curvatures of semi-circular and bowtie-elements. Nevertheless, the bandwidth remains unaltered, and the broadside frequency does not shift.

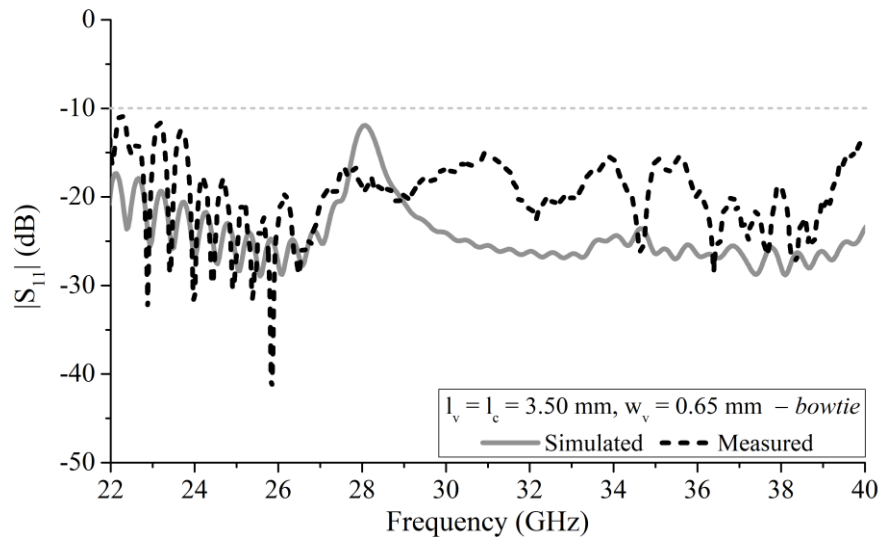


Figure 6.29. Simulated and measured $|S_{11}|$ of 13 unit-cell element periodic structure with bowtie vertical unit-cell segments.

6.4.3.2 Realized Gain

Figure 6.30 shows the realized gain plot of the antenna structure with the modified bow-tie unit-cell shown in **Figure 6.24**. The sharp decline in realized gain around 28.0 GHz region, shown in **Figure 6.28**, has considerably improved with this arrangement using the parameters presented in **Table 6.3**. The gain profile gradually increases around 23.0 GHz, and onwards, with peak realized gain of 15.30 dBi at 35.0 GHz.

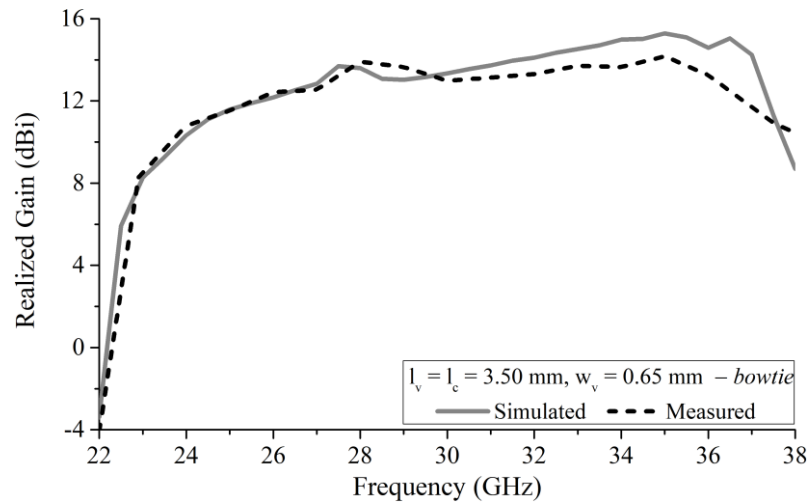
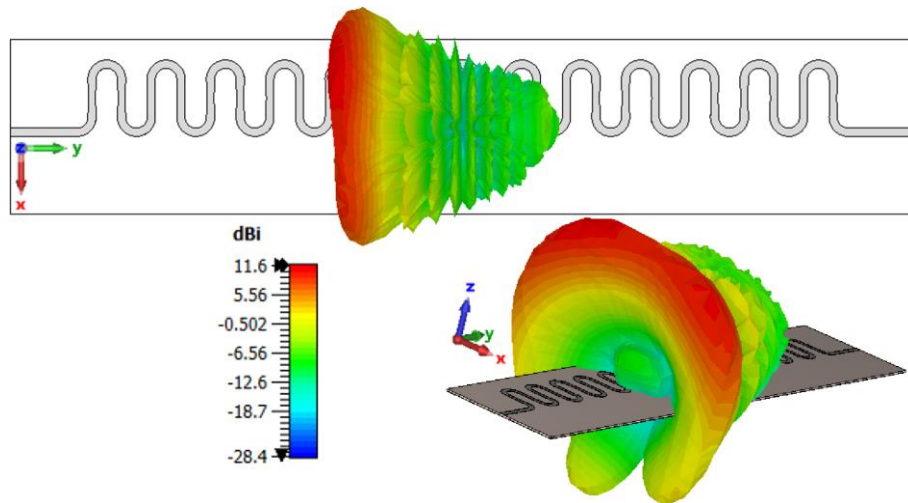


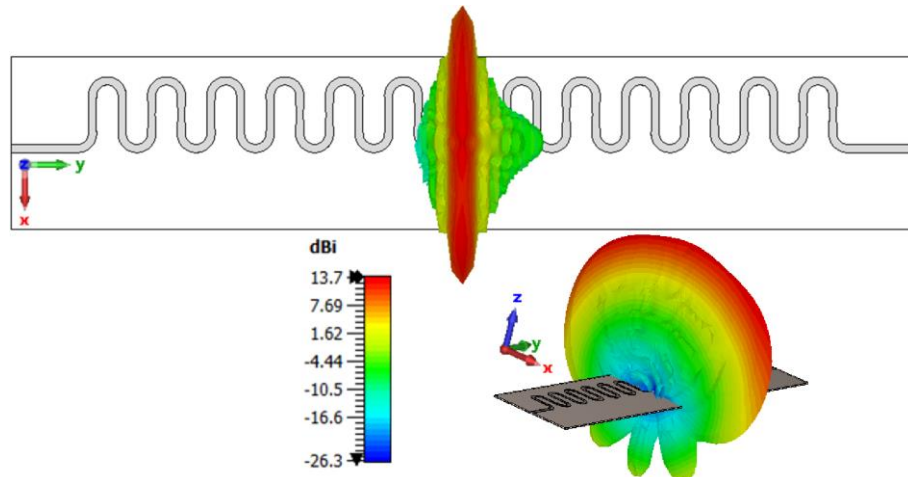
Figure 6.30. Simulated and measured realized gain comparison of 13 unit-cell element periodic structure with $w_v = 0.76$ mm and modified bowtie vertical unit-cell segments.

6.4.3.3 Radiation Characteristics and Scanning Range

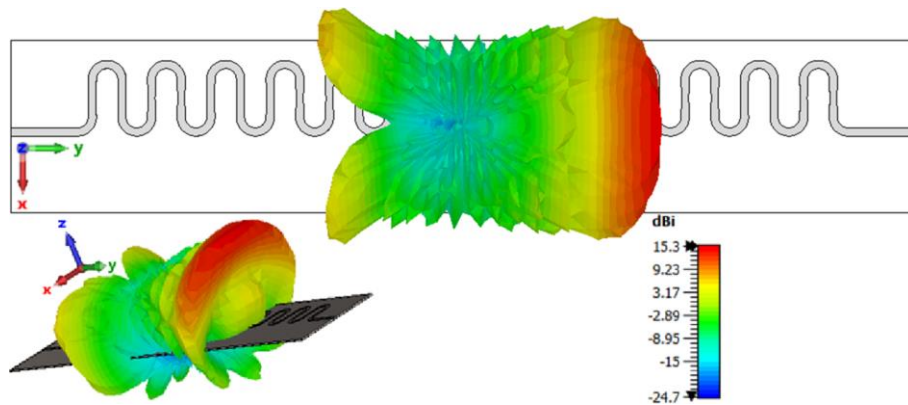
The 3D radiation patterns for the simulation of the 13-element structure, with bowtie and semi-circular unit-cell, are presented for backward endfire, broadside and forward endfire regions in **Figure 6.31(a)**, **(b)** and **(c)**, respectively. The patterns, at 24.0 GHz, 28.0 GHz and 35.0 GHz, show a fan-beam scanning with increase in frequency with radiation angles of -42° , 0° and 56° , respectively. At 28 GHz, when the beam is at 0° in the yz-plane, the HBPW in the xz-plane is 125.5° as shown in the side view 3D pattern in **Figure 6.31(b)**.



(a)



(b)



(c)

Figure 6.31. 3D radiation pattern visualising scanning in top and side view at (a) 24.0 GHz (b) 28.0 GHz (c) 35.0 GHz.

The scanning range of the proposed antenna is presented in **Figure 6.32**. **Figure 6.32(a)** shows the scanning range from backward endfire approaching towards the broadside. The antenna scans from -64° at 22.87 GHz. **Figure 6.32(b)** shows the scanning range from the broadside to the forward endfire direction. The antenna scans seamlessly through the broadside, due to the mitigation of OSB, until 76° i.e., 37.0 GHz.

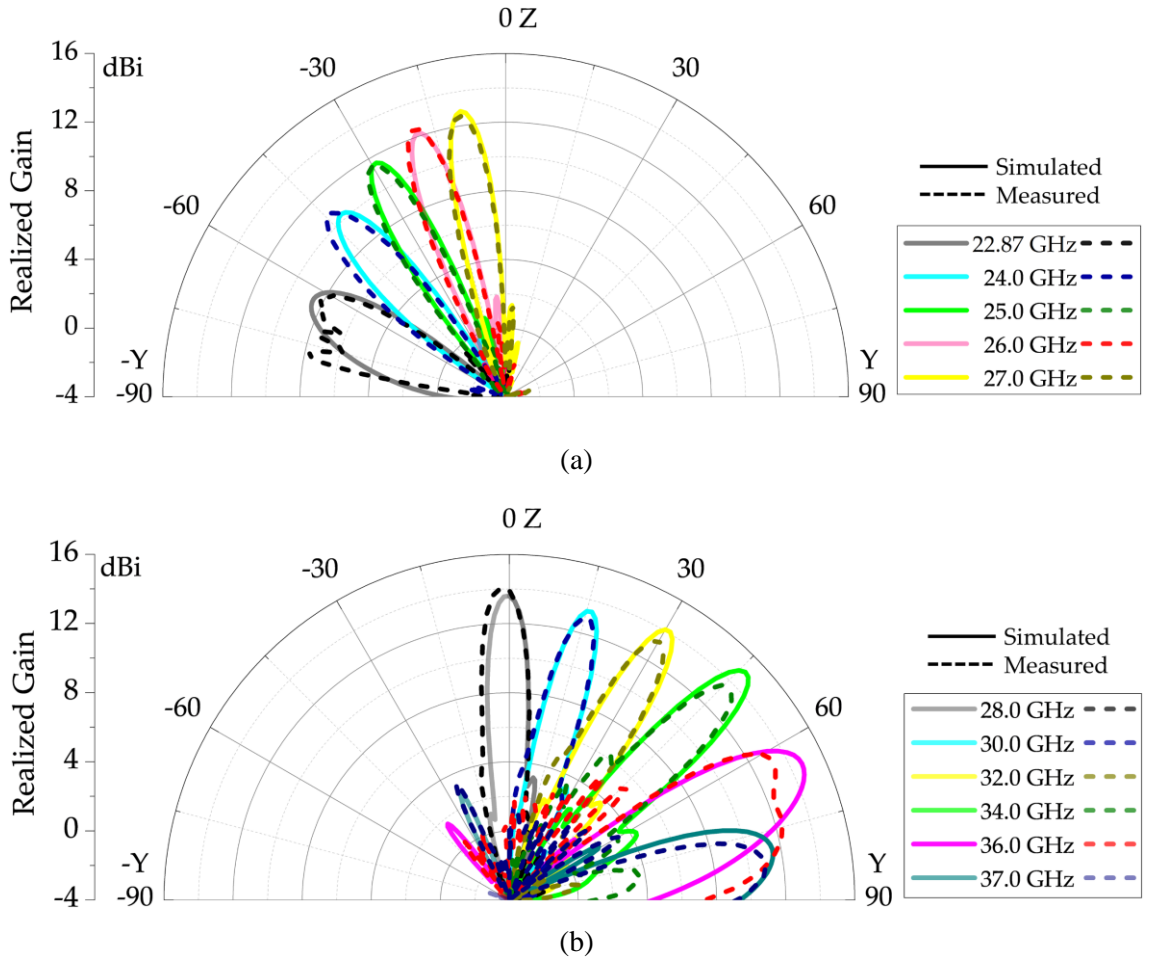


Figure 6.32. Scanning range of the proposed 1-D periodic modified BAA-LWA with bowtie and semi-circular unit-cell (a) backward quadrant and (b) forward quadrant.

6.4.3.4 Sidelobe Level and Main Beam Direction

Figure 6.33 show the SLL and main beam direction, in the yz-plane, of the proposed antenna. From **Figure 6.29** it can be seen that the antenna has wide bandwidth below 22.87 GHz and above 37.0 GHz, but these frequencies are not considered as part of the scanning range in **Figure 6.32** because an SLL threshold of -10 dB is maintained to efficiently define the scanning region shown in **Figure 6.33(a)**. As the mainlobe of the scanning range approaches forward endfire after 76° , shown in **Figure 6.33(b)** the rise in the antenna's backlobe and the increase in SLL makes it unsuitable to scan in a single direction as efficient as the rest of the considered bandwidth.

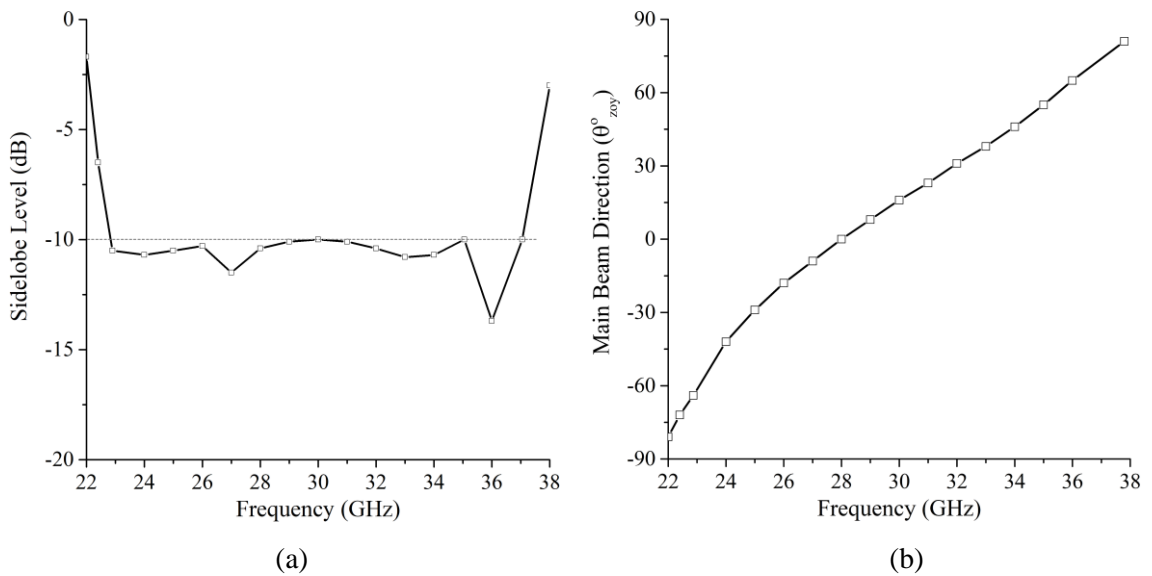


Figure 6.33. (a) Sidelobe Level and (b) Main beam direction in the yz-plane of the proposed LWA.

6.4.3.5 Efficiency and Half Power BeamWidth

Figure 6.34(a) shows the radiation efficiency of the proposed antenna array. The antenna has more than 60% radiation efficiency throughout the scanning range and between

25.0 GHz and 37.0 GHz, the efficiency is more than 80%. The HPBW in yz-plane, across the entire scanning range is shown in **Figure 6.34(b)**. It can be seen that the antenna has a narrow radiation beam in the scanning range which can be classified as fan-beam radiation pattern but broadens with the rise of sidelobe level in both backward and forward endfire direction frequencies i.e., below 24 GHz and above 35 GHz.

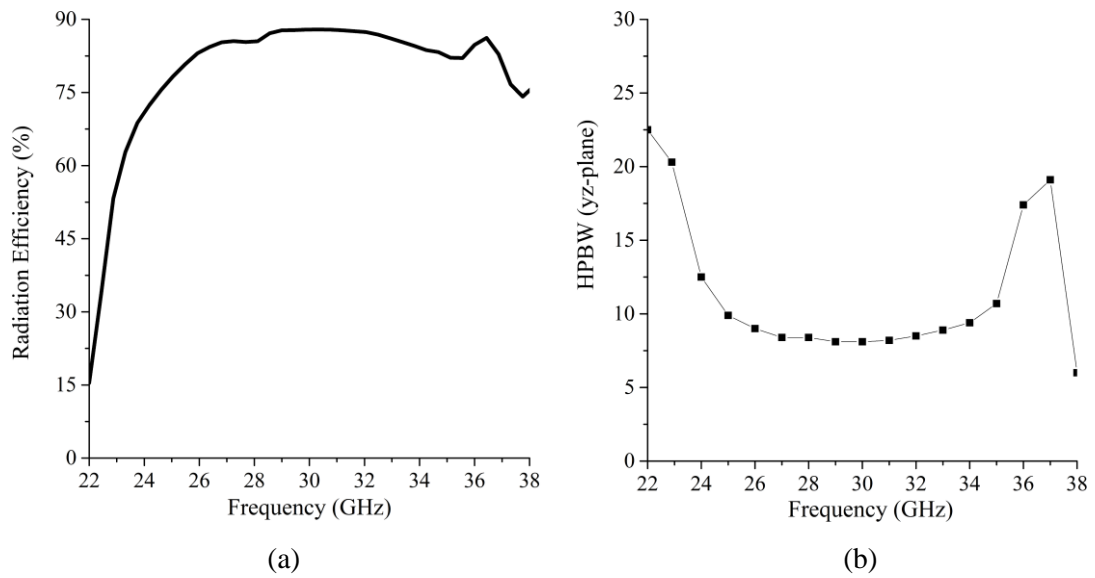


Figure 6.34. Simulated plots of LWA (a) Radiation Efficiency and (b) HPBW in y-z plane.

6.5 Comparison with Existing Literature

A comparison between the proposed antennas and the antennas with similar frequency scanning characteristics, found in literature, is presented in **Table 6.4**. Several methodologies have been proposed in the literature on different design types to widen the scanning range and suppress or mitigate the effects of OSB in different frequency bands. It can be seen that in terms of the scanning range, the antennas proposed in Sections 6.2 and 6.3 are the only antennas to have wide enough bandwidth to support two distinct scanning

ranges at different frequencies. In several articles, the SLL scanning threshold is not mentioned but all the proposed antennas have better SLL for the scanning range than [181] and same as that of [166] and [70]. In [182], only the SLL at broadside is mentioned. Amongst other features, the proposed antennas have high peak realized gain than [152], [181]–[183]. The waveguide CTS structure in [149] has high gain and better SLL threshold but the structure is relatively larger in size, with overall dimensions of $133 \times 93 \times 21 \text{ mm}^3$, having narrower scanning range and smaller fractional bandwidth. Furthermore, the proposed antennas have the least fabrication requirement, along with the antenna presented in [155], [166], [182] compared to others especially the SIW and CTS structures [149], [150], [168], [184], [185] that require multiple layers, drilling holes and have complicated fabrication process. The proposed antenna with vertical bowtie and horizontal semi-circular element, presented in Section 6.4, has better scanning range than the first continuous scanning range of BAA and D-BAA presented in Sections 6.2 and 6.3, respectively and all the antennas presented in **Table 6.4** except [168] but, although it mentions continuous scanning range between 144° to 41° for 4.40 GHz to 8.80 GHz, the OSB is not suppressed and is clearly evident between 5.30 GHz to 6.20 GHz. If not for the $\text{SLL} \leq -10 \text{ dB}$ threshold maintained throughout this work, the proposed antennas may have had a wider scanning range due to the available bandwidth. The proposed antennas can be used for 28 GHz 5G and Ka-Band mm-wave imaging applications [37].

Ref	Antenna Type	Total Length (λ_0)	Bandwidth (GHz)	Realized Gain (dBi)	Scanning Range	SLL Threshold (dB)
[149]	WG-CTS	15.08	26.0 – 42.0	22.90 ~ 29.20	-56.2° ~ -2.2°	-12.6
[150]	Periodic SIW	11.12	13.20 – 15.60	14.10 (Peak)	-61° ~ 42°	N/A
[152]	Periodic SIW	≈ 5.80	9.0 – 14.0	14.89 (Peak)	-40° ~ 35°	
[153]	Half-mode SIW	≈ 9.30	13.50 – 16.50	10.0 (Peak)	-30° ~ 30°	-10
[155]	Periodic Microstrip	3.68	3.70 – 6.80	10.0 (Peak)	-55° ~ 63°	N/A
[159]	Multi-layered CRLH TL	11.58	20.0 – 30.0	10.0 ~ 14.0	-25° ~ 50°	
[166]	Periodic Microstrip	29.49	8.0 – 11.40	21.0 (Peak)	-25° ~ 10°	-10
[168]	*Periodic HW-MLWA	3.99	4.40 – 8.80	≈ 1.0 ~ 8.0	144° ~ 41°	N/A
[181]	Microstrip-slot stubs	2.65	2.40 – 2.60	≈ 9.0 (Peak)	4° ~ 31°	-6
[182]	Periodic Microstrip	7.48	20.0 – 29.0	12.20 (Peak)	-50° ~ 45°	-13 (broadside)
[183]	Metasurface WG slot	15.85	15.50 – 16.20	15.10 (Peak)	47° ~ 7°	N/A
[184]	SIW Planar	12.24	24.0 – 25.60	13.0 ~ 15.0	-30° ~ 30°	
[185]	CTS SIW	13.46	27.06 – 36.0	12.85 ~ 17.84	-43° ~ 3°	
[186]	Periodic CRE	N/A	13.0 – 19.45	≈ 12.0 ~ 14.0	-45° ~ 35°	
<i>This Work</i>	<i>Microstrip BAA (Section 6.2)</i>	6.44	18.0 – 37.20	8.0 ~ 13.30	-38° ~ 55°	-10
				15.10 ~ 16.56	-31° ~ -17°	
	<i>Microstrip D-BAA (Section 6.3)</i>	6.80	18.0 – 38.63	10.60 ~ 16.44	-38° ~ 54°	
				16.20 ~ 18.61	-32° ~ -5°	
	<i>Bowtie, semi-circular BAA (Section 6.4)</i>	7.80	22.87 – 37.0	8.57 ~ 15.30	-64° ~ 76°	

CRE – Complimentary radiation elements; **TL** – Transmission line; **HW-MLWA** – Half width microstrip LWA; **WG** – Waveguide; **CTS** – Continuous transverse stub; **N/A** – Not Available; * OSB from 5.30 GHz to 6.20 GHz.

Table 6.4. Performance comparison between proposed LWAs and LWAs in literature.

6.6 Summary

The transformation of a meandered wire BAA structure to printed edge-fed Leaky-wave BAA and their modifications for continuous scanning are presented in this chapter. The first variation introduces an 11 unit-cell BAA with unequal horizontal and vertical lengths and its 1×2 linear array, D-BAA, featuring two distinct scanning ranges and a dual beam region. The unit-cell of the antenna, initially designed in accordance with wire BAA's theory with equal horizontal and vertical lengths, is optimized to mitigate the effects of open-stopband at broadside enabling seamless scanning from backward to forward end-fire. The proposed D-BAA, fed using Klopfenstein tapered feed, is compact in size and offers two wide scanning ranges between -38° to 54° and between -32° to -5° with peak gain of 18.61 dBi. The second variation of the antenna aims at one but wider backward to forward endfire scanning range. The horizontal and vertical segments of the meandered unit-cell are replaced with semi-circular and bowtie segments, respectively, of which, the latter assists in mitigation of the open-stopband at broadside. The length and diameter of both vertical and horizontal segments, respectively, are kept equal at 3.50 mm. The proposed antenna has wide operational bandwidth from below 20.0 GHz to above 40.0 GHz however an SLL threshold of -10 dB is enforced to define efficient scanning range between 22.87 GHz and 37.0 GHz. The 13 unit-cell periodic antenna has a compact size, offers scanning range between -64° to 76° and has peak gain of 15.30 dBi.

Chapter 7

Conclusions and Future Work

7.1 Conclusions

With the increase in projected number of wireless technology and mobile application consumers, the large and less exploited mm-wave frequency region is anticipated to be the future of wireless applications. Although the availability of such a vast bandwidth is attractive, it also poses design challenges for antenna engineers with constraints pertaining to high frequencies. This research discussed the transformation and modification of the antenna structures, used for lower frequency applications, to explore and utilize performance for compact printed mm-wave applications with high gain, multi-band and wideband characteristics.

Rogers RT/duroid 5880 is one of the most commonly used and popular choice substrates for mm-wave applications because it is low profile, has low electrical losses and is suitable for atmospheric conditions with high moisture. In this research, wherever possible, Rogers RT/duroid 5880 substrate, with thickness of 0.254 mm, has been used for simulation and modelling of the antennas. A 4×2 element microstrip patch array antenna with rear-fed arrangement, having 16.10 dBi measured broadside gain for upper 26 GHz wireless communication applications, has been presented in Chapter 3. Although sometimes categorized as a rigid material in comparison to other flexible substrates, Rogers

RT/duroid 5880 is susceptible to bending or deformation during placement of the substrate for fabrication on the LPKF machine, antenna substrate cut-out, installation of connector, during pattern measurement setup with tension of the cable connected to the antenna or just a hard hand grip. The observation of the uniform bending tolerance of the edge-fed antenna shows that when curved in convex direction, the frequency tuned upwards by over 700 MHz with curving as little as 3° which, with connector, is invisible to an unaided eye on a planar surface and the performance deteriorated after 10° bend with increased mismatching and reduced gain therefore caution should be exercised if the desired fabricated antenna is planar.

Conventionally, the microstrip patch array antennas have limited bandwidth. In order to cater the objective of multiband and wideband applications in the mm-wave region, a quasi-rhombic, dual-band planar counterpart of wire grid array antenna has been presented in Chapter 4. The grid array antenna has two operating frequency regions in the upper 26 GHz region with single and dual-beam radiation patterns. The comparison with patch antenna array, of similar footprint, shows that the grid array, with its simplistic structure, has 1.5 percentage points more fractional bandwidth and 5° wider beamwidth in the elevation plane operating in two bands in close proximity.

The Bruce array antenna is one of the most, if not the most, understudied antennas in history. For the first time, an approach to transform and modify conventional wire Bruce array antenna to planar technology, for 5G and mm-wave applications, has been presented in Chapter 5. The resultant, 16 radiating element, planar geometry was an easy to fabricate, meandered structure with tri-band mm-wave operation. For a compact and minimalistic structure, the antenna accommodated the multiband demands for the mm-

wave wireless communication applications having high gain, broadside fan-beam radiation pattern, at 28 GHz and dual-beam radiation patterns in 31 GHz and 33-34 GHz range enabling radiation diversity in scenarios which are not conducive for wireless communication such as underground and narrow passages.

The multiband antennas introduced in the research can be used for fixed frequency and fixed beam applications however, high bandwidth, with high gain, is required for mm-wave frequency scanning systems to achieve high resolution. In Chapter 6, the simplistic concept of planar Bruce array antenna has been extended to edge-fed leaky-wave structure in which the first iteration mitigates the open-stopband problem of periodic structures, using optimization of lengths, without any complex circuitry. The antenna resolves the bandwidth limitation and supports two frequency scanning ranges in K-Band and Ka-Band with the first range scanning seamlessly from backward to forward endfire directions and the second range in the backward endfire direction. Linear arrays have always attracted huge interest from antenna engineers which increase the gain and directivity and aid in the collimation of radiation patterns from individual elements but, depending on the design, often these array antennas end up being bulky. The deployment of a two-way Klopfenstein tapered feed divider for Dual Bruce array, increased the gain with only 3.0 mm increase in the size of antenna. In another variation, the Bruce array's high gain, frequency scanning potential was analyzed further by replacing the horizontal and vertical segments with semi-circular and bowtie segments, respectively. The bowtie element assisted in the mitigation of the open-stopband with the antenna having a wide seamless scanning, with wide bandwidth, for mm-wave scanning applications.

7.2 Future Work

With the continuously transitioning systems and applications from lower frequencies to mm-wave and 5G spectrum, it is imperative for engineers to seek new methodologies to design efficient, high bandwidth and highly efficient antennas. While the demands of most applications and potential of mm-wave is speculative, at this moment, evolution is inevitable and, therefore, there is a need to design cost-efficient and compact antennas for future wireless communications.

The work presented in this thesis has primarily been carried out using planar structures. However, several applications, such as wearable gadgets, in the future will demand the deployment of the antenna on uneven and non-planar surfaces. The antenna structures can be developed and explored with flexible materials, such as LCP substrates, to tap their potential for conformal antenna applications. Transparent antenna structures can be explored to form solutions with high visibility in glass panels, such as windows etc, for 5G vehicular communications and other conformal applications based on thin-film technologies while maintaining good radiation performance.

The work presented on Bruce array antennas can be further expanded by using other divider transitions, instead of Klopfenstein, such as SIW. The simplistic structure has limited control because of fewer variables. To further explore its potential, phase scanning ability of beamforming networks, such as Butler matrix, can be combined with frequency scanning feature in linear array of Bruce array. Techniques such as corrugation can be deployed to miniaturize the design and have more influence on individual bands in case of the rear-fed antenna.

Integrated antenna-in-packaging has been used for several devices. The effects of packaging with commonly used materials should be analysed to compare performance between Bruce array and other conventional antennas. In the future, the effects on human body should be performed using voxel-based models such as Gustav or Hugo.

The potential of 5G mm-wave is yet to be fully realized and although it is too early to predict the requirement and potential of beyond 5G systems, and its standardization being an open-research question, the scientific community has already started to envision what should be expected from 6G communication systems. Along with Terahertz (THz) and sub-THz bands, mm-wave band is also expected to be used in 6G communications for high data-rate transfers, up to 100 Gbps, for short range device-to-device communications therefore innovative and efficient antenna design techniques will be required to accommodate the upcoming applications.

Bibliography

- [1] D. Prinima and D. J. Pruthi, “Evolution of Mobile Communication Network: from 1G to 5G,” *Int. J. Innov. Res. Comput. Commun. Eng.*, vol. 4, no. 4, p. 224, 2016.
- [2] L. Guevara and F. Auat Cheein, “The Role of 5G Technologies: Challenges in Smart Cities and Intelligent Transportation Systems,” *Sustainability*, vol. 12, no. 16, 2020.
- [3] “World Telecommunication Indicators Database,” International Telecommunication Union (ITU), 2003. Accessed: Jan. 30, 2021. [Online]. Available: [https://www.itu.int/itudoc/gs/subscirc/itu-d/\(191-03\).html](https://www.itu.int/itudoc/gs/subscirc/itu-d/(191-03).html).
- [4] “Measuring digital development: Facts and figures 2020,” International Telecommunication Union (ITU), 2020. Accessed: Feb. 26, 2021. [Online]. Available: <https://www.itu.int/en/ITU-D/Statistics/Pages/facts/default.aspx>.
- [5] T. S. Rappaport *et al.*, “Millimeter wave mobile communications for 5G cellular: It will work!,” *IEEE Access*, vol. 1, pp. 335–349, 2013.
- [6] T. K. Sawanobori, “The Next Generation of Wireless: 5G Leadership in the US Washington,” *DC, USA CTIA*, 2016.
- [7] “Ericsson Mobility Report 2019,” Ericsson, 2019. Accessed: Feb. 04, 2021. [Online]. Available: <https://www.ericsson.com/4acd7e/assets/local/mobility-report/documents/2019/emr-november-2019.pdf>.
- [8] “Cisco visual networking index: global mobile data traffic forecast update, 2017–2022,” Cisco, 2019. Accessed: Jan. 30, 2021. [Online]. Available:

- <https://s3.amazonaws.com/media.mediapost.com/uploads/CiscoForecast.pdf>.
- [9] “Ericsson Mobility Report 2020,” Ericsson, 2020. Accessed: Feb. 04, 2021. [Online]. Available: <https://www.ericsson.com/4adc87/assets/local/mobility-report/documents/2020/november-2020-ericsson-mobility-report.pdf>.
- [10] “Spectrum for 4G and 5G,” Qualcomm Technologies, San Diego, CA, USA, Dec. 2020. Accessed: Feb. 25, 2021. [Online]. Available: <https://www.qualcomm.com/media/documents/files/spectrum-for-4g-and-5g.pdf>.
- [11] N. Naderializadeh and A. S. Avestimehr, “ITLinQ: A new approach for spectrum sharing in device-to-device communication systems,” *IEEE J. Sel. areas Commun.*, vol. 32, no. 6, pp. 1139–1151, 2014.
- [12] C.-H. Yu, K. Doppler, C. B. Ribeiro, and O. Tirkkonen, “Resource sharing optimization for device-to-device communication underlaying cellular networks,” *IEEE Trans. Wirel. Commun.*, vol. 10, no. 8, pp. 2752–2763, 2011.
- [13] “Report of the unlicensed devices and experimental licenses working group,” 2002. Accessed: Feb. 17, 2021. [Online]. Available: <https://transition.fcc.gov/sptf/files/E&UWGFinalReport.pdf>.
- [14] Y. Banday, G. M. Rather, and G. R. Begh, “Effect of atmospheric absorption on millimetre wave frequencies for 5G cellular networks,” *IET Commun.*, vol. 13, no. 3, pp. 265–270, 2018.
- [15] “IEEE Standard for Information technology--Telecommunications and information exchange between systems--Local and metropolitan area networks--Specific requirements-Part 11: Wireless LAN Medium Access Control (MAC) and Physical Layer (PHY) Specifications Am,” *IEEE Std 802.11ad-2012 (Amendment to IEEE Std 802.11-2012, as amended by IEEE Std 802.11ae-2012 and IEEE Std*

802.11aa-2012). pp. 1–628, 2012.

- [16] “IEEE Draft Standard for Information Technology-Telecommunications and Information Exchange Between Systems - Local and Metropolitan Area Networks-Specific Requirements Part 11: Wireless LAN Medium Access Control (MAC) and Physical Layer (PHY) Specificatio,” *IEEE P802.11ay/D7.0*, December 2020. pp. 1–784, 2020.
- [17] “WiGig® and the future of seamless connectivity,” WiGig®, 2013. Accessed: Feb. 17, 2021. [Online]. Available: https://www.wi-fi.org/system/files/WiGig_White_Paper_20130909.pdf.
- [18] “Deploying 5G NR mmWave to unleash the full 5G potential,” Qualcomm Technologies, San Diego, CA, USA, Nov. 2020. Accessed: Feb. 09, 2021. [Online]. Available: <https://www.qualcomm.com/media/documents/files/deploying-mmwave-to-unleash-5g-s-full-potential.pdf>.
- [19] T. S. Rappaport, R. W. Heath Jr, R. C. Daniels, and J. N. Murdock, *Millimeter wave wireless communications*. Pearson Education, 2015.
- [20] “America’s 5G Future.” Accessed: Feb. 23, 2021. [Online]. Available: <https://www.fcc.gov/5G>.
- [21] “Use of Spectrum Bands Above 24 GHz for Mobile Radio Services,” May 2019. Accessed: Feb. 23, 2021. [Online]. Available: <https://www.federalregister.gov/documents/2019/05/13/2019-09426/use-of-spectrum-bands-above-24-ghz-for-mobile-radio-services>.
- [22] “5G for Europe: An Action Plan,” European Commission, Brussels, Belgium, Sep. 2016. Accessed: Feb. 15, 2021. [Online]. Available:

- https://ec.europa.eu/newsroom/dae/document.cfm?doc_id=17131.
- [23] “Results of the 3.6 GHz Band Spectrum Award,” Comreg, Ireland, Jun. 2017. Accessed: Mar. 15, 2021. [Online]. Available: <https://www.comreg.ie/publication-download/results-3-6-ghz-band-spectrum-award-2>.
- [24] “Results of the 26 GHz Spectrum Award 2018,” Comreg, 18/53, Ireland, Jun. 2018. Accessed: Feb. 15, 2021. [Online]. Available: <https://www.comreg.ie/publication/results-of-the-26-ghz-spectrum-award-2018/>.
- [25] “Award of the 700 MHz and 3.6-3.8 GHz spectrum bands,” Ofcom, Apr. 2021. Accessed: Apr. 28, 2021. [Online]. Available: https://www.ofcom.org.uk/__data/assets/pdf_file/0028/217954/notice-reg-121.pdf.
- [26] M. Series, “IMT Vision–Framework and overall objectives of the future development of IMT for 2020 and beyond,” *Recomm. ITU*, vol. 2083, p. 0, 2015.
- [27] T. S. Rappaport, Y. Xing, G. R. MacCartney, A. F. Molisch, E. Mellios, and J. Zhang, “Overview of millimeter wave communications for fifth-generation (5G) wireless networks—With a focus on propagation models,” *IEEE Trans. Antennas Propag.*, vol. 65, no. 12, pp. 6213–6230, 2017.
- [28] John (YA), “Path Loss at Millimeter Wave Frequencies | RAYmaps,” 2019. .
- [29] D. Nandi and A. Maitra, “Study of rain attenuation effects for 5G Mm-wave cellular communication in tropical location,” *IET Microwaves, Antennas Propag.*, vol. 12, no. 9, pp. 1504–1507, 2018.
- [30] F. Schwering and A. A. Oliner, “Millimeter-wave antennas,” in *Antenna Handbook*, Springer, 1993, pp. 1–148.
- [31] J. G. Andrews *et al.*, “What will 5G be?,” *IEEE J. Sel. areas Commun.*, vol. 32,

- no. 6, pp. 1065–1082, 2014.
- [32] N. Al-Falahy and O. Y. K. Alani, “Millimetre wave frequency band as a candidate spectrum for 5G network architecture: A survey,” *Phys. Commun.*, vol. 32, pp. 120–144, 2019.
- [33] Y. Azar *et al.*, “28 GHz propagation measurements for outdoor cellular communications using steerable beam antennas in New York City,” in *2013 IEEE international conference on communications (ICC)*, 2013, pp. 5143–5147.
- [34] K.-C. Huang and Z. Wang, *Millimeter wave communication systems*, vol. 29. John Wiley & Sons, 2011.
- [35] “5G spectrum access at 26 GHz and update on bands above 30 GHz,” Ofcom, Jul. 2017. Accessed: Feb. 14, 2021. [Online]. Available: https://www.ofcom.org.uk/__data/assets/pdf_file/0014/104702/5G-spectrum-access-at-26-GHz.pdf.
- [36] A. Kapoor and B. Bayrakci, “Millimeter Wave Body Scanners Market: Past, Present, and Future,” Analog Devices. Accessed: Feb. 17, 2021. [Online]. Available: <https://www.analog.com/media/en/technical-documentation/tech-articles/Millimeter-Wave-Body-Scanners-Market-Past-Present-and-Future.pdf>.
- [37] D. M. Sheen, D. L. McMakin, and T. E. Hall, “Three-dimensional millimeter-wave imaging for concealed weapon detection,” *IEEE Trans. Microw. Theory Tech.*, vol. 49, no. 9, pp. 1581–1592, Sep. 2001.
- [38] Y. Zhang *et al.*, “A novel millimeter-wave backward to forward scanning periodic leaky-wave antenna based on two different radiator types,” *Prog. Electromagn. Res.*, vol. 168, pp. 31–38, 2020.
- [39] A. Krauss, H. Bayer, R. Stephan, and M. A. Hein, “Dual-band leaky-wave antenna

- based on a dual-layer frequency selective surface for bi-directional satcom-on-the-move in Ka-band,” in *2016 International Workshop on Antenna Technology (iWAT)*, 2016, pp. 25–28.
- [40] W. Cao, Z. N. Chen, W. Hong, B. Zhang, and A. Liu, “A Beam Scanning Leaky-Wave Slot Antenna With Enhanced Scanning Angle Range and Flat Gain Characteristic Using Composite Phase-Shifting Transmission Line,” *IEEE Trans. Antennas Propag.*, vol. 62, no. 11, pp. 5871–5875, Nov. 2014.
- [41] Q. Li, Y. Zhang, and C. M. Wu, “Wide-Angle Frequent Scanning Metamaterial Leaky Wave Antenna Array for Automotive Radars,” in *2018 International Conference on Microwave and Millimeter Wave Technology (ICMMT)*, 2018, pp. 1–3.
- [42] K. B. Widener and K. Johnson, “Millimeter wave cloud radar (MMCR) handbook,” DOE Office of Science Atmospheric Radiation Measurement (ARM) Program, 2005.
- [43] M. S. Elbamby, C. Perfecto, M. Bennis, and K. Doppler, “Toward low-latency and ultra-reliable virtual reality,” *IEEE Netw.*, vol. 32, no. 2, pp. 78–84, 2018.
- [44] A. Baratè, G. Haus, L. A. Ludovico, E. Pagani, and N. Scarabottolo, “5G Technology for augmented and virtual reality in education,” in *Proceedings of the International Conference on Education and New Developments*, 2019, vol. 2019, pp. 512–516.
- [45] K. Z. Ghafoor *et al.*, “Millimeter-Wave Communication for Internet of Vehicles: Status, Challenges, and Perspectives,” *IEEE Internet Things J.*, vol. 7, no. 9, pp. 8525–8546, 2020.
- [46] G. A. Deschamps, “Microstrip microwave antennas,” in *Proceedings of the Third*

- Symposium on the USAF Antenna Research and Development Program, Oct, 1953,*
pp. 18–22.
- [47] R. Munson, “Microstrip phased array antennas,” in *1973 EIC 11th Electrical Insulation Conference*, 1973, pp. 281–283.
- [48] R. Munson, “Conformal microstrip antennas and microstrip phased arrays,” *IEEE Trans. Antennas Propag.*, vol. 22, no. 1, pp. 74–78, 1974.
- [49] J. Huang, “Microstrip Antennas: Analysis, Design, and Application,” in *Modern Antenna Handbook*, 2008, pp. 157–200.
- [50] Z. Ahmed, G. Perwasha, S. Shahid, H. Zahra, I. Saleem, and S. M. Abbas, “Ultra wideband antenna with WLAN band-notch characteristic,” in *2013 3rd IEEE International Conference on Computer, Control and Communication (IC4)*, 2013, pp. 1–5.
- [51] K. D. Xu, H. Xu, Y. Liu, J. Li, and Q. H. Liu, “Microstrip Patch Antennas With Multiple Parasitic Patches and Shorting Vias for Bandwidth Enhancement,” *IEEE Access*, vol. 6, pp. 11624–11633, 2018.
- [52] M. K. Khandelwal, B. K. Kanaujia, and S. Kumar, “Defected Ground Structure: Fundamentals, Analysis, and Applications in Modern Wireless Trends,” *Int. J. Antennas Propag.*, vol. 2017, p. 2018527, 2017.
- [53] S. Tripathi, A. Mohan, and S. Yadav, “Hexagonal fractal ultra-wideband antenna using Koch geometry with bandwidth enhancement,” *IET Microwaves, Antennas Propag.*, vol. 8, no. 15, pp. 1445–1450, Dec. 2014.
- [54] C. M. Krishna, P. K. K. Varma, and P. J. Vijay, “Bandwidth Enhancement of Circular Ring Fractal Antenna for Wireless Applications,” in *Microelectronics, Electromagnetics and Telecommunications*, Springer, 2019, pp. 299–309.

- [55] C. A. Balanis, "Microstrip Antennas," in *Antenna theory: analysis and design*, 3rd ed., John Wiley & Sons, 2016.
- [56] P. Bevelacqua, "Antenna Arrays (Phased Arrays)," 2016. <https://www.antenna-theory.com/arrays/main.php#phased> (accessed Jan. 14, 2021).
- [57] F. Rashid and A. Manikas, "Diversity reception for OFDM systems using antenna arrays," in *2006 1st International Symposium on Wireless Pervasive Computing*, 2006, pp. 6 pp. – 6.
- [58] C. A. Balanis, *Antenna theory: analysis and design*. John Wiley & Sons, 2015.
- [59] X. Wang, K.-L. Wu, and W.-Y. Yin, "A compact Gysel power divider with unequal power-dividing ratio using one resistor," *IEEE Trans. Microw. Theory Tech.*, vol. 62, no. 7, pp. 1480–1486, 2014.
- [60] P. S. Hall, J. R. James, and C. Wood, "Microstrip antenna theory and design," *IEE Peter Peregrinus*, p. 204, 1981.
- [61] M. A. Matin, "Review on millimeter wave antennas-potential candidate for 5G enabled applications," *Adv. Electromagn.*, vol. 5, no. 3, pp. 98–105, 2016.
- [62] W. W. Hansen, "Radiating electromagnetic wave guide, US Patent 2,402,622." Google Patents, Jun. 25, 1940.
- [63] A. A. Oliner, "Historical Perspectives on Microwave Field Theory," *IEEE Trans. Microw. Theory Tech.*, vol. 32, no. 9, pp. 1022–1045, 1984.
- [64] C. H. Walter, *Traveling wave antennas*. New York: Dover Publications, 1970.
- [65] "IEEE Standard for Definitions of Terms for Antennas," *IEEE Std 145-2013 (Revision of IEEE Std 145-1993)*. pp. 1–50, 2014.
- [66] C. Caloz and T. Itoh, *Electromagnetic metamaterials: transmission line theory and microwave applications*. John Wiley & Sons, 2005.

- [67] J. L. Gomez-Tornero, A. T. Martinez, D. C. Rebenaque, M. Gugliemi, and A. Alvarez-Melcon, "Design of tapered leaky-wave antennas in hybrid waveguide-planar technology for millimeter waveband applications," *IEEE Trans. Antennas Propag.*, vol. 53, no. 8, pp. 2563–2577, 2005.
- [68] F. Xu and K. Wu, "Understanding Leaky-Wave Structures: A Special Form of Guided-Wave Structure," *IEEE Microw. Mag.*, vol. 14, no. 5, pp. 87–96, 2013.
- [69] K. Barkeshli, K. Barkeshli, and S. Khorasani, "Periodic Structures," in *Advanced Electromagnetics and Scattering Theory*, Springer International Publishing, 2015, pp. 329–335.
- [70] P. Baccarelli, S. Paulotto, D. R. Jackson, and A. A. Oliner, "A New Brillouin Dispersion Diagram for 1-D Periodic Printed Structures," *IEEE Trans. Microw. Theory Tech.*, vol. 55, no. 7, pp. 1484–1495, 2007.
- [71] D. M. Pozar, *Microwave engineering*, 4th ed. John Wiley & sons, 2011.
- [72] G. A. E. Vandenbosch and A. Vasylychenko, *A practical guide to 3D electromagnetic software tools*. INTECH Open Access Publisher, 2011.
- [73] "FEKO." <https://www.altair.com/feko/> (accessed Jun. 22, 2021).
- [74] A. Vasylychenko, Y. Schols, W. De Raedt, and G. A. E. Vandenbosch, "Quality Assessment of Computational Techniques and Software Tools for Planar-Antenna Analysis," *IEEE Antennas Propag. Mag.*, vol. 51, no. 1, pp. 23–38, 2009.
- [75] "Ansys Electronics Desktop." <https://www.ansys.com/products/electronics> (accessed Jun. 22, 2021).
- [76] "Empire XPU." <https://www.empire.de/> (accessed Jun. 22, 2021).
- [77] T. Weiland, "A discretization method for the solution of Maxwell's equations for six-component fields.-Electronics and Communication,(AEÜ), Vol. 31," 1977.

- [78] C. GmbH, “CST Microwave Studio Manual,” *Computer Simulation Technology*, 2020. .
- [79] S. Schmidt LPKF, “PCB Prototyping Systems Put to Work,” *Co. Bus. Mark. Wirel. Des. Dev.*, vol. 8, no. 4, p. 63, 2000, [Online]. Available: https://www.lpkfusa.com/articles/prototyping/wdd_04_2000.pdf.
- [80] “Schwarzbeck BBHA 9170 Data sheet.” <http://schwarzbeck.de/Datenblatt/k9170.pdf>.
- [81] R. & Schwarz, “R&S Vector Network Analyzers ZVA 8 / ZVA 24 / ZVA 40 Operating Manual,” 2005. https://scdn.rohde-schwarz.com/ur/pws/dl_downloads/dl_common_library/dl_manuals/gb_1/z/zva_2/ZVA_ZVB_ZVT_OperatingManual_en_33.pdf.
- [82] K.-S. Chin, H.-T. Chang, J.-A. Liu, H.-C. Chiu, J. S. Fu, and S.-H. Chao, “28-GHz patch antenna arrays with PCB and LTCC substrates,” in *Proceedings of 2011 Cross Strait Quad-Regional Radio Science and Wireless Technology Conference*, 2011, vol. 1, pp. 355–358.
- [83] O. M. Haraz, A. Elboushi, S. A. Alshebeili, and A. R. Sebak, “Dense dielectric patch array antenna with improved radiation characteristics using ebg ground structure and dielectric superstrate for future 5G cellular networks,” *IEEE Access*, vol. 2, pp. 909–913, 2014.
- [84] M. Khalily, R. Tafazolli, T. A. Rahman, and M. R. Kamarudin, “Design of phased arrays of series-fed patch antennas with reduced number of the controllers for 28-GHz mm-wave applications,” *IEEE Antennas Wirel. Propag. Lett.*, vol. 15, pp. 1305–1308, 2015.
- [85] M. K. Ishfaq, T. Abd Rahman, H. T. Chattha, and M. Ur Rehman, “Multiband

- split-ring resonator based planar inverted-F antenna for 5G applications,” *Int. J. Antennas Propag.*, vol. 2017, 2017.
- [86] “Spectrum above 6 GHz for future mobile communications Response from the Radio Society of Great Britain,” Radio Society, 2015. Accessed: Dec. 09, 2020. [Online]. Available: https://www.ofcom.org.uk/__data/assets/pdf_file/0023/69422/spectrum_above_6_ghz_cfi.pdf.
- [87] Z. Ahmed *et al.*, “A uniquely-fed miniaturized ultra-wideband antenna with dual band-rejection characteristics,” *Sci. Int.*, vol. 27, no. 6, 2015.
- [88] Z. Ahmed, F. K. Lodhi, Z. U. Islam, F. Shamshad, I. Rashid, and F. A. Bhatti, “Ultra-wideband microstrip antennas with WLAN band-notch capability,” *Int. J. Comput. Commun. Syst. Eng.*, vol. 2, no. 4, pp. 575–580, 2015.
- [89] D. N. Arizaca-Cusicuna, J. L. Arizaca-Cusicuna, and M. Clemente-Arenas, “High Gain 4x4 Rectangular Patch Antenna Array at 28GHz for Future 5G Applications,” in *2018 IEEE XXV International Conference on Electronics, Electrical Engineering and Computing (INTERCON)*, 2018, pp. 1–4.
- [90] M. Y. Mohamed, A. M. Dini, M. M. Soliman, and A. Z. M. Imran, “Design of 2×2 Microstrip Patch Antenna Array at 28 GHz for Millimeter Wave Communication,” in *2020 IEEE International Conference on Informatics, IoT, and Enabling Technologies (ICIoT)*, 2020, pp. 445–450.
- [91] T. Varum, A. Ramos, and J. N. Matos, “Planar microstrip series-fed array for 5G applications with beamforming capabilities,” in *2018 IEEE MTT-S International Microwave Workshop Series on 5G Hardware and System Technologies (IMWS-5G)*, 2018, pp. 1–3.

- [92] J. Yin, Q. Wu, C. Yu, H. Wang, and W. Hong, “Low-Sidelobe-Level Series-Fed Microstrip Antenna Array of Unequal Interelement Spacing,” *IEEE Antennas Wirel. Propag. Lett.*, vol. 16, pp. 1695–1698, 2017.
- [93] J. Maharjan and D.-Y. Choi, “Four-Element Microstrip Patch Array Antenna with Corporate-Series Feed Network for 5G Communication,” *Int. J. Antennas Propag.*, vol. 2020, 2020.
- [94] B. T. Mohamed and H. Ammor, “A 16-elements Corporate-series Feed Rectangular Patch Antenna Array at 28GHz, for future 5G applications,” in *2019 International Conference on Wireless Technologies, Embedded and Intelligent Systems (WITS)*, 2019, pp. 1–4.
- [95] K. N. Paracha, A. D. Butt, A. S. Alghamdi, S. A. Babale, and P. J. Soh, “Liquid metal antennas: Materials, fabrication and applications,” *Sensors*, vol. 20, no. 1, p. 177, 2020.
- [96] J. R. Aguilar, M. Beadle, P. T. Thompson, and M. W. Shelley, “The microwave and RF characteristics of FR4 substrates,” in *IEE Colloquium on Low Cost Antenna Technology (Ref. No. 1998/206)*, 1998, pp. 2/1-2/6.
- [97] H. Kao *et al.*, “Bending Effect of an Inkjet-Printed Series-Fed Two-Dipole Antenna on a Liquid Crystal Polymer Substrate,” *IEEE Antennas Wirel. Propag. Lett.*, vol. 13, pp. 1172–1175, 2014.
- [98] D. Gaetano, M. J. Ammann, P. McEvoy, M. John, L. Keating, and F. Horgan, “Proximity study of a conformal UWB directional antenna on water pipe,” *Microw. Opt. Technol. Lett.*, vol. 54, no. 8, pp. 1982–1986, 2012.
- [99] D. B. Ferreira, C. B. de Paula, D. C. Nascimento, and A. Kishk, “Design techniques for conformal microstrip antennas and their arrays,” *Adv. Microstrip Antennas with*

Recent Appl., pp. 3–31, 2013.

- [100] R. J. Allard, D. H. Werner, and P. L. Werner, “Radiation pattern synthesis for arrays of conformal antennas mounted on arbitrarily-shaped three-dimensional platforms using genetic algorithms,” *IEEE Trans. Antennas Propag.*, vol. 51, no. 5, pp. 1054–1062, 2003.
- [101] L. Z. Tung, G. A. Mahdiraji, and L. C. Ping, “Comparative Study between planar and bent antenna characterization,” in *MATEC Web of Conferences*, 2018, vol. 152, p. 3002.
- [102] L. M. Bhowmik, C. Armiento, A. Akyurtlu, W. Miniscalco, J. Chirravuri, and C. McCarroll, “Design and analysis of conformal ku-band microstrip patch antenna arrays,” in *2013 IEEE International Symposium on Phased Array Systems and Technology*, 2013, pp. 815–820.
- [103] Z. Ahmed, K. Yang, P. McEvoy, and M. J. Ammann, “Study of mm-Wave microstrip patch array on curved substrate,” in *Loughborough Antennas & Propagation Conference (LAPC 2017)*, 2017, pp. 1–4.
- [104] M. Steer, *Microwave and RF Design: A Systems Approach*. Raleigh, NC, USA: Scitech Publishing Inc., 2010.
- [105] A. Narbudowicz, M. J. Ammann, and D. Heberling, “On pattern reconfigurable antennas steered by modulation scheme,” in *2015 9th European Conference on Antennas and Propagation (EuCAP)*, 2015, pp. 1–4.
- [106] M. Manohar, R. S. Kshetrimayum, and A. K. Gogoi, “Printed monopole antenna with tapered feed line, feed region and patch for super wideband applications,” *IET Microwaves, Antennas Propag.*, vol. 8, no. 1, pp. 39–45, Jan. 2014.
- [107] H. Singh and R. M. Jha, Eds., “Mutual Coupling Effects in Phased Arrays,” in

- Active Radar Cross Section Reduction: Theory and Applications*, Cambridge: Cambridge University Press, 2015, pp. 177–215.
- [108] J. Kraus, “A backward angle-fire array antenna,” *IEEE Trans. Antennas Propag.*, vol. 12, no. 1, pp. 48–50, 1964.
- [109] J. D. Kraus, “Backward angle travelling wave wire mesh antenna array.” Google Patents, Dec. 06, 1966.
- [110] R. Conti, J. Toth, T. Dowling, and J. Weiss, “The wire grid microstrip antenna,” *IEEE Trans. Antennas Propag.*, vol. 29, no. 1, pp. 157–166, 1981.
- [111] M. Sun and Y. P. Zhang, “Grid Antenna Arrays,” in *Handbook of Antenna Technologies*, Z. N. Chen, D. Liu, H. Nakano, X. Qing, and T. Zwick, Eds. Singapore: Springer Singapore, 2016, pp. 1249–1277.
- [112] M. Tiuri, S. Tallqvist, and S. Urpo, “Chain antenna,” in *1974 Antennas and Propagation Society International Symposium*, 1974, vol. 12, pp. 274–277.
- [113] B. Zhang and Y. P. Zhang, “Grid Array Antennas,” *Wiley Encyclopedia of Electrical and Electronics Engineering*. pp. 1–18, Dec. 15, 2014.
- [114] S. D. Assimonis, T. Samaras, and V. Fusco, “Analysis of the microstrip-grid array antenna and proposal of a new high-gain, low-complexity and planar long-range WiFi antenna,” *IET Microwaves, Antennas Propag.*, vol. 12, no. 3, pp. 332–338, 2018.
- [115] H. Nakano, T. Kawano, Y. Kozono, and J. Yamauchi, “A fast MoM calculation technique using sinusoidal basis and testing functions for a wire on a dielectric substrate and its application to meander loop and grid array antennas,” *IEEE Trans. Antennas Propag.*, vol. 53, no. 10, pp. 3300–3307, 2005.
- [116] H. Nakano, I. Oshima, H. Mimaki, K. Hirose, and J. Yamauchi, “Center-fed grid

- array antennas,” in *IEEE Antennas and Propagation Society International Symposium. 1995 Digest*, 1995, vol. 4, pp. 2010–2013 vol.4.
- [117] H. Nakano, T. Kawano, and J. Yamauchi, “Meander-line grid-array antenna,” *IEE Proceedings-Microwaves, Antennas Propag.*, vol. 145, no. 4, pp. 309–312, 1998.
- [118] H. Nakano, H. Osada, H. Mimaki, Y. Iitsuka, and J. Yamauchi, “A Modified Grid Array Antenna Radiating a Circularly Polarized Wave,” in *2007 International Symposium on Microwave, Antenna, Propagation and EMC Technologies for Wireless Communications*, 2007, pp. 527–530.
- [119] H. Nakano, Y. Iitsuka, and J. Yamauchi, “Rhombic Grid Array Antenna,” *IEEE Trans. Antennas Propag.*, vol. 61, no. 5, pp. 2482–2489, 2013.
- [120] G. Xu, H. Luan, H. Peng, Y. Zhang, and W. Yin, “A Microstrip Grid Array Antenna for Dual Band Applications,” in *2018 IEEE International Symposium on Antennas and Propagation & USNC/URSI National Radio Science Meeting*, 2018, pp. 667–668.
- [121] H. Nakano, T. Kawano, and J. Yamauchi, “A cross-mesh array antenna,” in *2001 Eleventh International Conference on Antennas and Propagation, (IEE Conf. Publ. No. 480)*, 2001, vol. 1, pp. 327–330 vol.1.
- [122] H. Nakano, Y. Iitsuka, and J. Yamauchi, “Loop-Based Circularly Polarized Grid Array Antenna With Edge Excitation,” *IEEE Trans. Antennas Propag.*, vol. 61, no. 8, pp. 4045–4053, 2013.
- [123] G. Clasen and R. Langley, “Meshed patch antennas,” *IEEE Trans. Antennas Propag.*, vol. 52, no. 6, pp. 1412–1416, 2004.
- [124] E. A. Soliman, “CPW-FED Brick-Wall Antenna with Parasitic Elements,” *J. Electromagn. Waves Appl.*, vol. 21, no. 10, pp. 1421–1427, Jan. 2007.

- [125] H. Nakano, S. Tajima, N. Suzuki, H. Mimaki, and J. Yamauchi, "The radiation characteristics of honeycomb antennas," in *Tenth International Conference on Antennas and Propagation (Conf. Publ. No. 436)*, 1997, vol. 1, pp. 350–353 vol.1.
- [126] M. Sun and Y. P. Zhang, "Design and integration of 60-GHz grid array antenna in chip package," in *2008 Asia-Pacific Microwave Conference*, 2008, pp. 1–4.
- [127] Z. Chen, L. Zhang, B. Zhang, and Y. P. Zhang, "A Multiport Microstrip Grid Array Structure," *IEEE Trans. Antennas Propag.*, vol. 64, no. 11, pp. 4953–4958, 2016.
- [128] Z. Chen and Y. P. Zhang, "FR4 PCB grid array antenna for millimeter-wave 5G mobile communications," in *2013 IEEE MTT-S International Microwave Workshop Series on RF and Wireless Technologies for Biomedical and Healthcare Applications (IMWS-BIO)*, 2013, pp. 1–3.
- [129] W. A. W. Muhamad, R. Ngah, M. F. Jamlos, P. J. Soh, and H. Lago, "Gain enhancement of microstrip grid array antenna for 5G applications," in *2016 URSI Asia-Pacific Radio Science Conference (URSI AP-RASC)*, 2016, pp. 1827–1829.
- [130] S. F. Jilani, Q. H. Abassi, and A. Alomainy, "Millimeter-Wave Compact and High-Performance Two-Dimensional Grid Array for 5G Applications," in *2019 IEEE International Symposium on Antennas and Propagation and USNC-URSI Radio Science Meeting*, 2019, pp. 25–26.
- [131] S. F. Jilani, Q. H. Abassi, and A. Alomainy, "Millimetre-Wave MIMO Array of a Compact Grid Antenna for 5G Wireless Networks and Beyond," in *2020 International Conference on UK-China Emerging Technologies (UCET)*, 2020, pp. 1–4.
- [132] S. Hakimi and S. K. A. Rahim, "Millimeter-wave microstrip Bent line Grid Array antenna for 5G mobile communication networks," in *2014 Asia-Pacific Microwave*

- Conference*, 2014, pp. 622–624.
- [133] “Consultation on proposed 26 GHz Spectrum Award 2018,” 2017. Accessed: Dec. 17, 2020. [Online]. Available: https://www.comreg.ie/media/dlm_uploads/2017/10/ComReg1785.pdf.
- [134] Z. Ahmed, P. McEvoy, and M. J. Ammann, “Comparison of Grid Array and Microstrip Patch Array Antennas at 28 GHz,” in *2018 IEEE MTT-S International Microwave Workshop Series on 5G Hardware and System Technologies (IMWS-5G)*, 2018, pp. 1–3.
- [135] P. Feng, X. Chen, X. Ren, C.-J. Liu, and K.-M. Huang, “A novel microstrip grid array antenna with both high-gain and wideband properties,” *Prog. Electromagn. Res.*, vol. 34, pp. 215–226, 2013.
- [136] C. Xing, C. Kain, and H. Kama, “A microstrip grid array antenna optimized by a parallel genetic algorithm,” *Microw. Opt. Technol. Lett.*, vol. 50, no. 11, pp. 2976–2978, 2008.
- [137] X. Chen, G. Wang, and K. Huang, “A Novel Wideband and Compact Microstrip Grid Array Antenna,” *IEEE Trans. Antennas Propag.*, vol. 58, no. 2, pp. 596–599, 2010.
- [138] E. Bruce, “Aerial Systems,” U.S. Patent 1,813,143, Jul. 07, 1931.
- [139] R. D. Straw, “The ARRL Antenna Book,” in *Newington, CT*, The American Radio Relay League, 2000.
- [140] H. Nakano, N. Odachi, H. Mimaki, and J. Yamauchi, “An array of Franklin and Bruce antennas,” in *IEEE Antennas and Propagation Society International Symposium. 1996 Digest*, 1996, vol. 2, pp. 1130–1133.
- [141] S.-Y. Y. Chen, “Broadband slot-type bruce array fed by a microstrip-to-slotline T-

- junction,” *IEEE Antennas Wirel. Propag. Lett.*, vol. 8, pp. 116–119, 2009.
- [142] S. Kamal *et al.*, “A Novel Negative Meander Line Design of Microstrip Antenna for 28 GHz mmWave Wireless Communications,” *Radioengineering*, vol. 29, no. 3, p. 479, 2020.
- [143] H. Shawkey and D. Elsheakh, “Multiband Dual-Meander Line Antenna for Body-Centric Networks’ Biomedical Applications by Using UMC 180 nm,” *Electronics*, vol. 9, no. 9, p. 1350, 2020.
- [144] Z. Ahmed, M. H. Hoang, P. McEvoy, and M. J. Ammann, “Millimetre-wave Planar Bruce Array Antenna,” in *2020 International Workshop on Antenna Technology (iWAT)*, 2020, pp. 1–3.
- [145] D. R. Jackson, C. Caloz, and T. Itoh, “Leaky-wave antennas,” *Proc. IEEE*, vol. 100, no. 7, pp. 2194–2206, 2012.
- [146] D.-F. Guan, P. You, Q. Zhang, Z.-B. Yang, H. Liu, and S.-W. Yong, “Slow-wave half-mode substrate integrated waveguide using spoof surface plasmon polariton structure,” *IEEE Trans. Microw. Theory Tech.*, vol. 66, no. 6, pp. 2946–2952, 2018.
- [147] S.-D. Xu *et al.*, “A wide-angle narrowband leaky-wave antenna based on substrate integrated waveguide-spoof surface plasmon polariton structure,” *IEEE Antennas Wirel. Propag. Lett.*, vol. 18, no. 7, pp. 1386–1389, 2019.
- [148] Z. B. Yang *et al.*, “Low-Loss Spoof Surface Plasmon Polariton Based on Folded Substrate Integrated Waveguide,” *IEEE Antennas Wirel. Propag. Lett.*, vol. 18, no. 1, pp. 222–225, Jan. 2019.
- [149] Y. You, Y. Lu, Q. You, Y. Wang, J. Huang, and M. J. Lancaster, “Millimeter-wave high-gain frequency-scanned antenna based on waveguide continuous transverse

- stubs,” *IEEE Trans. Antennas Propag.*, vol. 66, no. 11, pp. 6370–6375, Nov. 2018.
- [150] W. Zhou, J. Liu, and Y. Long, “Investigation of shorting vias for suppressing the open stopband in an SIW periodic leaky-wave structure,” *IEEE Trans. Microw. Theory Tech.*, vol. 66, no. 6, pp. 2936–2945, Jun. 2018.
- [151] D. Zheng, Y. L. Lyu, and K. Wu, “Longitudinally Slotted SIW Leaky-Wave Antenna for Low Cross-Polarization Millimeter-Wave Applications,” *IEEE Trans. Antennas Propag.*, vol. 68, no. 2, pp. 656–664, Feb. 2020.
- [152] Y. L. Lyu *et al.*, “Leaky-Wave Antennas Based on Noncutoff Substrate Integrated Waveguide Supporting Beam Scanning From Backward to Forward,” *IEEE Trans. Antennas Propag.*, vol. 64, no. 6, pp. 2155–2164, Jun. 2016.
- [153] S. Rezaee and M. Memarian, “Analytical Study of Open-Stopband Suppression in Leaky-Wave Antennas,” *IEEE Antennas Wirel. Propag. Lett.*, vol. 19, no. 2, pp. 363–367, Feb. 2020.
- [154] A. Kandwal, Z. Nie, L. Wang, L. W. Y. Y. Liu, and R. Das, “Realization of low profile leaky wave antennas using the bending technique for frequency scanning and sensor applications,” *Sensors (Switzerland)*, vol. 19, no. 10, May 2019.
- [155] S. Cheng, Y. Li, Z. Liang, S. Zheng, and Y. Long, “An approximate circuit model to analyze microstrip rampart line in OSB suppressing,” *IEEE Access*, vol. 7, pp. 90412–90417, 2019.
- [156] M. R. Naeini, M. Fakharzadeh, and F. Farzaneh, “Travelling-wave Ka-band frequency scanning antennas for millimeter-wave imaging applications,” in *2016 8th International Symposium on Telecommunications (IST)*, 2016, pp. 591–595.
- [157] Z. Ahmed, P. McEvoy, and M. J. Ammann, “Millimetre-Wave Frequency Scanning Rampart Array Antenna,” in *INSPIRE TU Dublin Conference*, 2019, p.

1.

- [158] L. Zhu, “Guided-wave characteristics of periodic coplanar waveguides with inductive loading - unit-length transmission parameters,” *IEEE Trans. Microw. Theory Tech.*, vol. 51, no. 10, pp. 2133–2138, 2003.
- [159] W. Jiang, C. Liu, B. Zhang, and W. Menzel, “K-band frequency-scanned leaky-wave antenna based on composite right/left-handed transmission lines,” *IEEE Antennas Wirel. Propag. Lett.*, vol. 12, pp. 1133–1136, 2013.
- [160] S. Xie, J. Li, G. Deng, J. Feng, and S. Xiao, “A wide-angle scanning leaky-wave antenna based on a composite right/left-handed transmission line,” *Appl. Sci.*, vol. 10, no. 6, Mar. 2020.
- [161] H. Yu, K. Zhang, X. Ding, and Q. Wu, “A dual-beam leaky-wave antenna based on squarely modulated reactance surface,” *Appl. Sci.*, vol. 10, no. 3, Feb. 2020.
- [162] P. Baccarelli, S. Paulotto, D. R. Jackson, and A. A. Oliner, “Analysis of printed periodic structures on a grounded substrate: a new Brillouin dispersion diagram,” in *IEEE MTT-S International Microwave Symposium Digest, 2005.*, 2005, p. 4 pp.
- [163] K. Rudramuni *et al.*, “Goubau-line leaky-wave antenna for wide-angle beam scanning from backfire to endfire,” *IEEE Antennas Wirel. Propag. Lett.*, vol. 17, no. 8, pp. 1571–1574, 2018.
- [164] X.-L. Tang *et al.*, “Continuous Beam Steering Through Broadside Using Asymmetrically Modulated Goubau Line Leaky-Wave Antennas,” *Sci. Rep.*, vol. 7, no. 1, p. 11685, 2017.
- [165] A. Hessel, “General Characteristics of Traveling-Wave Antennas,” in *Antenna Theory—Part 2*, McGraw-Hill Book Company, New York, 1969.
- [166] J. T. Williams, P. Baccarelli, S. Paulotto, and D. R. Jackson, “1-D comblines leaky-

- wave antenna with the open-stopband suppressed: Design considerations and comparisons with measurements,” *IEEE Trans. Antennas Propag.*, vol. 61, no. 9, pp. 4484–4492, 2013.
- [167] S. Paulotto, P. Baccarelli, F. Frezza, and D. R. Jackson, “A novel technique for open-stopband suppression in 1-D periodic printed leaky-wave antennas,” *IEEE Trans. Antennas Propag.*, vol. 57, no. 7, pp. 1894–1906, 2009.
- [168] Y. Li, Q. Xue, H. Z. Tan, and Y. Long, “The half-width microstrip leaky wave antenna with the periodic short circuits,” *IEEE Trans. Antennas Propag.*, vol. 59, no. 9, pp. 3421–3423, Sep. 2011.
- [169] C. Caloz, D. R. Jackson, and T. Itoh, “Frontiers in antennas: next generation design & engineering,” in *Frontiers in Antennas: Next Generation Design Engineering.*, McGraw-Hill., 2011.
- [170] Q. Yang, X. Zhao, and Y. Zhang, “Design of CRLH Leaky-Wave Antenna with Low Sidelobe Level,” *IEEE Access*, vol. 7, pp. 178224–178234, 2019.
- [171] D. M. Sheen *et al.*, “Wide-bandwidth, wide-beamwidth, high-resolution, millimeter-wave imaging for concealed weapon detection,” in *Passive and Active Millimeter-Wave Imaging XVI*, 2013, vol. 8715, p. 871509.
- [172] J. Liu, W. Zhou, and Y. Long, “A Simple Technique for Open-Stopband Suppression in Periodic Leaky-Wave Antennas Using Two Nonidentical Elements Per Unit Cell,” *IEEE Trans. Antennas Propag.*, vol. 66, no. 6, pp. 2741–2751, Jun. 2018.
- [173] S. Otto, A. Rennings, K. Solbach, and C. Caloz, “Transmission line modeling and asymptotic formulas for periodic leaky-wave antennas scanning through broadside,” *IEEE Trans. Antennas Propag.*, vol. 59, no. 10, pp. 3695–3709, Oct.

2011.

- [174] Z. Ahmed, M. John, P. Mcevoy, and M. J. Ammann, "Investigation of Frequency Scanning Printed Bruce Array Antenna," *IEEE Access*, vol. 8, pp. 189003–189012, Oct. 2020.
- [175] H. V Nguyen, A. Parsa, and C. Caloz, "Power-Recycling Feedback System for Maximization of Leaky-Wave Antennas' Radiation Efficiency," *IEEE Trans. Microw. Theory Tech.*, vol. 58, no. 7, pp. 1641–1650, 2010.
- [176] G. Ruvio and M. J. Ammann, "Effects of Klopfenstein tapered feedlines on the frequency- and time-domain performance of planar monopole UWB antennas," in *2008 IEEE Antennas and Propagation Society International Symposium*, 2008, pp. 1–4.
- [177] V. Demir, D. Elsherbeni, D. Kajfez, and A. Elsherbeni, "Efficient wideband power divider for planar antenna arrays," *Appl. Comput. Electromagn. Soc. J.*, vol. 21, pp. 318–323, 2006.
- [178] R. W. Klopfenstein, "A Transmission Line Taper of Improved Design," *Proc. IRE*, vol. 44, no. 1, pp. 31–35, 1956.
- [179] D. Kajfez and J. O. Prewitt, "Correction to 'A Transmission Line Taper of Improved Design' (Letters)," *IEEE Trans. Microw. Theory Tech.*, vol. 21, no. 5, p. 364, 1973.
- [180] Z. Ahmed, P. McEvoy, and M. J. Ammann, "A Wide Frequency Scanning Printed Bruce Array Antenna with Bowtie and Semi-Circular Elements," *Sensors*, vol. 20, no. 23, p. 6796, Nov. 2020.
- [181] G. Zhang, Q. Zhang, S. Ge, Y. Chen, and R. D. Murch, "High Scanning-Rate Leaky-Wave Antenna Using Complementary Microstrip-Slot Stubs," *IEEE Trans.*

- Antennas Propag.*, vol. 67, no. 5, pp. 2913–2922, 2019.
- [182] M. H. Rahmani and D. Deslandes, “Backward to Forward Scanning Periodic Leaky-Wave Antenna With Wide Scanning Range,” *IEEE Trans. Antennas Propag.*, vol. 65, no. 7, pp. 3326–3335, Jul. 2017.
- [183] A. Zhang, R. Yang, D. Li, B. Hu, Z. Lei, and Y. Jiao, “Metasurface-Based Tapered Waveguide Slot Array Antennas for Wide Angular Scanning in a Narrow Frequency Band,” *IEEE Trans. Antennas Propag.*, vol. 66, no. 8, pp. 4052–4059, Aug. 2018.
- [184] S. Zhan-shan, R. Ke, C. Qiang, B. Jia-jun, and F. Yun-qi, “3D radar imaging based on frequency-scanned antenna,” *IEICE Electron. Express*, vol. 14, no. 12, p. 20170503, 2017.
- [185] H. Choe and S. Lim, “Millimeter-Wave Continuous Transverse Stub (CTS) Antenna Array Using Substrate Integrated Waveguide (SIW) Technology,” *IEEE Trans. Antennas Propag.*, vol. 62, no. 11, pp. 5497–5503, 2014.
- [186] Y. L. Lyu, F. Y. Meng, G. H. Yang, Q. Wu, and K. Wu, “Leaky-Wave Antenna with Alternately Loaded Complementary Radiation Elements,” *IEEE Antennas Wirel. Propag. Lett.*, vol. 17, no. 4, pp. 679–683, Apr. 2018.

List of Publications

Journal Publications

- [JP 1] Z. Ahmed, P. McEvoy and M. J. Ammann, “A Wide Frequency Scanning Bruce Array Antenna with Bowtie and Semi-Circular Elements”, MDPI Sensors, 20, 6796, 2020.
- [JP 2] Z. Ahmed, M. John, P. McEvoy and M. J. Ammann, “Investigation of Frequency Scanning Printed Bruce Array Antenna”, IEEE Access, 8, 189003-189012, 2020.

Conference Publications

- [CP 1] Z. Ahmed, M. H. Hoang, P. McEvoy and M. J. Ammann, “Mm-wave Planar Bruce Array Antenna”, IEEE International Workshop on Antenna Technology (iWAT), Bucharest, Romania, 2020.
- [CP 2] M. H. Hoang, Z. Ahmed, M. John, P. McEvoy and M. J. Ammann, “Calibration for a Hybrid MIMO Near-field Imaging System to Mitigate Antennas Effects”, IEEE International Workshop on Antenna Technology (iWAT), Bucharest, Romania, 2020. (*Best Paper Award*)
- [CP 3] Z. Ahmed, P. McEvoy and M. J. Ammann, “Millimeter-wave frequency scanning rampart array antenna”, TU Dublin’s Inspire 2019, Technological

University Dublin, Ireland, 2019. (*Abstract*) (*Image Featured on Cover of Conference Magazine*)

- [CP 4] Z. Ahmed, P. McEvoy and M. J. Ammann, “Comparison of Grid Array and Microstrip Patch Antennas at 28 GHz”, IEEE MTT-S International Microwave Workshop Series on 5G Hardware and System Technologies, Dublin, Ireland, 2018. (*Nominated for Best Paper Award*)
- [CP 5] Z. Ahmed, K. Yang, P. McEvoy and M. J. Ammann, “Study of mm-wave Microstrip Patch Array on Curved Substrate”, IET Loughborough Antennas & Propagation Conference (LAPC ‘17), Loughborough, United Kingdom, 2017.

List of Modules Completed for Structure PhD

Employability Skills Modules

Module Code	Module Name	Credits (ECTS)	Institute Attended
PRJM 2000	Project Management: Tools and Techniques for Academic Research	5	Dublin Institute of Technology (DIT)
THED H1001	Teaching in Higher Education	5	Institute of Technology Tallaght (ITT)
RESM 1950	Research Methods	5	DIT
PGRE 9014	Research Information Retrieval	5	DIT

Discipline Specific Modules

Module Code	Module Name	Credits (ECTS)	Institute Attended
CIVL 9001	Finite Elements in Science and Engineering	5	DIT
NMAD 1003	Applied Optics – Polarisation of Light	5	DIT
TFEV 9002	International Event Management	10	Technological University Dublin (TU Dublin)